2009

Oxidation modeling by means of molecular dynamics

Chaiyod Soontrapa
University of Nevada Las Vegas

OXIDATION MODELING BY MEANS OF MOLECULAR DYNAMICS

by

Chaiyod Soontrapa

Bachelor of Science
Carnegie Mellon University, Pittsburgh, PA
2001

Master of Science
Massachusetts Institute of Technology, Cambridge, MA
2005

A dissertation submitted in partial fulfillment of
the requirements for the

Doctor of Philosophy Degree in Mechanical Engineering
Department of Mechanical Engineering
Howard R. Hughes College of Engineering

Graduate College
University of Nevada, Las Vegas
December 2009

UNIVERSITY OF NEVADA LAS VEGAS

THE GRADUATE COLLEGE

We recommend that the dissertation prepared under our supervision by

Chaiyod Soontrapa

entitled

Oxidation Modeling by Means of Molecular Dynamics

be accepted in partial fulfillment of the requirements for the degree of

Doctor of Philosophy
Mechanical Engineering

Yitung Chen, Committee Chair

Robert Boehm, Committee Member

William Culbreth, Committee Member

Anthony Hechanova, Committee Member

John W. Farley, Graduate Faculty Representative

Ronald Smith, Ph. D., Vice President for Research and Graduate Studies
and Dean of the Graduate College

December 2009

ABSTRACT

Oxidation Modeling by Means of Molecular Dynamics

by

Chaiyod Soontrapa

Dr. Yitung Chen, Doctoral Advisory Committee Chair
Professor of Mechanical Engineering
University of Nevada, Las Vegas

Oxidation modeling is normally engineered to study systems at macroscopic scales, mostly in analytical forms based on diffusion theories. The associated time scale is usually in months, days, or minutes, and the length scale is in the order of microns. In this dissertation, oxidation modeling is performed at atomistic scale with the time and length scales in picoseconds and angstroms, respectively, using molecular dynamics. Molecular dynamics simulations generate trajectories of each atom or particle in a system according to the laws of physics. Studying oxidations under the atomistic point of view can offer new insights on atomic behaviors and influencing factors in oxidation mechanisms.

This dissertation focuses on modeling dynamic behaviors of liquid lead, oxygen, and iron. Lead is used as a coolant in nuclear reactors due to its excellent physical properties such as high boiling point and neutron transparency. Nevertheless, liquid lead is very corrosive to iron, the main structural material in reactors. As lead diffuses along grain boundaries and other faults in iron crystals, iron lattices become brittle. In addition, oxygen dissolving in liquid lead causes another problem. Too much oxygen promotes undesired compound formations of lead oxide, typically known as slags, which hinder the

coolant flow. However, when only traces of oxygen are present in this lead-iron system, protective iron oxide layers form and help preventing further ingress of liquid lead.

This dissertation provides a new approach in modeling oxidations, using the Generalized Reduced Gradient (GRG) method in minimizing the potential energy of a metal/metal oxide system. The approach is then applied to model iron oxidation in the form of magnetite. Finally, a system consisting of liquid lead, iron, and oxygen is studied under several scenarios.

ACKNOWLEDGEMENTS

I would like to express my deep gratitude toward a number of people for their kind support during the final epic of my long endured academic journey. I am truly indebted to Professor Yitung Chen for his devotion and invaluable advice on my doctoral research. I would like to thank my dissertation committee members: Professor Robert Boehm, Professor William Culbreth, Professor Anthony Hechanova, and Professor John W. Farley, for their valuable time and effort. I am greatly blessed with the morale support from my parents and brother. I also would like to thank all of my friends for their warm support during this hard academic epic. Finally, I am grateful for the financial support from the US Department of Energy through the University of Nevada, Las Vegas, Transmutation Research Program (TRP) (Grant No. DE-FG04-2001AL67358). Without the grant, this project would have never been completed.

TABLE OF CONTENTS

LIST OF TABLES

LIST OF FIGURES

CHAPTER 1

INTRODUCTION

1.1 Lead and Lead Bismuth Eutectic as Coolants

Owing to its outstanding properties, lead proves to be an excellent candidate for a coolant used in advanced nuclear reactors and accelerator driven systems (ADS) [1]. The melting point of lead is relatively low at 327.46 °C (600.61 K) while its boiling point is at 1749 °C (2022.15 K). The high boiling point of lead offers a possible application in thermochemical production of hydrogen, which requires the threshold temperature of 830 °C (1103.15 K). Lead is also transparent to neutrons because it provides low moderation, low absorption, but good reflection of neutrons, which is beneficial to neutron economy in fast reactors. In nuclear reactors, lead actively absorbs dangerous gamma radiation due to the very high density of lead. Unlike sodium, which is another candidate coolant in advanced nuclear reactors, lead is relatively inert to air and water, providing safer heat exchange between the primary and secondary loops. The high density of lead also helps keeping the design dimensions of lead-cooled reactors relatively small.

An alloy composed of 44.8% lead and 55.2% bismuth by weight is called Lead-Bismuth Eutectic (LBE). A eutectic is a mixture of two or more solids at such proportions that the mixture's melting temperature is at a local minimum. Figure 1.1 shows the LBE phase diagram [2]. Compared to lead, LBE has a lower melting point of 125.5 °C (398.65 K) and a lower boiling point of 1670 °C (1943.15 K). The high boiling points of lead and LBE improve passive safety in case of loss of coolant accidents. This means coolants can absorb more energy without boiling off to further pressurize reactor systems. LBE also carries over attractive properties of lead such as neutron transparency

and high density. However, at least two disadvantages exist for the use of bismuth. First, the price of bismuth is many times higher than the price of lead. In 2008, bismuth cost about $12 per pound, while lead cost only about $1 per pound [3]. The second disadvantage comes from polonium, a by-product of bismuth irradiation. Polonium is born when bismuth undergoes neutron capture with subsequent beta decay. Alpha particles emitted by polonium can easily damage organic tissues and increase the risk of cancer. In addition, the major drawback of using lead and its alloys as coolants remains in their very corrosive nature to structure materials such as steels.

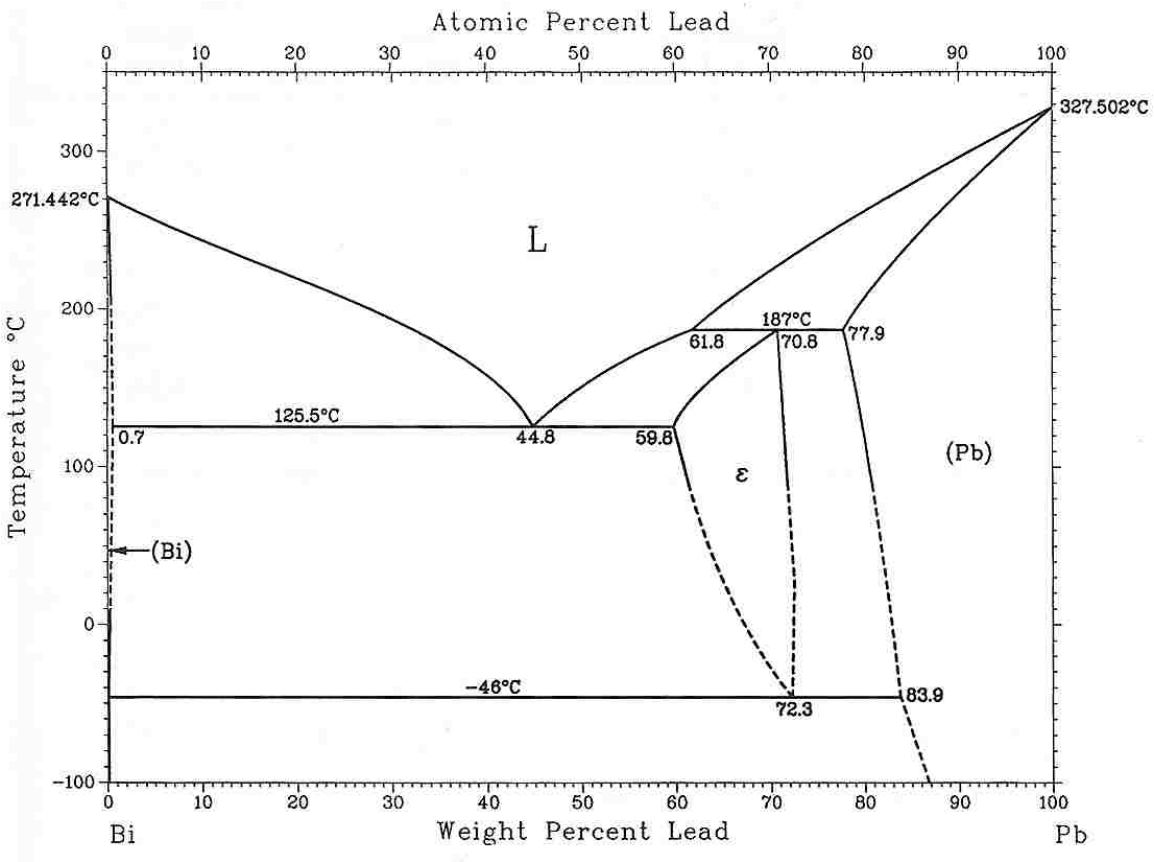

Figure 1.1 The phase diagram of lead-bismuth eutectic [2]

1.2 Corrosion in Liquid Lead Alloy Environments

Liquid metal corrosion involves several variables that can greatly affect corrosion rates. Those variables belong in one of the following three categories: (1) operating condition, (2) metallurgy, and (3) manufacture [4]. Examples of the corrosion factors according to their categories are listed in Table 1.1 [4, 5].

Table 1.1 Corrosion factors that influence corrosion rates [4, 5]

Categories of Corrosion Factors	Corrosion Factors
Operating Condition	• Temperature • Temperature gradient • Cyclic temperature • Surface area to volume ratio • Flow velocity
Metallurgy	• Purity of liquid metal • Mixed metal systems in the same liquid metal • Microstructure of container materials
Manufacture	• Condition of container materials

Operating Condition:

- Temperature

  Temperature is the most important variable in liquid metal corrosion. Higher temperature leads to higher solubility and higher diffusivity, which in turn accelerate corrosion.

- Temperature gradient

  A temperature gradient changes solubility limits of the same solid metal in hot and cold parts of a circulation loop. It causes the continued loss of materials from the hot parts, and can possibly lead to selective removal if the loop components are made of different materials.

- Cyclic temperature

  In a poorly controlled furnace, for example, sizable fluctuations in temperature allow solid metals to dissolve into liquid metals when temperature is erratically high. Later, when temperature drops, dissolved metals precipitate in the bulk liquid. If this cycle continues, thinning of the furnace walls will be evident.

- Surface area to volume ratio

  Corrosion increases when the ratio of an exposed metallic surface area to the volume of liquid metal decreases. In an isolated static system, solid metals will eventually saturate liquid metals that they come in contact. Given two containers with the same surface area, a container with a larger amount of a liquid metal (hence larger volume) will corrode more heavily than the one with less amount of the same liquid metal. The more liquid metals are added into the system, the more solid metals will dissolve in the liquid metals.

- Flow velocity

  The flow velocity, or as measured by the Reynolds number, becomes very important in a forced-circulation loop. The corrosion impacts depend on how fast the coolant is flowing over solid material surfaces, and, therefore, this type of

corrosion is termed Flow Accelerated Corrosion (FAC) [6]. The FAC combines the mechanical effects (abrasion and impingement) with electrochemical effects (dissolution and oxidation), and each effect has varied domination over one another depending on the flow velocity. Generally, three velocity domains are considered: (a) low velocity, (b) moderate velocity, and (c) high velocity [7].

(a) In the low velocity domain, the mass transfer fully or partially dominates. When there is no flow, the solubility of solid in liquid reaches its limit at the solid-liquid interface. When a low-velocity flow starts, some of the corrosion products at the interface are carried by the liquid flow. A stronger flow will give rise to a higher corrosion rate because solid dissolves more at the solid-liquid interface to make up for the transported fragments.

(b) In the moderate velocity domain, the flow rate continues to be the limiting factor until the flow velocity reaches a critical value. When that happens, dissolution rate becomes the limiting factor instead. The corrosion rate in this sub-domain becomes activation controlled. In the activation controlled sub-domain, the dissolution of solid in liquid dictates the rate at which the corrosion products are formed. Therefore, regardless of the flow velocity, the dissolution and reaction rates fully control the corrosion rate. The strong flow just simply carries all the corrosion products from the interface.

(c) In the high velocity domain, all mechanical effects become crucial. Shear stresses in a single-phase highly turbulent flow and particle impacts in a

multi-phase turbulent flow can strip off passive oxide films from the base metals. This behavior shortens diffusion distances between the underlying metals and liquid, and that hastens the corrosion rates. In addition, if the flow changes its directions sharply due to sudden expansions/contractions or elbows in the circulation loop, erosion corrosion becomes severe as liquid and particles suspending in the flow are thrown against the loop walls. Cavitation corrosion can also occur if the voids in the flowing liquid metals suddenly collapse on the loop walls. Micro jets of heavy liquid metal atoms burst out from the collapsed bubbles will collide at high velocities with the loop walls, leaving those walls under high local pressures. High stress in solid metal structures can result in consequences such as localized fatigue damages and stress-assisted cracking.

The low velocity domain is where the flow is essentially laminar, while the flow is turbulent in the remaining two domains (b) and (c). Figure 1.2 shows the diagram of velocity effects on the corrosion rate. Within the turbulent flow domain, the combination of different effects results in four types of flow accelerated corrosion besides the underlying mass transfer that is continuously active whenever a flow exists. The four FAC types are (1) activation-controlled corrosion, (2) phase-transport controlled corrosion, (3) erosion corrosion, and (4) cavitation corrosion [8]. The classification of these four corrosion types is shown in Fig. 1.3 [8]. All of these corrosion types have been described briefly, except for the phase-transport controlled corrosion. The phase-transport controlled corrosion involves reactive phases in flowing liquid, usually gaseous phases that

contaminate the liquid. The phase-transport begins when reactive phases wet or get in contact with structural surfaces. The nature of the flow can accelerate the corrosion if the flow efficiently transports these aggressive contaminations throughout the loop, or the flow has bends or sudden expansions that create surface eddies. An example of this corrosion type includes carbon in liquid sodium that impairs the elastic properties of 316-type stainless steels [9]. Another example is oxygen in liquid sodium that aggravates corrosion in austenite chromium-nickel steels [10]. Figure 1.4 shows the schematics of these four corrosion types in the turbulent flow domain.

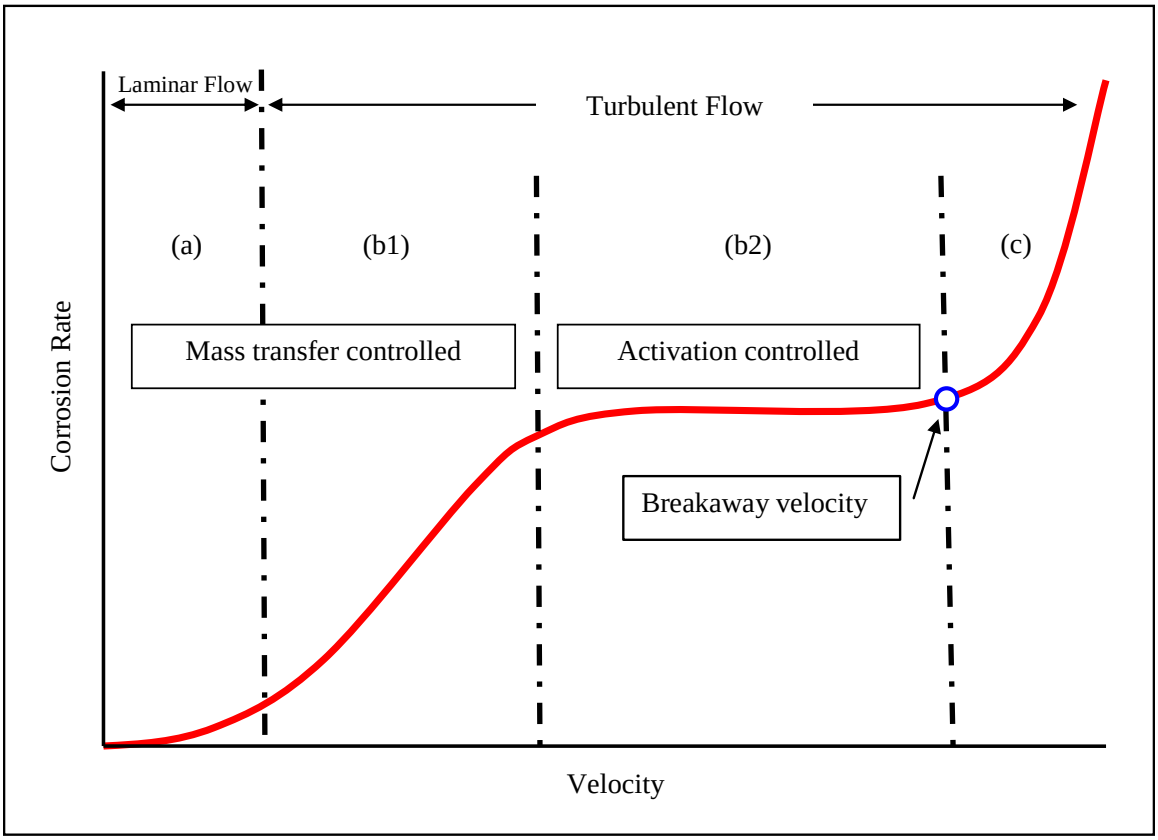

Figure 1.2 Velocity effects on the corrosion rate [7]

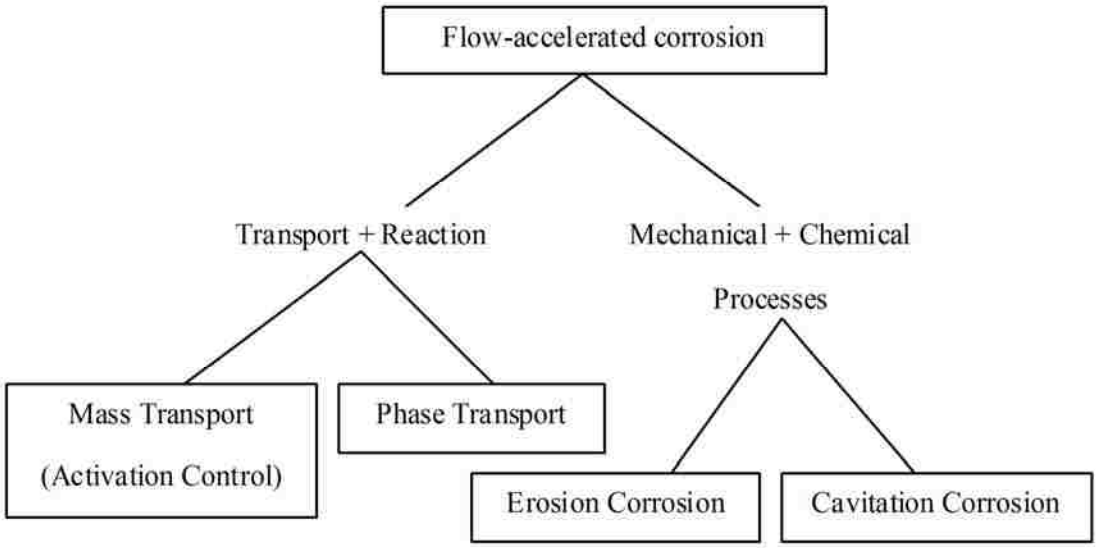

Figure 1.3 Classification of flow accelerated corrosion [8]

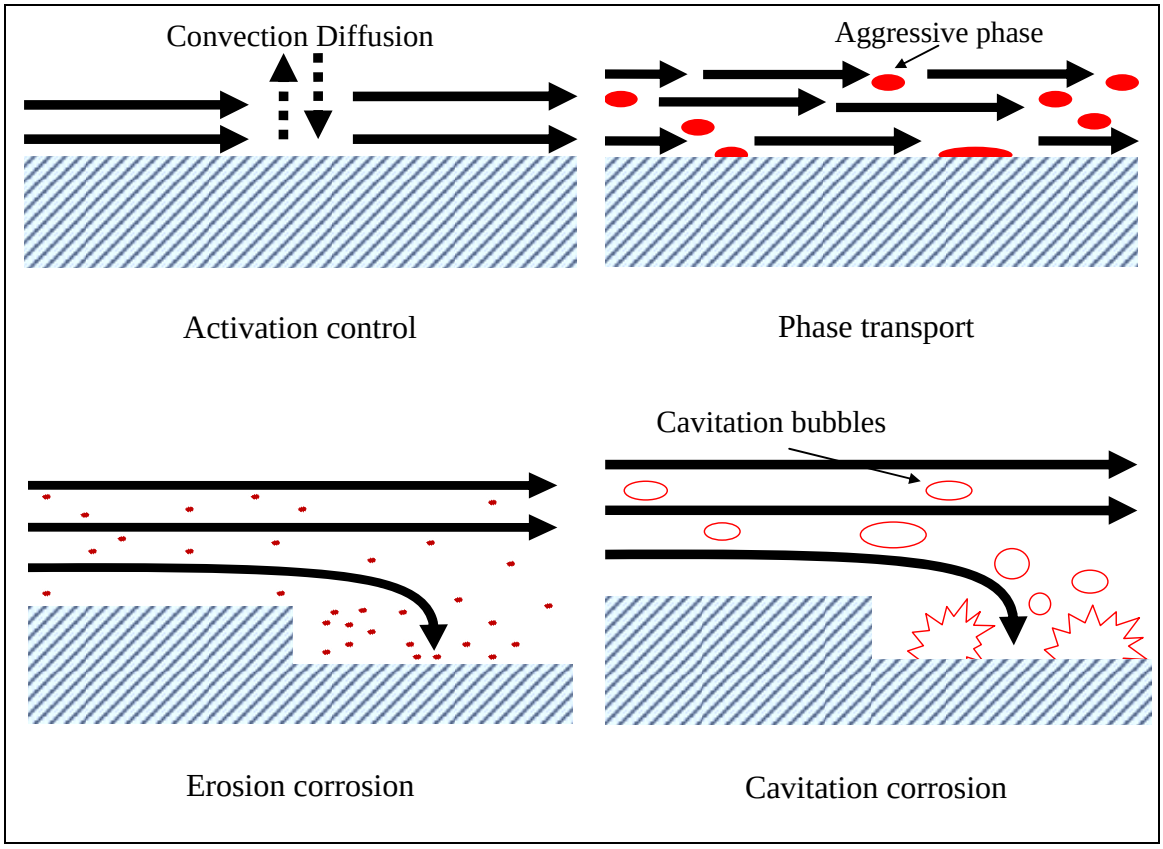

Figure 1.4 Four types of flow accelerated corrosion [8]

Metallurgy:

- Purity of liquid metal

  Purity of the liquid metal can impact the rate at which the solubility limit is reached and the wetting tendency of the liquid metal on the solid metal. Impurities in liquid metals can either enhance or worsen corrosion rates.

- Mixed metal systems in the same liquid metal

  When a container or a loop is made of a combination of solid metals, a mass transfer phenomenon (dissimilar mass transfer or concentration mass transfer) can occur even under an isothermal condition. A system consisting of multiple types or phases of solid metals reaches equilibrium only when all the chemical potentials of each distinct type or phase are equal to each other. The constituents in the system components will be continuously redistributed until all the chemical potentials satisfy an equality. The equalization of the chemical potentials, the main driving force behind this process, forces the free energy of the system to become lower.

- Microstructure of the container materials

  The microstructure of the container materials such as grain sizes and precipitations along grain boundaries affect the rates at which liquid metal attacks on solid metals. Wettability of individual grains and the wettability of grain boundaries are different. Good wettability normally accelerates corrosion rates. Corrosion can be greatly enhanced along a continuous carbide or oxide network at the grain boundary.

Manufacture:

- Condition of container materials

  During a manufacturing process, welding, loading, cold work and other operations can cause container materials having unwanted grain boundary precipitates and second phases, high stress state of metals, and unfavorable grain sizes. This effectively leaves the container materials in compromised conditions. For example, thinning due to liquid metal corrosion combined with high stress in container materials potentially foster premature failures. Also, an uncontrolled factory environment can introduce oxide films on the surfaces of container materials. In a static system, the primary effect of surface films is to change the rate at which the liquid metal is saturated. The greater the unprotected surface area that is exposed, the faster the liquid becomes saturated. After equilibrium is reached between the liquid metal and the solid metal, the surface condition should have no effect.

All of the above corrosion factors play their roles in either promoting or deterring corrosion attacks of liquid metals on solid metals.

Based on visual detections, there are two general types of corrosive attacks on solid metals by liquid metals: (1) uniform corrosion and (2) local corrosion [4]. In uniform corrosion, the attack of liquid metals on solid metals proceeds evenly over the contact areas between solid and liquid metals. Thinning on the surfaces continues until structural failures take place. However, uniform corrosion can be easily measured and predicted. In contrast, local corrosion is much harder to observe as damage occurs below the surfaces of solid metal structures.

Furthermore, uniform and local corrosion can be further categorized based on specific nature of the attacks. There are four kinds of corrosive attacks as follows [5]:

(1) Simple solution

The simple solution attack corrodes solid metal surfaces evenly. The driving force of the attacks is solubility of solid metals in liquid metals. For a static system, if all phase diagrams of liquid-solid metals in the system are available, penetration depths can be predicted based on solubility limits at a specific temperature. Examples of the simple solution attack include the corrosion of titanium in liquid lead at 1000 °C and iron in liquid lithium at 1000 °C.

(2) Diffusion penetration

There are two modes of penetration: intragranular and intergranular. In both modes of attack, intermetallic compounds (alloys) between liquid and solid metal species are usually formed. In the intragranular mode of attack, liquid metals dissolve directly into the grains of solid metals. In the intergranular mode of attack, liquid metals penetrate along the grain boundaries. Between the two modes of attack, the intergranular attack causes more disastrous damages to structural metals, and it is often the preferred mode of attack. Grain boundaries provide easy paths for diffusion of liquid metals. As a result of penetrations and alloy formations along the grain boundaries, adhesion between grains weakens and grains easily detach from their crystalline networks.

(3) Impurity reactions

Impurities such as oxygen and nitrogen in liquid metals can promote or slow corrosion rates. For example, nitrogen reacts with carbon in stainless steel, causing

removal of carbon from the grain boundaries of steel. In contrast, oxygen forms protective film layers on steel that act as contact barriers between steel and liquid lead.

(4) Mass transfer

There are two types of mass transfer as listed below. Each type of mass transfer differs by the driving force behind it.

(4.1) Temperature-gradient mass transfer

The driving force behind this type of corrosion is the difference in solubility of a solid metal in a liquid metal at various temperatures. At a very hot portion of a circulation loop, atoms from pure solid metals or solid alloys made up the piping of the loop diffuse out to the surfaces and dissolve in the liquid metal. They are then carried through the loop. Upon reaching colder portions of that loop, they settle and re-crystallize because the solubility is less in these cold parts than in the hot parts.

(4.2) Dissimilar-metal mass transfer

This type of corrosion is driven by the decrease in free energy of a system by alloying two or more different metals. In a circulation loop that was made of two or more different metals, atoms of one metal species dissolve in a liquid metal, travel through the loop, and diffuse into another metal species, forming an alloy.

To conclude, only simple solution is uniform corrosion, while the rest are local corrosion. Table 1.2 summarizes the corrosion natures and their driving forces.

Table 1.2 Summary of the corrosion types

Damage Type	Nature of Attack	Driving Force
Uniform Corrosion	simple solution	isothermal solubility of solid in liquid
Local Corrosion	diffusion penetration	solubility of liquid in solid
	impurity reactions	reactions between constituents in solid with impurities in liquid
	Mass transfer • temperature-gradient mass transfer • dissimilar-metal mass transfer	 • solubility of solid in liquid at different temperatures • reduction in free energy

Liquid metal corrosion studies often mention three important parameters: (1) wettability, (2) solubility, and (3) diffusivity. Surface wetting plays an important role. A liquid with more wettability can spread itself over a large surface area, while a liquid with low wettability only appears as droplets on solid surfaces. Therefore, the more wettability a liquid metal has on a solid metal surface, the faster corrosion proceeds. This is directly related to the surface to volume ratio, one of the corrosion factors mentioned earlier. On the other hand, wettability of liquid metals becomes lower when solid metal surfaces are protected by passive oxide layers. An experiment has shown that a presence of passive oxide layers on T91 steel deters surface wetting by liquid lead [11].

The second parameter is solubility. Related to corrosion attacks of liquid lead on solid iron are two important kinds of solubility: (1) oxygen solubility and (2) iron

solubility in liquid lead. In the temperature range between 400 °C and 700 °C, the solubility of oxygen in liquid lead is given by [1]:

$$\log C_O = 3.2 - 5000/T \tag{1.1}$$

where C_O is the concentration of oxygen in wt. % and T is the temperature in Kelvin. At 550 °C, the concentration of oxygen is 1.3×10^{-3} wt. %. This translates into 1 oxygen atom for about every 60 lead atoms. The oxygen solubility determines the upper limit of oxygen control. Oxygen control, a key corrosion protection method, will help maintaining protective oxide layers. Any oxygen exceeding its solubility limit will react with lead to form undesirable lead oxides. The oxygen control process will be discussed in Chapter 4.

In the temperature range between 330 °C and 910 °C, the solubility of iron in liquid lead is [1]:

$$\log C_O = 0.34 - 3450/T \tag{1.2}$$

where C_O is the concentration of oxygen in wt. % and T is the temperature in Kelvin. At 550 °C, the concentration of iron is 1.4×10^{-4} wt. %. This is roughly 1 iron atom in 1914 lead atoms. As stated earlier, if the solubility is available, the amount of metal losses can be calculated for a static system (no flow). This provides a rough estimate of how much thinning will occur over time. The volume of liquid lead can be calculated from [1]:

$$\rho_{Pb} = 11367 - 1.1944T \tag{1.3}$$

where ρ_{Pb} is the lead density in kg/m^3 and T is the temperature in Kelvin in the range 600 K to 2000 K. Figure 1.5 gives an estimate of iron loss in kilograms per one cubic meter of liquid lead at various temperatures in a static system using Eqns. (1.2) and (1.3).

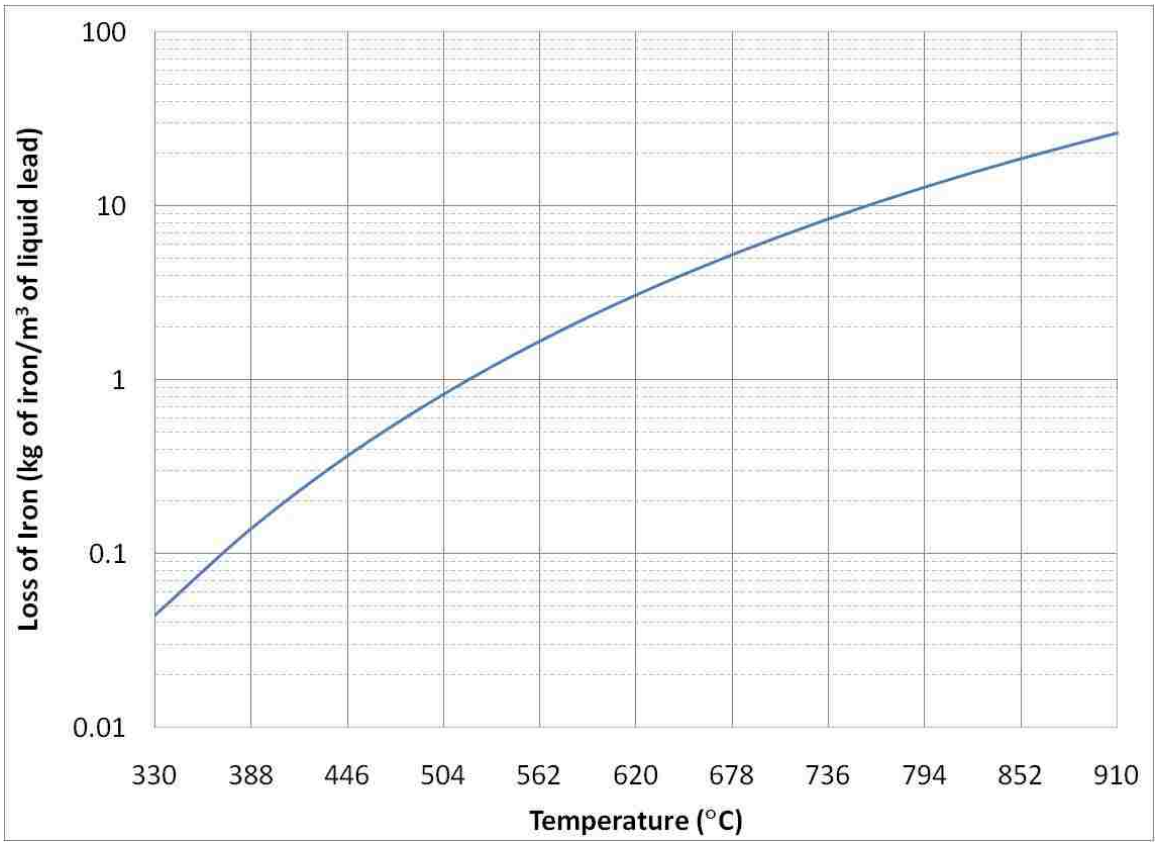

Figure 1.5 Iron loss in liquid lead at different temperatures in a static system

The last parameter is the diffusivity, which measures how fast an atom can travel in a given environment. In the temperature range from 700 ° C to 1000 ° C, the diffusivity D of iron in lead and LBE is approximated by [1]:

$$\log D = -2.31 - 2295/T \tag{1.4}$$

where D is in cm^2/s, and the temperature T is in Kelvin. The diffusion and dissolution rates serve as two important parameters in analytical modeling of liquid lead and LBE corrosion behaviors.

1.3 Prevention of Liquid Metal Corrosion Attacks on Solid Metals

To prevent corrosion attacks from liquid metals on solid metals, the following three methods are usually implemented: (1) alloying of stable oxide formers, (2) surface coating, and (3) adding corrosion inhibitors [1]. All of these methods involve passive oxide formations over the surfaces of structural materials. Each prevention method only works well at certain oxygen concentrations in liquid metals. Therefore, oxygen level in liquid metals must be controlled specifically for each corrosion prevention method.

In the first prevention method, stable oxide formers such as silicon and aluminum will be alloyed with structural metals to become the thin surface layers of the structural metals. The alloyed surfaces do not affect the mechanical properties of the bulk materials due to their very thin surface layers compared to the bulk volume. With excellent adherence to the structural surfaces, oxide scales of silicon and aluminum oxides can block or minimize the ingress of liquid metals into bulk materials. Self-healing of oxide scales stay continuously active as long as oxide forming elements remain in alloyed surfaces throughout the service duration.

The second prevention method relies on direct coating of structural surfaces with corrosion-resistant alloys and compounds or metals that have low solubility in liquid metals. The disadvantages of this prevention method are poor adherence and lack of self-healing ability to rebuild oxide films. However, when treated with pulsed electron

beams, the coatings are welded to the bulk materials, essentially transforming to the case of alloyed surfaces, and, as a result, adherence is improved.

The last prevention method is to add corrosion inhibitors. By definition, inhibitors are substances that are added in small quantities to a chemical system with the pure purpose to slow down reaction rates among reactants. There are two types of inhibitors: metallic and non-metallic. Examples of metallic inhibitors include zirconium (Zr) and titanium (Ti). In LBE with very low oxygen, zirconium and titanium are found to reduce the dissolution rate of iron into LBE. Instead of typical oxide scale formation, it is postulated that Zr and Ti first form nitride scales with available dissolved nitrogen in steels. Once nitrogen is depleted, they find available dissolved carbon in steels and form carbide scales. On the other hand, when a feasible concentration of oxygen exists in LBE, oxygen itself acts as a non-metallic corrosion inhibitor. Oxygen oxidizes iron and protective oxide films are formed. Clearly, oxygen works well only when there is enough oxygen concentration in liquid metals. That is why oxygen control becomes a focal interest to ensure oxide formations and self-healing when damaged oxide layers wear off.

1.4 Liquid Lead Corrosion Modeling

Several models for liquid lead and LBE corrosion have been proposed. Many of these models are almost all analytical and deal primarily with the macroscopic behavior of LBE loop systems. The analytical models are usually based on diffusion theories and semi-empirical data gathered from experiments. In a LBE loop, only the mass transfer and activation controlled domains are preferred. Therefore, kinetic models have been specifically engineered for these two domains of interest [12-18]. Stochastic cellular

automaton modeling offers a departure from the analytical and semi-empirical modeling. Tan and Chen formulated cellular automaton modeling to study the interactive behaviors among iron, lead, bismuth, and oxygen at the mesoscopic scale, the next closest to the atomistic scale [19]. There are only a few studies on the interatomic behaviors of lead and iron atoms. These studies employed molecular dynamics to explore interatomic interactions in iron-lead systems.

The first molecular dynamics simulation work was done by Takahashi el al. [20]. The Takahashi group applied a quantum mechanics theory, called the density functional theory, to simulate systems containing solid iron and liquid LBE. Maulana et al. became the second research group to use molecular dynamics on modeling steels in LBE using a traditional pair potential function [21]. Both studies do not consider protective oxide layers in their simulations. Incorporating oxygen into simulations involves variable charges on ions due to oxidation during the course of a simulation. The lack of considering oxidation in these models has been rectified in this dissertation.

1.5 Molecular Dynamics

Molecular dynamics (MD) is a computer simulation process that generates trajectories of atoms or molecules in a system. There are two levels of molecular dynamics: Newtonian and Quantum. Quantum MD can simulate bond forming and breaking among atoms, while Newtonian MD cannot accurately deal with those abrupt changes. Although Newtonian MD cannot provide exact details of how atoms bonded together and in what configurations, it can provide representative details of oxidation processes such as oxide layer thickness and how thick a layer should be in order to

completely seal off oxygen ingress. These oxide layers can be virtually observed and measured from MD simulation results. The units related to molecular dynamics simulations are usually in angstroms $(\mathring{\mathrm{A}})$ for distance, electron volts (eV) for energy, picoseconds (ps) for time, and atomic mass units (amu) for mass. This dissertation also adopts these units unless otherwise noted.

1.5.1 Verlet Algorithm

Newton's second law of motion states that force $\vec{F}$ is equal to the product of a mass m and acceleration $\vec{a}$:

$$\vec{F} = m\vec{a} \tag{1.5}$$

In addition, the relationship between force $\vec{F}$ and potential energy U is

$$\vec{F} = -\vec{\nabla}U \tag{1.6}$$

Therefore, acceleration can also be written as:

$$\vec{a} = -\frac{\vec{\nabla}U}{m} \tag{1.7}$$

Typically in molecular dynamics simulations, the potential energy U is a function of position $\vec{r}$. This essentially makes the acceleration a function of position, $a(\vec{r})$.

To begin constructing a particle trajectory, a Taylor's series expansion is applied to the position $\vec{r}_i$ of a particle i at one time step Δt ahead of a current time t. This gives:

$$\vec{r}_i(t+\Delta t) = \vec{r}_i(t) + \vec{v}_i(t)\Delta t + \frac{1}{2}\vec{a}_i(t)(\Delta t)^2 + \frac{1}{6}\vec{b}_i(t)(\Delta t)^3 + O\left(\Delta t^4\right) \tag{1.8}$$

where $\vec{v}_i$ is the velocity of the particle i and $\vec{b}_i$ is the jerk, the third derivative of the position with respect to time. The error in the above equation is in the order of Δt^4,

which can be represented in the Big O notation as $O(\Delta t^4)$. The position of that particle at one time step backward is then

$$\vec{r}_i(t-\Delta t) = \vec{r}_i(t) - \vec{v}_i(t)\Delta t + \frac{1}{2}\vec{a}_i(t)(\Delta t)^2 - \frac{1}{6}\vec{b}_i(t)(\Delta t)^3 + O(\Delta t^4) \qquad (1.9)$$

Adding Eqns. (1.8) and (1.9) together gives

$$\vec{r}_i(t+\Delta t) = 2\vec{r}_i(t) - \vec{r}_i(t-\Delta t) + \vec{a}_i(t)(\Delta t)^2 + O(\Delta t^4) \qquad (1.10)$$

The above scheme is called the Verlet central difference method. This method, however, suffers at the initial condition (when $t = 0$). The position $\vec{r}_i(0)$ and acceleration $\vec{a}_i(0)$ are known, but the position $\vec{r}_i(-\Delta t)$ is unknown. In order to overcome this problem, an approximation from Eq. (1.8) can be made in the first time step as:

$$\vec{r}_i(\Delta t) = \vec{r}_i(0) + \vec{v}_i(0)\Delta t + \frac{1}{2}\vec{a}_i(0)(\Delta t)^2 + O(\Delta t^3) \qquad (1.11)$$

Although the accuracy drops to $O(\Delta t^3)$, a small time step usually helps compensate for accuracy for this one-time only approximation over many time steps during the course of a simulation. At subsequent time steps, calculations revert back to Eq. (1.8), the original basic Verlet, and the accuracy still holds at $O(\Delta t^4)$.

Certain cases of molecular dynamics simulations require velocity in calculating instantaneous kinetic energy and temperatures. The basic Verlet equation does not explicitly prescribe the velocity. From Eq. (1.9), the velocity $\vec{v}_i(t)$ can be approximated by:

$$\vec{v}_i(t) = \frac{\vec{r}_i(t) - \vec{r}_i(t-\Delta t)}{\Delta t} + O(\Delta t^2) \qquad (1.12)$$

Substituting the above equation into Eq. (1.10) yields a more popular scheme called the Velocity Verlet scheme:

$$\vec{r}_i(t+\Delta t) = \vec{r}_i(t) + \vec{v}_i(t)\Delta t + \vec{a}_i(t)(\Delta t)^2 + O\left(\Delta t^3\right) \tag{1.13}$$

The derivative with respect to time of the above equation is the velocity $\vec{v}_i(t+\Delta t)$:

$$\vec{v}_i(t+\Delta t) = \vec{v}_i(t) + \vec{a}_i(t)\Delta t + O\left(\Delta t^2\right) \tag{1.14}$$

As the name suggests, the Velocity Verlet scheme includes the velocity in the equations for finding positions and velocities, and it avoids the initial value problem of $\vec{r}_i(-\Delta t)$. Substituting Eq. (1.7) in Eq. (1.13) yields:

$$\vec{r}_i(t+\Delta t) = \vec{r}_i(t) + \vec{v}_i(t)\Delta t - \frac{1}{m}\vec{\nabla}U\left(\vec{r}_i(t)\right)(\Delta t)^2 + O\left(\Delta t^3\right) \tag{1.15}$$

Given initial conditions, once the potential function is known, a particle position can be calculated.

1.5.2 Beeman Algorithm

Instead of the Verlet algorithm, all the simulations in this dissertation use the Beeman algorithm, which is a variation of the Verlet algorithm. The accuracy of the Beeman algorithm is $O\left(\Delta t^3\right)$ in velocity compared to $O\left(\Delta t^2\right)$ of the original Verlet algorithm. The equations for Beeman algorithm are:

$$\vec{r}_i(t+\Delta t) = \vec{r}_i(t) + \vec{v}_i(t)\Delta t + \frac{(\Delta t)^2}{6}\left[4\vec{a}_i(t) - \vec{a}_i(t-\Delta t)\right] + O\left(\Delta t^4\right) \tag{1.16}$$

$$\vec{v}_i(t+\Delta t) = \vec{v}_i(t) + \frac{\Delta t}{6}\left[2\vec{a}_i(t+\Delta t) + 5\vec{a}_i(t) - \vec{a}_i(t-\Delta t)\right] + O\left(\Delta t^3\right) \tag{1.17}$$

The regular Beeman algorithm does not assume velocity-dependence. That is, the acceleration $\vec{a}$ used in Eqns. (1.16) and (1.17) is only a function of position $\vec{r}$, $\vec{a}(\vec{r})$, (see Eq. (1.7)). However, certain simulations require that forces, and hence acceleration,

depend on not only positions but also velocities. Examples of such simulations include the ones that utilize the Nose-Hoover algorithm to keep temperature constant or the Parrinello-Rahman algorithm to keep pressure constant. This means, the acceleration now has to be a function of both position and velocity, $\vec{a}(\vec{r},\vec{v})$.

To fully incorporate velocity dependence, the original Beeman algorithm needs to be modified to carry a predictor-corrector scheme. First, the position of a particle at time $t+\Delta t$ is determined from Eq. (1.16). Then, the predicted velocity $\vec{v}_i^{(p)}$ at time $t+\Delta t$ is calculated from a new equation:

$$\vec{v}_i^{(p)}(t+\Delta t) = \vec{v}_i(t) + \frac{\Delta t}{2}\left[3\vec{a}_i(t) - \vec{a}_i(t-\Delta t)\right] + O\left(\Delta t^3\right) \tag{1.18}$$

The predicted velocity and position at time $t+\Delta t$ give the acceleration $\vec{a}(t+\Delta t)$ from the force $\vec{F}$:

$$\vec{a}_i(t+\Delta t) = \vec{F}\left(\vec{r}_i(t+\Delta t), \vec{v}_i^{(p)}(t+\Delta t)\right) \tag{1.19}$$

The resulting acceleration is then used in finding the corrected velocity $\vec{v}_i^{(c)}$ from Eq. (1.17):

$$\vec{v}_i^{(c)}(t+\Delta t) = \vec{v}_i(t) + \frac{\Delta t}{6}\left[2\vec{a}_i(t+\Delta t) + 5\vec{a}_i(t) - \vec{a}_i(t-\Delta t)\right] + O\left(\Delta t^3\right) \tag{1.20}$$

Substituting $\vec{v}_i^{(c)}$ for $\vec{v}_i^{(p)}$ in Eq. (1.16) gives a new value of $\vec{v}_i^{(c)}$. The iteration continues until convergence between $\vec{v}_i^{(c)}$ and $\vec{v}_i^{(p)}$ is reached, which usually takes 2-3 cycles.

1.5.3 Nose-Hoover Algorithm

The Nose-Hoover algorithm can set a system at specific temperature during a simulation, and the algorithm has been used in this dissertation. The algorithm couples a system with a heat bath, and heat will be transferred back and forth between the system

and heat bath in order to keep the system temperature relatively constant. In the Nose-Hoover algorithm, Newton's second law of motion is modified to have an additional term related to the heat bath:

$$\vec{a}_i(t) = \frac{\vec{F}_i(t)}{m_i} - \zeta(t)\vec{v}_i(t) \tag{1.21}$$

The friction coefficient ζ is defined as:

$$\frac{d}{dt}\zeta(t) = \frac{N_F}{Q}\left(k_B T(t) - k_B T_0\right) \tag{1.22}$$

The number of degrees of freedom N_F is equal to $3N+1$, where N is the number of particles in a system, $T(t)$ is the instantaneous temperature, T_0 is the heat bath temperature, and k_B is the Boltzmann constant. The fictitious mass parameter Q determines the heat transfer rate. Normally the Q value does not have any effects unless its value is incredibly large or extremely small. If Q is too large, the system will decouple from the heat bath and that renders the algorithm ineffective. If Q is too small, heat will flow back and forth too frequently between the system and the heat bath, and that makes the system become unphysical.

1.5.4 Computer Programs for Molecular Dynamics Simulations and Visualizations

This dissertation relies on the computer code "Moldy" to perform molecular dynamics (MD) simulations. Moldy was written by Keith Refson in the C language specifically for MD simulations of condensed matters [22]. Moldy was chosen because of its relatively compact size and flexibility to be modified. The Moldy code is easy to read and follow line by line of the code, compared to other molecular dynamics simulation computer programs. The two modifications made to Moldy for this

dissertation are the additions of (1) the Embedded Atom Method (EAM) potential and (2) the Generalized Reduced Gradient (GRG) Method as explained in the next chapter.

After Moldy has finished a simulation, the simulation results are translated into a format called pbd (an acronym for Protein Data Bank). The pdb files can be visualized through another computer program called VMD (short for Virtual Molecular Dynamics). VMD is developed by the Theoretical and Computational Biophysics group at the University of Illinois and the Beckman Institute [23]. VMD can display and animate molecular dynamics configurations and trajectories in a variety of representations. All of the simulation figures in this dissertation have been processed through VMD.

1.6 Dissertation Purpose

This dissertation offers another approach to study corrosion behavior in liquid lead – iron systems. Difficulties in doing experiments on liquid lead corrosions discourage experimental investigations on various cases and scenarios. Currently, the available experimental data are scarce and scattered [24 – 27]. With modeling via molecular dynamics, representative behaviors can be obtained, and they help in optimizing experiment designs with minimal costs. In addition, molecular dynamics modeling can lead to the developments of new alloys for better corrosion resistance in liquid lead and LBE. The rest of this dissertation is arranged as follows:

- Chapter 2 discusses electrostatic energy minimization in oxidation modeling
- Chapter 3 shows the results of iron oxidation modeling
- Chapter 4 shows the results of oxide layer modeling in lead-iron systems
- Chapter 5 concludes the dissertation

CHAPTER 2

OPTIMIZATION APPROACH IN VARIABLE-CHARGE POTENTIAL FOR METAL/METAL OXIDE SYSTEMS

2.1 Introduction

An oxidation occurs when a fresh metal is exposed to oxygen. The process, which sometimes yields undesired results, can impede corrosion by forming protective oxide layers. For example, chromium and silicon can form internal oxides in steel alloys preventing corrosion/erosion from lead-bismuth coolant in fast nuclear reactors [1]. Molecular dynamics (MD) can be used as a tool to study how oxidation occurs. By applying Newtonian MD, oxide layers can be virtually observed and measured from MD simulation results.

In Newtonian MD, each atom or particle obeys Newton's second law of motion ($\vec{F} = m\vec{a}$) and the force acting on the particle can be found by taking the first spatial derivative of the particle's potential energy ($F_x = -dU/dx$, for example). In the case of oxide simulations, the total energy is the sum of electrostatic (ES) energy and non-electrostatic (non-ES) energy. For a given environment, the electrostatic energy depends only on ionic charges, and it can vary greatly for a pair of ions with different oxidation states. Repulsive and attractive forces arising from different charged pairs keep ionic compounds in balance. The non-ES energy, independent of ion charges, describes inter-atomic interactions among various atoms. A widely used inter-atomic potential for metals is the embedded atom method (EAM) potential [28, 29]. The idea of EAM originates from embedding an atom into a site surrounded by electron clouds.

2.2 Embedded Atom Method (EAM)

Most of the well-known potentials such as Lennard-Jones potentials only describe interactions between two atoms or molecules. However, within a group of atoms or molecules, an atom is acted on by not one, but many of its neighboring atoms. Therefore, there is a need for many-body potential functions and the embedded atom method is one of them. The EAM potential can be derived from the Density Functional Theory (DFT), a quantum mechanical theory, which describes ground state properties of many-body systems. Using the Hohenberg and Kohn theorems, Daw showed that the EAM potential is a semi-empirical application of DFT [30].

The EAM potential has contributions from three parts: (1) a pair potential φ, (2) an electron density function ρ, and (3) an embedding energy function F. The EAM potential takes the form:

$$E = F(\rho) + \varphi \tag{2.1}$$

The pair potential takes the form:

$$\phi(r) = Ae^{-\alpha\left(\frac{r}{r_e}-1\right)} - Be^{-\beta\left(\frac{r}{r_e}-1\right)} \tag{2.2}$$

where A, B, α, and β are fitting parameters that are positive numbers, r is the distance between two atoms, and r_e is the first nearest neighbor distance of a crystal at equilibrium. The electron density f of each individual atom as a function of the distance r away from that atom is:

$$f(r) = f_e e^{-\beta\left(\frac{r}{r_e}-1\right)} \tag{2.3}$$

where f_e is defined as the ratio between cohesive energy E_c and an atomic volume at equilibrium Ω_0, or $f_e \equiv E_c / \Omega_0$ [31]. The total electron density ρ at a point or a lattice site is approximated by the linear superposition of electron densities from all atoms surrounding that site, and it can be expressed as:

$$\rho = \sum_i f(r_i) \tag{2.4}$$

where r_i is the distance from the i^{th} neighbor to the site of interest. This total electron density dictates how much energy is needed to embed an atom at a given site.

The embedding energy function determines the energy to embed an atom into a cloud of electrons coming from the neighboring atoms. The analytic form of the embedding energy function used in this dissertation was found independently by two research groups: Johnson [32] and Banerjea & Smith [33]. The embedding energy function takes the form:

$$F = F_0\left(1 - \eta \ln\left(\frac{\rho}{\rho_e}\right)\right)\left(\frac{\rho}{\rho_e}\right)^{\eta} \tag{2.5}$$

where ρ_e is the density of a lattice at equilibrium, and F_0 and η are the fitting parameters. Banerjea and Smith developed the above equation from semi-empirical data, while Johnson derived it from the Rose equation:

$$E = -E_c\left(1 + a_0\left(\frac{r_1}{r_e} - 1\right)\right)\exp\left(-a_0\left(\frac{r_1}{r_e} - 1\right)\right) \tag{2.6}$$

with $a_0 = \sqrt{\frac{9\Omega_0 \tilde{B}}{E_c}}$, where $\tilde{B}$ is the bulk modulus, and E_c is the cohesive energy. By combining Eqns. (2.5) and (2.6), the embedding energy function is of the form:

$$F = -E_c\left(1+a_0\left(\frac{r_1}{r_e}-1\right)\right)\exp\left(-a_0\left(\frac{r_1}{r_e}-1\right)\right)-\varphi \tag{2.7}$$

From Eq. (2.4), the total electron density due to the first n nearest neighbors is:

$$\rho = nf_e e^{-\beta\left(\frac{r_1}{r_e}-1\right)} \tag{2.8}$$

At equilibrium the total electron density ρ_e is nf_e. Taking the natural logarithmic on both sides of Eq. (2.8) gives

$$\frac{r_1}{r_e}-1 = -\frac{1}{\beta}\ln\left(\frac{\rho}{nf_e}\right) = -\frac{1}{\beta}\ln\left(\frac{\rho}{\rho_e}\right) \tag{2.9}$$

Substituting Eq. (2.9) in Eq. (2.7) yields

$$F = -E_c\left(1-\frac{a}{\beta}\ln\left(\frac{\rho}{\rho_e}\right)\right)\left(\frac{\rho}{\rho_e}\right)^{\frac{a}{\beta}}-\varphi \tag{2.10}$$

Equation (2.10) is very similar to Eq. (2.5) developed by Banerjea and Smith from semi-empirical data. For convenience in parameter fitting, Eq. (2.5) is used in this dissertation. Furthermore, Eq. (2.5) is normalized in such a way that

$$\left.\frac{dF}{d\rho}\right|_{\rho=\rho_e} = -\frac{F_0\eta^2}{\rho}\left(\frac{\rho}{\rho_e}\right)\ln\left(\frac{\rho}{\rho_e}\right)\Bigg|_{\rho=\rho_e} = 0 \tag{2.11}$$

Details in parameter fitting for the EAM potential will be described in Chapter 3.

2.3 Electrostatics Energy Minimization

Using a second-order Taylor series expansion about a neutral point of an atom i, Rappé and Goddard [34] expressed energy of its isolated ion with a charge q_i as:

$$E_i(q_i) = E(0)+\chi_i q_i+\frac{1}{2}J_i q_i^2 \tag{2.12}$$

where $\chi_i = \frac{\partial E_i}{\partial q_i}$ is the electronegativity of the atom i, and $J_i = \frac{\partial^2 E_i}{\partial q_i^2}$ is its self-Coulomb repulsion or Chemical Hardness. The electronegativity and self-Coulomb repulsion can be calculated from the first ionization energy (IE) and electron affinity energy (IA) as follows [34, 35]:

$$\chi = \frac{1}{2}(IE + IA) \tag{2.13}$$

$$J = IE - IA \tag{2.14}$$

Within a group of ions (an ionic crystal, for example), Coulomb interactions among ions contribute to a total energy of each individual ion. The total energy of the atom i can now be written as:

$$E_i(q_i) = E(0) + \chi_i q_i + \frac{1}{2} J_i q_i^2 + \frac{1}{2} k_C q_i \sum_{j \neq i} \frac{q_j}{r_{ij}}, \tag{2.15}$$

where k_C is the Coulomb constant and r_{ij} is a distance between ions i and j. To write the above equation more compactly, define

$$J_{ij} = \begin{cases} \frac{1}{2} J_i & , i = j \\ \frac{1}{2} \frac{k_C}{r_{ij}} & , i \neq j \end{cases} \tag{2.16}$$

Equation (2.15) then becomes

$$E_i(q_i) = E(0) + \left(\chi_i + \sum_j J_{ij} q_j \right) q_i \tag{2.17}$$

Since the total energy of the ion i is the sum of electrostatic and non-electrostatic energies, the $E(0)$ term can be safely considered as part of the non-electrostatic EAM. Therefore the electrostatic energy E_i^{es} of an atom i is

$$E_i^{es}(q_i) = \left(\chi_i + \sum_j J_{ij} q_j \right) q_i \tag{2.18}$$

As the environment changes, each charge q_i in a system must readjust itself to match the environment. There have been many attempts to find charge distributions in response to changes in the system environment. However, each approach has some unresolved issues as described below.

Rappé and Goddard [34] used the electronegativity equalization that, at equilibrium, each chemical potential $\mu_i = \frac{\partial E_i}{\partial q_i}$ must be equal to the same value, say μ. This leads to $\sum_j J_{ij} q_j = \mu - \chi_i$, or in a matrix form as $\mathrm{J}\mathbf{q} = \boldsymbol{\mu} - \boldsymbol{\chi}$. The charge vector is then $\mathbf{q} = \mathrm{J}^{-1}(\boldsymbol{\mu} - \boldsymbol{\chi})$. The chemical potential value μ is calculated to be $\mu = \left(\sum_{i,j} J_{ij}^{-1} \chi_j + \sum_i q_i \right) \Big/ \sum_{i,j} J_{ij}^{-1}$. Initially, the charge neutrality condition $\sum_i q_i = 0$ is applied and μ becomes $\mu = \left(\sum_{i,j} J_{ij}^{-1} \chi_j \right) \Big/ \left(\sum_{i,j} J_{ij}^{-1} \right)$. Once the chemical potential value μ is known, each q_i can be solved for. When the values of q_i's exceed their physical charge limits, the values are fixed at the limits. Successive calculations then consider only unfixed charges with the net charge equal to the negative sum of all fixed charges $\sum_{i,i=unfixed} q_i = -q_{fixed}$. The calculations are repeated until all the q_i values are within

their bounds. Although this approach ensures that all the charges stay within their limits, a system is not guaranteed to be at equilibrium when charges are forced to be fixed at their bounds. Hence, the total energy is not minimized. To illustrate this, consider one oxygen atom and two aluminum atoms that are aligned along one straight line. The distances between each pair of the atoms are $1.44\,\mathring{\mathrm{A}}$ for the Al-O pairs, $1.44\,\mathring{\mathrm{A}}$ and $2.88\,\mathring{\mathrm{A}}$ for the Al-Al pairs. The charge limits on aluminum and oxygen are $0 \le q_{Al} \le +3e$ and $-2e \le q_O \le 0$, respectively. Using the parameter values from the reference [36], the matrix J and vector $\boldsymbol{\chi}$ can be written as

$J = \begin{bmatrix} 5.1645 & 5.0 & 2.5 \\ 5.0 & 7.018 & 5 \\ 2.5 & 5 & 5.1645 \end{bmatrix}$ and $\boldsymbol{\chi} = \langle 0, \quad 5.485, \quad 0 \rangle$. The value of μ is then 3.9046, and that yields the charge vector to be $\mathbf{q} = \langle 9.3165, \quad -13.5003, \quad 9.3165 \rangle$. Obviously, the charge values of the aluminum and oxygen atoms exceed their bounds, so they have to be fixed at their limits. This means that the first and second aluminum atoms will carry $+3e$ and 0 charge while the oxygen atom will carry 0 charge. The result certainly violates the charge neutrality condition and therefore each atom is forced to only carry zero charge. The electrostatic energy then becomes $0\ eV$. In contrast, the correct result using a constrained optimization shows that the two aluminum atoms carry $+0.1428e$ charge and the oxygen atom carries $-0.2856e$ charge with the minimized energy of $-0.7834\ eV$.

Following the approach of Rappé and Goddard, Streitz and Mintmire [36] substituted point charges in Eq. (2.18) with a charge distribution function $\rho_q(r,q) = Z\delta(r) + (q - Z)f(r)$, where Z is an effective core charge ranging from zero to

the charge limit of an atom, $\delta(r)$ is a delta function, and $f_N(r)$ is a distribution function with $\int f_N(r)dr = 1$. Evidently, q is partitioned into $\rho_q(r,q)$ because $\int \rho_q(r,q)dr = q$. Charge values can be then algebraically solved for, using equilibrium conditions and neutrality as in the approach of Rappé and Goddard. Zhou et al. [37] pointed out two problems of the Streitz and Mintmire model: (1) charge instability and (2) validity of the model other than binary systems. Regarding the charge instability, an example of two point charges of equal magnitude but opposite sign (a neutral system) was chosen. Zhou et al. showed that when a distance between two ions falls below some critical value, a global minimum energy does not exist. Equation (2.18) has the global minimum when the first and second derivatives of the energy E_i^{es} with respect to the charge q_i (i.e. slope and concavity) are zero and positive, respectively. The second problem with the Streitz and Mintmire model is that it does not work when two or more metals are included in a system. Streitz and Mintmire set up their model such that oxidations would always occur among atoms within a given system, and they only studied binary systems (one metal and oxygen). If only metals are present but no oxygen, charge transfers will still occur as long as those metals possess different electronegativities. Although, this is physically correct, such charge transfers will violate the charge neutrality condition for a system with only metals but no oxidizing agents.

Zhou et al. [37] attempted to correct those errors in the Streitz and Mintmire model by modifying the original model with inclusion of a special weighing function and limiting values of charges into the electrostatic equation. To prevent charges from exceeding their bounds, the weighing variable acts as an energy penalty. That is, when charges are too close to their bounds, the additional energy terms incorporated with the

weighing variable and charge limits rapidly increases. According to this model, the electrostatic energy E_i^{es} of an atom i is:

$$E_i^{es}(q_i) = \left(\chi_i + \sum_j J_{ij} q_j\right) q_i + \omega\left(1 - \frac{q_i - q_i^L}{\left|q_i - q_i^L\right|}\right)\left(q_i - q_i^L\right)^2 + w\left(1 - \frac{q_i^U - q_i}{\left|q_i^U - q_i\right|}\right)\left(q_i^U - q_i\right)^2 \tag{2.19}$$

where q_i^L and q_i^U are the bounds for the charge of atom i, $q_i^L < q_i < q_i^U$ and the energy penalty w is defined to be 20.0. The modified model with the additional energy penalty terms cannot be solved algebraically. Zhou et al. used an unconstrained optimization to find an optimized set of charge values. The use of the auxiliary weighing variable is a complicated and indirect solution. As in the case of the Streitz and Mintmire model, this model lacks the actual charge constraints and suffers from the same charge divergence problem. To show this, the same simple case of an aluminum-oxygen pair that Zhou et al. used to prove the charge diversion in the Streitz and Mintmire model is reintroduced here. The electrostatic energy for a pair of Al-O in a neutral system can be written as:

$$E_{tot}^{es} = (\chi_O - \chi_{Al}) q_O + \left(\frac{J_O + J_{Al}}{2} - \frac{k_c}{r}\right) q_O^2 \tag{2.20}$$

according to the Streitz and Mintmire model and:

$$E_{tot}^{es} = \left[(\chi_O - \chi_{Al}) + 4w\left(q_{Al}^U - q_O^L\right)\right] q_O + \left(\frac{J_O + J_{Al}}{2} - \frac{k_c}{r} + 4\omega\right) q_O^2 + 2w\left[\left(q_O^L\right)^2 + \left(q_{Al}^U\right)^2\right] \tag{2.21}$$

according to the Zhou et al. model. To minimize E_{tot}^{es}, setting the first derivative with respect to q_O equal to zero yields $q_O = \frac{\chi_{Al} - \chi_O}{J_O + J_{Al} - 2k_c / r}$ for the Streitz and Mintmire

model and $q_O = \frac{\chi_{Al} - \chi_O - 4\omega\left(q_{Al}^U - q_O^L\right)}{J_O + J_{Al} - 2k_c / r + 8\omega}$ for the Zhou et al. model. Using the Streitz and Mintmire data (J_O = 14.036 eV, J_{Al} = 10.329 eV, χ_O =5.485 eV, and χ_{Al} = 0.0 eV) [36], the charges on the oxygen atom become $q_O = \frac{-5.485}{24.365 - 28.8/r}$ and $q_O = \frac{-5.485 - 4(20)\left(3-(-2)\right)}{24.365 - 28.8/r + 8(20)} = \frac{-405.485}{184.365 - 28.8/r}$ for the Streitz and Mintmire model and the Zhou et al. model, respectively. Figure 2.1 shows the oxygen ion charge as a function of the separation distance between the Al-O pair. The Streitz and Mintmire model gives a divergence at $1.18\,\mathring{\mathrm{A}}$, while the Zhou et al. model causes a divergence to occur at $0.15\,\mathring{\mathrm{A}}$. If a constrained optimization is applied, the oxygen charge will be limited to q_O^L, which is $-2e$, when a divergence is encountered.

This dissertation presents a much more direct way to implement a charge transfer model for molecular dynamic simulations. The idea is based on what Rappé and Goddard started. One important difference is that a constrained optimization is used with the original set of equations instead of solving them algebraically. At each time step, charges are adjusted so that the total energy in a system is minimized. The EAM potential is considered constant because all of the input information is known. So, minimizing the electrostatic potential is equivalent to minimizing the total energy of the system. The next section describes the applied algorithm in more details. A few sample simulations were also performed to test the validity of this code.

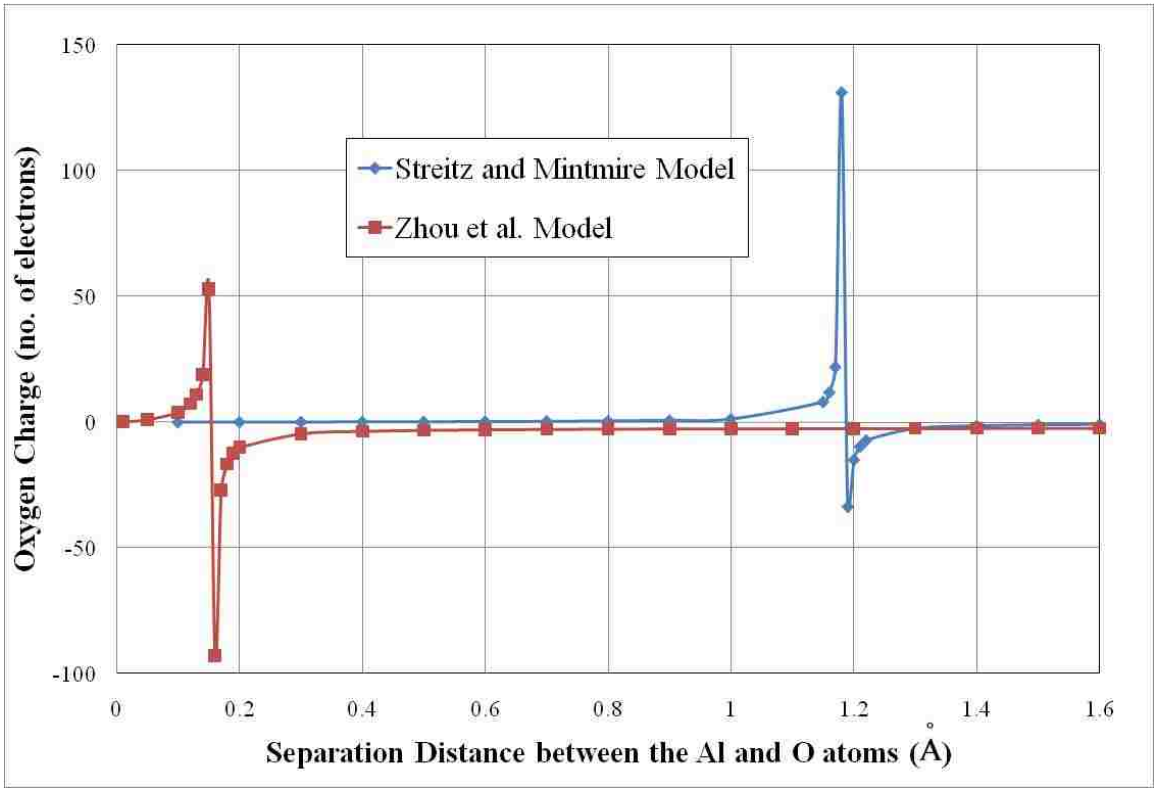

Figure 2.1 Charges on oxygen from the Streitz & Mintmire and Zhou et al. models

2.4 Optimization and Charge Transfer

In order to reach equilibrium, all systems try to lower their internal energies as much as possible. However, in a metal oxide system, there exist additional constraints on ion charges that have to be confined within their charge limits. This energy minimization, therefore, becomes a constrained optimization problem. The objective is to find an optimal set of charges that makes a total system energy as low as possible and yet all the charges are still within their physical limits and obey the charge neutrality condition. The original equation posed by Rappé and Goddard [34] serves as a good starting optimization problem. Hence, there is no need for new charge density functions

as Streitz and Mintmire [36] did, or the extra auxiliary terms in the Zhou et al. approach [37].

A general optimization problem can be described as:

Minimize $E(q_1, q_2, \ldots, q_n)$ (2.22)

Subject to: $h_k(q_1, q_2, \ldots, q_n) = 0$, $k = 1,2,\ldots,l$ (2.23)

$g_j(q_1, q_2, \ldots, q_n) \le 0$, $j = 1,2,\ldots,m$ (2.24)

$q_i^L \le q_i \le q_i^U$, $i = 1,2,\ldots,n$ (2.25)

where $E(q_1, q_2, \ldots, q_n)$ is the function to be minimized, electrostatic energy in this case as a function of n charges q_i's. Each charge q_i can only vary between its lower limit q_i^L and upper limit q_i^U. $h_k(q_1, q_2, \ldots, q_n)$ are the equality constraints, and there are l equality constraints in this optimization problem. $g_j(q_1, q_2, \ldots, q_n)$ are the inequality constraints, and this problem has m inequality constraints. In addition, an optimal set q^* of q_i's has to obey the Kuhn-Tucker conditions, which are stated as follows:

(1) $\nabla E(q^*) + \boldsymbol{\pi}^T \nabla g(q^*) + \boldsymbol{\lambda}^T \nabla h(q^*) = \mathbf{0}$

(2) $g_j(q^*) \le 0$ for all $j = 1,2,\ldots,m$

(3) $h_k(q^*) = 0$ for all $k = 1,2,\ldots,l$

(4) $\pi_j \ge 0$ for all $j = 1,2,\ldots,m$

(5) $\pi_j g_j(q^*) = 0$ for all $j = 1,2,\ldots,m$

where $\boldsymbol{\pi}$ and $\boldsymbol{\lambda}$ are vectors with their respective components π_i's and λ_j's, which are constants. The five conditions above are necessary for any solution that minimizes the function E under a given set of constraints.

There are four major direct methods to solve the general optimization problem above: (1) Sequential Linear Programming (SLP), (2) Sequential Quadratic Programming (SQP), (3) the Generalized Reduced Gradient (GRG) Method, and (4) Sequential Gradient Restoration Algorithm (SGRA) [38]. Other methods also exist but they offer only slight variations from these four principal methods. GRG is chosen to be used in this dissertation mainly because Solver, a sub-program in Microsoft Excel, is also implemented with GRG and it serves as an excellent benchmarking tool for result comparisons. The GRG method only deals with equality constraints. Therefore, all inequality constraints are converted into equality constraints with additional variables, called slack variables. The transformation can be written as:

$$\text{Minimize} \quad E(q_1, q_2, \ldots, q_n) \tag{2.26}$$

$$\text{Subject to:} \quad h_k(q_1, q_2, \ldots, q_n) = 0, \qquad k = 1,2,\ldots,l \tag{2.27}$$

$$g_j(q_1, q_2, \ldots, q_n) + q_{n+j} = 0, \qquad j = 1,2,\ldots,m \tag{2.28}$$

$$q_i^L \le q_i \le q_i^U, \qquad i = 1,2,\ldots,n \tag{2.29}$$

$$q_{n+j} \ge 0, \qquad j = 1,2,\ldots,m \tag{2.30}$$

$q_1, q_2, \ldots, q_n$ are the original variables, and $q_{n+1}, q_{n+2}, \ldots, q_{n+m}$ are the slack variables. The basic idea of the GRG method is to reduce the number of variables in a given optimization problem when searching for an optimal solution. The $n+m$ variables $q_1, q_2, \ldots, q_n, q_{n+1}, \ldots, q_{n+m}$, or in the vector notation $\mathbf{q} = (q_1, q_2, \ldots, q_n, q_{n+1}, \ldots, q_{n+m})$, are divided into two groups: basic variables $\mathbf{Y}$ and non-basic variables $\mathbf{Z}$. That is, $\mathbf{q} = (\mathbf{Z}, \mathbf{Y})^T$, where the superscript T indicates the transpose. The number of basic variables equals the number of constraints $m+l$, and these basic variables are expressed

in terms of the remaining $n-l$ non-basic variables. This essentially makes the optimization problem depend only on the $n-l$ non-basic variables $\mathbf{Z}$, and $\mathbf{q}=(\mathbf{Z},\mathbf{Y}(\mathbf{Z}))^T$. When non-basic variables are not fixed at their bounds, they are called super-basic variables. Super-basic variables determine search directions for a new feasible solution under a given set of constraints.

In terms of the basic variables $\mathbf{Y}=(y_1,y_2,\ldots,y_{m+l})$ and non-basic variables $\mathbf{Z}=(z_1,z_2,\ldots,z_{n-l})$, the reduced problem is restated as:

Minimize $E(\mathbf{Z},\mathbf{Y}(\mathbf{Z}))$ (2.31)

Subject to $\mathbf{H}(\mathbf{Z},\mathbf{Y}(\mathbf{Z}))=(\mathbf{h},\mathbf{g})^T=(H_1,H_2,\ldots,H_{l+m})^T=\mathbf{0}$ (2.32)

$z_i^L \le z_i \le z_i^U, \qquad i=1,2,\ldots,n-l$ (2.33)

$y_i^L \le y_i \le y_i^U, \qquad i=1,2,\ldots,m+l$ (2.34)

The superscripts L and U indicate the lower and upper limits, respectively, for each variable. Given a feasible starting point $\mathbf{q}_0$ that yields $\mathbf{H}(\mathbf{q}_0)=\mathbf{0}$, the reduced problem can be expanded at a point $\mathbf{q}=(\mathbf{Z},\mathbf{Y})^T$ about the current feasible point $\mathbf{q}_0=(\mathbf{Z}_0,\mathbf{Y}_0)^T$ (the first-order Taylor series):

Minimize $E(\mathbf{Z}_0+\Delta\mathbf{Z},\mathbf{Y}_0+\Delta\mathbf{Y})=E(\mathbf{q}_0)+\nabla_Z E(\mathbf{q}_0)^T\Delta\mathbf{Z}+\nabla_Y E(\mathbf{q}_0)^T\Delta\mathbf{Y}$ (2.35)

Subject to

$H_j(\mathbf{Z}_0+\Delta\mathbf{Z},\mathbf{Y}_0+\Delta\mathbf{Y})=H_j(\mathbf{q}_0)+\nabla_Z H_j(\mathbf{q}_0)^T\Delta\mathbf{Z}+\nabla_Y H_j(\mathbf{q}_0)^T\Delta\mathbf{Y}=0$ (2.36)

where $\Delta\mathbf{Z}=\mathbf{Z}-\mathbf{Z}_0=(\Delta Z_1,\Delta Z_2,\ldots,\Delta Z_{n-l})$ and $\Delta\mathbf{Y}=\mathbf{Y}-\mathbf{Y}_0=(\Delta Y_1,\Delta Y_2,\ldots,\Delta Y_{m+l})$ with ΔZ_i's and ΔY_i's are real numbers, ∇_Z and ∇_Y denote the differentials with respect to $\mathbf{Z}$ and $\mathbf{Y}$, respectively, and the index j runs from 1 to $l+m$. Therefore, $\nabla_{\mathbf{Z}}E(\mathbf{q}_0)^T$

and $\nabla_Z H_j(\mathbf{q}_0)^T$ are the $1\times(n-l)$ matrices $\left[\frac{\partial E(\mathbf{q}_0)}{\partial z_1} \quad \frac{\partial E(\mathbf{q}_0)}{\partial z_2} \quad \cdots \quad \frac{\partial E(\mathbf{q}_0)}{\partial z_{n-l}}\right]$ and

$\left[\frac{\partial H_j(\mathbf{q}_0)}{\partial z_1} \quad \frac{\partial H_j(\mathbf{q}_0)}{\partial z_2} \quad \cdots \quad \frac{\partial H_j(\mathbf{q}_0)}{\partial z_{n-l}}\right]$, respectively. Similarly, $\nabla_{\mathbf{Y}} E(\mathbf{q}_0)$ and

$\nabla_{\mathbf{Y}} H_j(\mathbf{q}_0)$ are the $1\times(m+l)$ matrices $\left[\frac{\partial E(\mathbf{q}_0)}{\partial y_1} \quad \frac{\partial E(\mathbf{q}_0)}{\partial y_2} \quad \cdots \quad \frac{\partial E(\mathbf{q}_0)}{\partial y_{m+l}}\right]$ and

$\left[\frac{\partial H_j(\mathbf{q}_0)}{\partial y_1} \quad \frac{\partial H_j(\mathbf{q}_0)}{\partial y_2} \quad \cdots \quad \frac{\partial H_j(\mathbf{q}_0)}{\partial y_{m+l}}\right]$, respectively.

To find a search direction for an optimal solution, define the matrices $\mathbf{A}$ and $\mathbf{B}$ as:

$$\mathbf{A} = \begin{bmatrix} \nabla_Z H_1^T \\ \nabla_Z H_2^T \\ \vdots \\ \nabla_Z H_{l+m}^T \end{bmatrix} \tag{2.37}$$

$$\mathbf{B} = \begin{bmatrix} \nabla_Y H_1^T \\ \nabla_Y H_2^T \\ \vdots \\ \nabla_Y H_{l+m}^T \end{bmatrix} \tag{2.38}$$

Equation (2.36) can then be rewritten more compactly as:

$$\mathbf{H}(\mathbf{q}) = \mathbf{H}(\mathbf{q}_0) + \mathbf{A}\Delta Z + \mathbf{B}\Delta Y = \mathbf{0} \tag{2.36a}$$

Recall that $\mathbf{H}(\mathbf{q}_0) = \mathbf{0}$, and this gives $\mathbf{A}\Delta Z + \mathbf{B}\Delta Y = \mathbf{0}$. Therefore,

$$\Delta\mathbf{Y} = -\mathbf{B}^{-1}\mathbf{A}\Delta Z \tag{2.39}$$

Substituting Eq. (2.39) into Eq. (2.35) yields Eq. (2.40) after a few steps of algebra:

$$E(\mathbf{q}) = E(\mathbf{q}_0) + \nabla_Z E(\mathbf{q}_0)^T \Delta\mathbf{Z} - \nabla_Y E(\mathbf{q}_0)^T \mathbf{B}^{-1}\mathbf{A}\Delta Z$$

$$E(\mathbf{q}) = E(\mathbf{q}_0) + \left\{\nabla_Z E(\mathbf{q}_0)^T - \nabla_Y E(\mathbf{q}_0)^T \mathbf{B}^{-1}\mathbf{A}\right\}\Delta\mathbf{Z}$$

$$E(\mathbf{q}) = E(\mathbf{q}_0) + \left\{\nabla_Z E(\mathbf{q}_0) - \left(\mathbf{B}^{-1}\mathbf{A}\right)^T \nabla_Y E(\mathbf{q}_0)\right\}^T \mathbf{\Delta Z}$$

$$E(\mathbf{q}) = E(\mathbf{q}_0) + (\mathbf{G_R})^T \mathbf{\Delta Z} \tag{2.40}$$

where $\mathbf{G_R} = \nabla_Z E(\mathbf{q}) - \left(\mathbf{B}^{-1}\mathbf{A}\right)^T \nabla_Y E(\mathbf{q})$ (2.41)

$\mathbf{G_R}$, the reduced gradient of the function $E(\mathbf{q})$, provides a search direction for an optimal solution. Below is the GRG implementation in finding an optimal solution (adapted from Ref. [38]):

GRG Algorithm:

Step 1. Choose:

- a starting set $\mathbf{q}^0$ of feasible q_i's ($h(\mathbf{q}) = 0$ must be zero)
- an initial number of iterations N_s
- an accuracy ε for convergence and stopping

Set $p = 1$ (iteration counter)

Step 2. Identify basic, non-basic, and super-basic variables

In the first iteration ($p = 1$), variables that are not basic are set to be super-basic

Calculate $\mathbf{G_R}$

Calculate an optimum step size α^* (see below)

Calculate $\mathbf{q}^p$

Step 3 Convergence and Termination:

Convergence for GRG

If the Kuhn-Tucker conditions are satisfied then STOP.

Stopping Criteria

- $\Delta q = \left| \mathbf{q}^{p} - \mathbf{q}^{p-1} \right|$

  If $\Delta q < \varepsilon$ then STOP.

- If $p = N_s$
  - Find the extrapolated maximum number of iterations $N_{\max}$
    - If $N_{\max} > N_s$ then set $N_s = N_{\max}$ else STOP.

Continue to the next iteration (increment p by one)

Go to step 2

Step size computation:

Step 1 Set $\mathbf{S} = -\mathbf{G_R}$

Step 2 Find a minimum α from a set of positive α's that make $\mathbf{Z}^{p}$ stay within its bound. Note that $\Delta\mathbf{Z} = \alpha\mathbf{S}$ and $\mathbf{Z}^{p} = \mathbf{Z}^{p-1} + \Delta\mathbf{Z}$.

Step 3 Use Eq. (2.39) to find α for $\mathbf{Y}^{p}$ that makes $\mathbf{Y}^{p}$ stay within its bounds.

Step 4 Solve $\frac{d}{d\alpha} E(\alpha) = 0$ for an α value that minimize $E(\alpha)$ (unconstrained α).

Step 5 Compare all the α's from Steps 2 to 4 and return a minimum α that confine all of the q_i's within their bounds

Step 6 If any of q_i's are at their bounds, set those q_i's to be non-basic variables. If one of those q_i's are formerly basic variables, pick new variables from the set of non-basic variables that stay approximately in the middle between their bounds to be new basic variables.

Based on Eqns. (2.31) to (2.34), the electrostatic (ES) energy minimization problem for a given set of n ions is structured as:

$$\text{Minimize} \qquad E_{tot}^{es}(\mathbf{q}) = \sum_{i=1}^{n}\left(\chi_i q_i + q_i \sum_{j=1}^{n} J_{ij} q_j\right) \tag{2.42}$$

$$\text{Subject to} \qquad h(\mathbf{q}) = \sum_{i=1}^{n} q_i = 0 \tag{2.43}$$

The ES energy minimization problem has only one equality constraint and no inequality constraint. That means $l = 1$ and $m = 0$. Therefore, this optimization problem has one basic variable and $n-1$ non-basic variables. Let the subscripts Y and Z associate with the basic and non-basic variables, respectively. Then, specifically to this problem in the vector notation, the basic variable is $\mathbf{Y} = (q_Y)$ and non-basic variables are $\mathbf{Z} = (q_{Z1}, q_{Z2}, \ldots, q_{Zn-1})$.

To find the reduced gradient $\mathbf{G_R}$, first calculate $\nabla_Z E(\mathbf{q})$. Equation (2.42) has its first derivative with respect to any charge q_s, which is one of the q_i's, as:

$$\frac{\partial E_{tot}^{es}}{\partial q_s} = \chi_s + \sum_{i=1}^{n}\left(J_{si} + J_{is}\right)q_i \tag{2.44}$$

The matrices **A** and **B** specific to this problem are:

$$\mathbf{A} = \nabla_Z h(\mathbf{q})^T = [1, \ldots, 1]_{1\times n-1} \tag{2.45}$$

$$\mathbf{B} = \nabla_Y h(\mathbf{q})^T = [1] \tag{2.46}$$

Thus, for a given step size of the non-basic variables in any search direction, the step size of the basic variable is given by:

$$\Delta Y = -\mathbf{B}^{-1}\mathbf{A}\Delta Z = -[1][1, \ldots, 1]\begin{bmatrix}\Delta Z_1 \\ \vdots \\ \Delta Z_{n-1}\end{bmatrix} = -\sum_{i=1}^{n-1}\Delta Z_i \tag{2.47}$$

The search direction $\mathbf{G_R}$ is shown in Eq. (2.48) below after a few steps of algebraic simplifications:

$$\mathbf{G_R} = \begin{bmatrix} \chi_1 + \sum_{i=1}^{n} (J_{1i} + J_{i1}) q_i \\ \vdots \\ \chi_Z + \sum_{i=1}^{n} (J_{Zi} + J_{iZ}) q_i \\ \vdots \\ \chi_{n-1} + \sum_{i=1}^{n} (J_{n-1,i} + J_{i,n-1}) q_i \end{bmatrix} - [1] \begin{bmatrix} 1 \\ \vdots \\ 1 \end{bmatrix} \left[\chi_Y + \sum_{i=1}^{n} (J_{Yi} + J_{iY}) q_i \right]$$

$$\mathbf{G_R} = \begin{bmatrix} \chi_1 + \sum_{i=1}^{n} (J_{1i} + J_{i1}) q_i \\ \vdots \\ \chi_Z + \sum_{i=1}^{n} (J_{Zi} + J_{iZ}) q_i \\ \vdots \\ \chi_{n-1} + \sum_{i=1}^{n} (J_{n-1,i} + J_{i,n-1}) q_i \end{bmatrix} - \begin{bmatrix} \chi_Y + \sum_{i=1}^{n} (J_{Yi} + J_{iY}) q_i \\ \vdots \\ \chi_Y + \sum_{i=1}^{n} (J_{Yi} + J_{iY}) q_i \\ \vdots \\ \chi_Y + \sum_{i=1}^{n} (J_{Yi} + J_{iY}) q_i \end{bmatrix}$$

$$\mathbf{G_R} = \begin{bmatrix} \vdots \\ \chi_Z - \chi_Y + \sum_{i=1}^{n} (J_{Zi} + J_{iZ}) q_i - \sum_{i=1}^{n} (J_{Yi} + J_{iY}) q_i \\ \vdots \end{bmatrix}$$

$$\mathbf{G_R} = \begin{bmatrix} \vdots \\ \chi_Z - \chi_Y + \sum_{i=1}^{n} (J_{Zi} - J_{Yi} + J_{iZ} - J_{iY}) q_i \\ \vdots \end{bmatrix} \tag{2.48}$$

Let G_{Ri} represent the i^{th} component of $\mathbf{G_R}$, which corresponds to q_{Zi}, the i^{th} component of the non-basic vector $\mathbf{Z}$. Then the Kuhn-Tucker conditions specific to the electrostatic (ES) energy minimization problem are:

(1) $G_{Ri} = 0$ when a non-basic variable q_{Zi} is strictly between its bounds.

(2) $G_{Ri} \geq 0$ when a non-basic variable q_{Zi} is at its lower bound.

(3) $G_{Ri} \le 0$ when a non-basic variable q_{Zi} is at its upper bound.

The above conditions are derived from the standard Kuhn-Tucker conditions mentioned earlier, and the derivation is presented here. The GRG method does not have any inequality constraints, except for the upper and lower bounds of each variable. In addition, the optimization problem only depends on the non-basic variables according to the GRG method, and so do the Kuhn-Tucker conditions. For the Kuhn-Tucker conditions, the bound restrictions on each non-basic variable can be transformed into the inequality constraints in the vector form as follows: the lower bound constraint $\mathbf{g}_Z^L = \left(q_{Z1}^L - q_{Z1}, \ldots, q_{Zi}^L - q_{Zi}, \ldots, q_{Zn-1}^L - q_{Zn-1}\right)$ and the upper bound constraint $g_Z^U = \left(q_{Z1} - q_{Z1}^U, \ldots, q_{Zi} - q_{Zi}^U, \ldots, q_{Zn-1} - q_{Zn-1}^U\right)$. The five standard Kuhn-Tucker (KT) conditions can be rewritten as:

(1) $\nabla_Z E(q^*) + \boldsymbol{\pi}^U - \boldsymbol{\pi}^L + \boldsymbol{\lambda} = \mathbf{0}$

(2) $g_i^L(q^*) \le 0$ and $g_j^U(q^*) \le 0$ (always true by the problem statement)

(3) $h_k(q^*) = 0$ (always true by the problem statement)

(4) $\pi_i^L \ge 0$ and $\pi_j^U \ge 0$

(5) $\pi_i^L g_i^L(q^*) = 0$ and $\pi_j^U g_j^U(q^*) = 0$

where π_i^L and π_j^U are the i^{th} and j^{th} components of $\boldsymbol{\pi}^L$ and $\boldsymbol{\pi}^U$, respectively. Based on the bound constraints of the non-basic variables, the Kuhn-Tucker conditions differ in each of the three possible cases: $q_{Zi}^L < q_{Zi} < q_{Zi}^U$, $q_{Zi}^L = q_{Zi}$, and $q_{Zi} = q_{Zi}^U$. If a non-basic variable is strictly between its lower and upper bounds $\left(q_{Zi}^L < q_{Zi} < q_{Zi}^U\right)$ then its inequality constraint is less than zero $\left(g_i^L(q^*) < 0 \text{ and } g_i^U(q^*) < 0\right)$. This leads to $\pi_i^L = \pi_i^U = 0$ as

required by $\pi_i^L g_i^L(q^*) = 0$ and $\pi_j^U g_j^U(q^*) = 0$ (KT Condition 5). That consequently yields $\frac{\partial}{\partial q_{Zi}} E(q^*) + \lambda_i = 0$. Recall that $\mathbf{G_R} = \nabla_Z E(\mathbf{q}) - \left(\mathbf{B}^{-1}\mathbf{A}\right)^T \nabla_Y E(\mathbf{q})$ and define $\boldsymbol{\lambda} \equiv -\left(\mathbf{B}^{-1}\mathbf{A}\right)^T \nabla_Y E(\mathbf{q})$. This finally leads to $G_{Ri} = 0$. Next, when a non-basic variable is at its lower bound $\left(q_{Zi} = q_{Zi}^L\right)$, $\pi_i^L \geq 0$ per KT Condition 4 but $\pi_i^U = 0$ because all g_i^U's are less than zero and $\pi_j^U g_j^U(q^*) = 0$ at all time. Therefore, $\frac{\partial}{\partial q_{Zi}} E(q^*) + \lambda_i + \pi_i^L = 0$ and this leads to $G_{Ri} - \pi_i^L = 0$. Since $\pi_i^L \geq 0$, it is certain that $G_{Ri} \geq 0$. In the same fashion, when a non-basic variable is at its upper bound $\left(q_{Zi} = q_{Zi}^U\right)$, $\pi_i^U \geq 0$ per KT Condition 4 but $\pi_i^L = 0$ because all g_i^L's are less than zero and $\pi_i^L g_i^L(q^*) = 0$ at all time. So, $\frac{\partial}{\partial q_{Zi}} E(q^*) + \lambda_i + \pi_i^U = 0$. This gives $G_{Ri} + \pi_i^U = 0$, and certainly $G_{Ri} \leq 0$ because $\pi_i^U \geq 0$.

Using the GRG algorithm, resulting charge distributions in different environments can be determined. The GRG code has been written in the C language specifically for this dissertation with over 1,000 lines of coding. To validate the self-written GRG code, the same inputs were entered in Excel's Solver, which is also implemented with GRG. The results from Solver and the self-written GRG code were found to be in excellent agreement. In most cases, they produced the same results, and, in a few cases, the self-written GRG code yielded better results.

To illustrate the benchmarking with Excel's Solver, the result from a sample case is reported here. In this case, a calculation cell contains 6 atoms: one aluminum atom and

five oxygen atoms. Using the same data as in Ref. [36], the J matrix according to Eq. (2.16) is

$$J = \begin{bmatrix} 7.017858 & 3.556027 & 11.926355 & 2.990698 & 3.824473 & 3.555971 \\ 3.556027 & 7.017858 & 3.103051 & 2.878696 & 11.926355 & 2.514477 \\ 11.926355 & 3.103051 & 7.017856 & 3.344118 & 3.556021 & 4.241726 \\ 2.990698 & 2.878696 & 3.344117 & 5.164328 & 3.523528 & 2.386254 \\ 3.824473 & 11.926350 & 3.556021 & 3.523528 & 7.017858 & 2.924555 \\ 3.555971 & 2.514477 & 4.241726 & 2.386254 & 2.924555 & 7.017858 \end{bmatrix}$$

The charge vector representing the aluminum charge q_{Al} and oxygen charges q_O^i is $\left\langle q_O^1, \quad q_O^2, \quad q_O^3, \quad q_{Al}, \quad q_O^4, \quad q_O^5 \right\rangle$ with the unit in e (electron charge). Table 2.1 shows the results from the code written for this dissertation and Excel's solver.

Table 2.1 Comparison between the self-written GRG code and Excel's Solver

	q_O^1	q_O^2	q_O^3	q_{Al}	q_O^4	q_O^5
Self-written code	-0.00055	0	0	0.00198	-0.00097	-0.00046
Excel's Solver	-0.00055	1.12E-15	0	0.00198	-0.00097	-0.00046

2.5 Results from Sample Simulations

Sample molecular dynamics simulations were run using Moldy [22], a computer code for molecular dynamic simulations with the same potential parameters as in Ref. [36]. Moldy has been modified to accommodate the GRG algorithm and the EAM potential. A test system is consisted of a 12.1482 $\mathring{A}$ thick semi-infinite aluminum slab with oxygen on both sides of the slab. Aluminum atoms are arranged in a face-centered cubic (FCC) structure with a lattice parameter of 0.40494 nm. At the beginning, all

atoms are neutral and hence the overall system is neutral. Moldy divides an original user defined space into smaller sub-cells to make calculations faster. In each sub-cell, a sub-routine named GRG is called to pre-compute a charge distribution within that sub-cell. The information on the charge distribution is then fed to a sub-routine that calculates forces and energy. Currently, we consider only simple ionic bonding. If electrons cannot be transferred within that sub-cell, GRG will leave the charge distribution as it is. As long as metals and oxidizing agents exist in a sub cell, charge transfers will always occur. The modified Moldy can take systems that include any metals and halogens (other than oxygen).

Three test runs were performed. Each differs by the type of oxygen on both sides of the aluminum slab: single-layered oxygen atoms, single-layered oxygen molecules, and double-layered oxygen molecules. The temperature was kept relatively constant at 300 K using a Nosé -Hoover heat bath. Each run lasted 10 picoseconds (ps) with 20,000 time steps. The visualization software called VMD [23] was used to render snapshots of the system. Figure 2.2 shows the initial setup of the aluminum slab with two layers of oxygen molecules. Figure 2.3 shows the oxidized slab at the end of the 10-ps run. The radial distribution functions (RDF) for Al-O are shown in Fig. 2.4. Two dominant Al-O peaks in the RDF suggest that the first and second nearest bond lengths between Al and O are about 1.8 - 1.9 $\mathring{A}$ and 2.2 - 2.3 $\mathring{A}$, respectively. These results agree well with the published experimental [39 – 43] and computational [44 – 47] results of alumina (Al_2O_3) as shown in Table 2.2.

Table 2.2 First nearest bond lengths of the aluminum-oxygen pair in Å

This work	Lamparter and Kniep [43]	Campbell et al. [44]	Hasnaoui et al. [45]
1.8 – 1.9 Å	1.8 Å	1.8 Å	1.8 Å

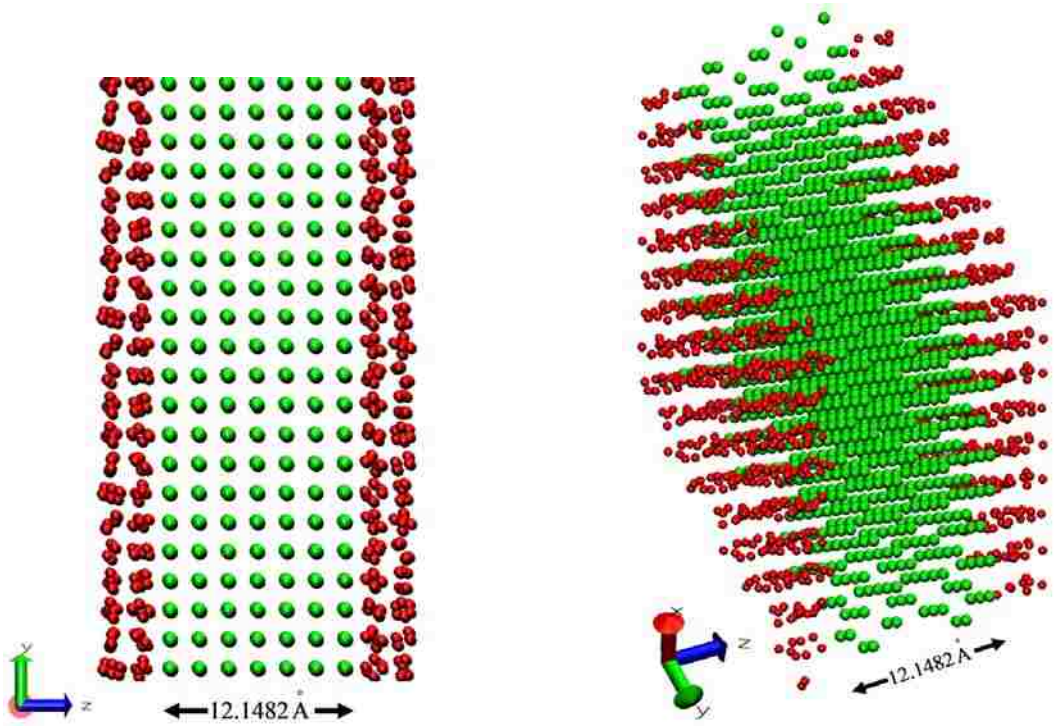

(a) (b)

Figure 2.2 Initial setup of the 12.1482 Å thick aluminum slab (green color) and two layers of O_2 (red color). (a) The x-z plane view. (b) The perspective view.

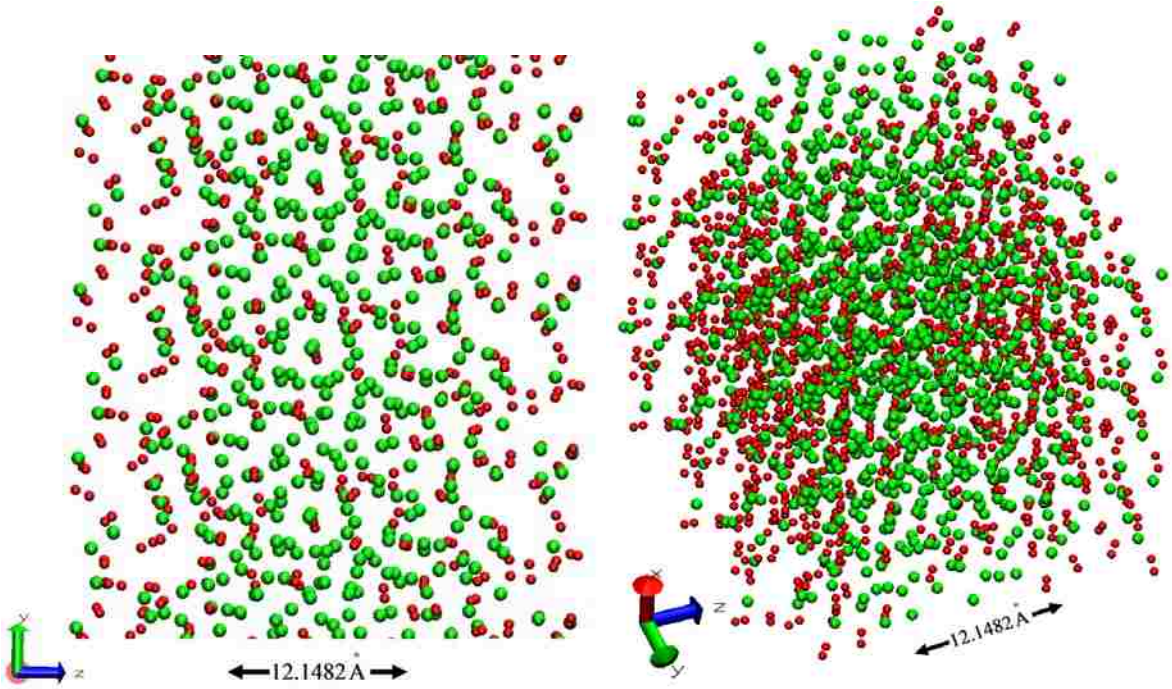

(a) (b)

Figure 2.3 After 10 ps, the oxidized aluminum slab expands its thickness to about 36 Å.

(a) The x-z plane view. (b) The perspective view.

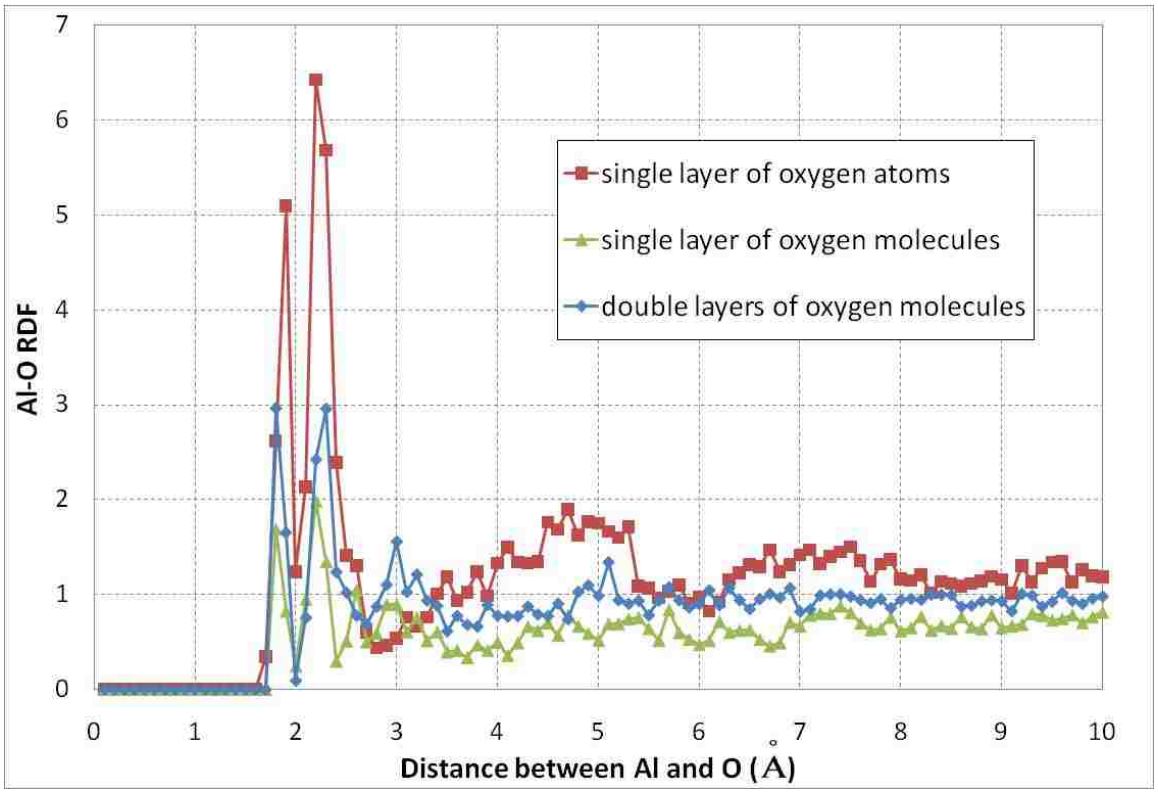

Figure 2.4 Al-O radial distribution functions

2.6 Conclusion

This chapter introduces a new approach to solve the original problem presented by Rappé and Goddard. Streitz and Mintmire and, later, Zhou et al. also attempted to solve the same problem by adding additional functions and variables. Their approaches arrive at correct solutions, but turn out to be unnecessarily complicated. This new approach takes a step back to the original equations and solves them directly using an optimization method called the generalized reduced gradient (GRG) method. This GRG approach can be implemented in any MD simulations for metal/metal oxide systems.

CHAPTER 3

OXIDATION MODELING OF IRON IN MAGNETITE FORM

3.1 Introduction

Pure iron is very susceptible to oxidation. Depending on the temperature, oxide layers are formed in a mixture of two or three types of iron oxides [48]. Above 570 °C, oxide layers consist of all three types of iron oxides: hematite (Fe_2O_3), magnetite (Fe_3O_4), and wüstite (FeO). Wüstite (FeO) does not form when the temperature is below 570 °C. The sequence of oxide layers is shown in Fig. 3.1. The Fe_2O_3 layer always occupies the outermost region. The Fe_3O_4 layer forms next to the hematite layer. Finally, at the innermost region lies the FeO layer. This formation sequence sets in the order of increasing oxygen partial pressure from the metal surface to the atmospheric environment. Fe_2O_3 is oxygen rich and sustained by high oxygen concentration at the outermost region. FeO is iron rich and it can form with less oxygen concentration at the innermost region, while Fe_3O_4 is the intermediate between the two.

Temperature and oxygen partial pressure affect oxide layer growth. As the total thickness of all oxide layers increases during oxidation, the relative thickness among oxide layers remains about the same [48]. Above 570 °C, the Fe_2O_3:Fe_3O_4: FeO thickness ratio ranges from 1:10:50 to 1:10:100. For example, at 1000 °C the Fe_2O_3:Fe_3O_4: FeO thickness ratio is 1:4:95 [49]. Below 570 °C, the Fe_3O_4 layer is thicker than the Fe_2O_3 layer with the Fe_3O_4:Fe_2O_3 thickness ratio approximately 10:1. Since corrosion and oxidation in lead-cooled reactors is of interest in this dissertation, the temperature domain will be limited to below 570 °C (the operating temperature of current lead-cooled reactors is about 550 °C) with oxide layers consisting of Fe_3O_4 and Fe_2O_3. In

addition, due to the relatively thick Fe_3O_4 layer, iron oxide is assumed to be purely Fe_3O_4 for simplicity.

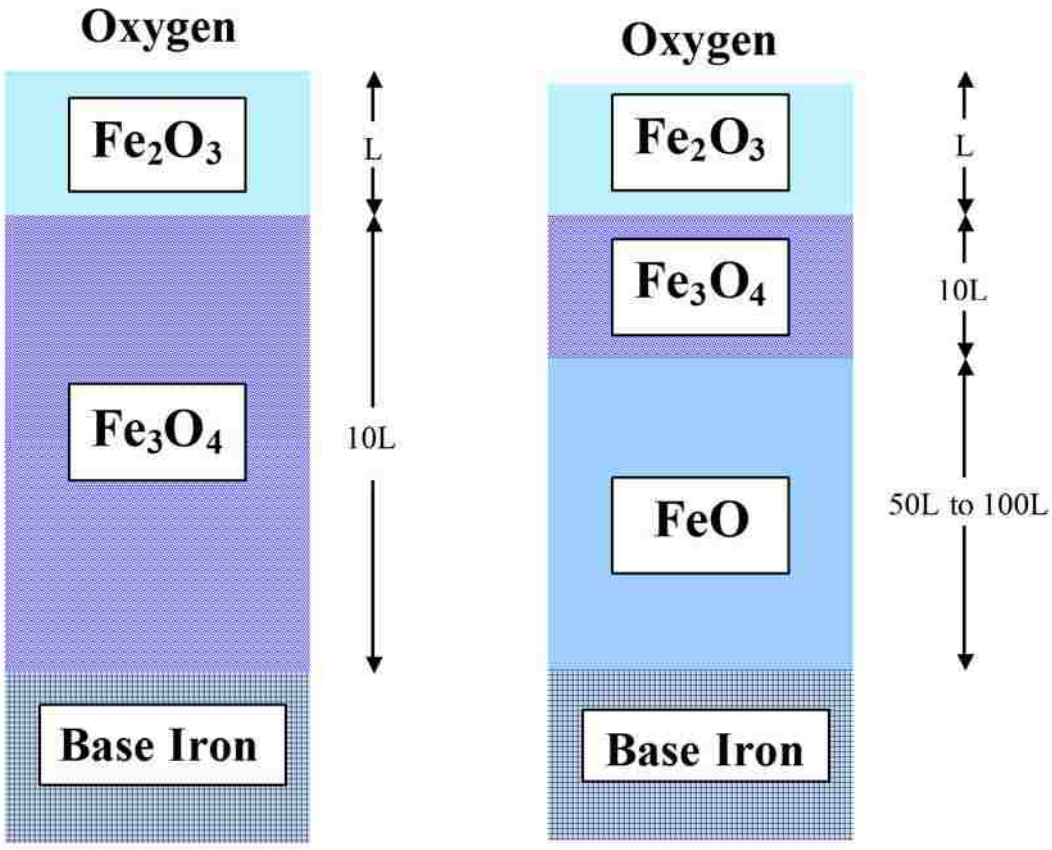

(a) (b)

Figure 3.1 Different oxide types and their respective thicknesses in iron oxidation depending on the temperature (thickness in an arbitrary unit L, not drawn to scale). (a) Below 570 °C (b) Above 570 °C

3.2 Parameter Fittings for Pure Materials (Iron and Oxygen)

The first step in modeling is to find appropriate potentials for all species in a system. Since this chapter involves iron oxidation, a series of parameters for iron and

oxygen have been fitted to the pair and EAM potentials, Eqns. (2.2) and (2.5), respectively. Equations (2.2) and (2.5) contain six variables, and therefore, a set of six equations are needed in parameter fitting. The set of six equations usually comes from crystal properties such as cohesive energy, equilibrium distance, bulk modulus, pressure derivative of bulk modulus, and elastic constants. Equations (3.1) to (3.4) are the first four equations in the set, which can be obtained from cohesive energy E_c, equilibrium pressure $P = 0$, bulk modulus $\tilde{B}$, and pressure derivative of bulk modulus $d\tilde{B}/dP$, respectively. All the derivatives are evaluated at $r = r_e$, the first nearest neighbor distance of a crystal at equilibrium.

$$E = \frac{1}{2}\sum_i \sum_{j \neq i} \phi(r_{ij}) + \sum_i F_i(\rho_i) + \sum_i E_i^{es} = E_c \tag{3.1}$$

$$\frac{dE}{dr} = 0 \tag{3.2}$$

$$\frac{r_e^2}{9\Omega_0}\frac{d^2E}{dr^2} = \tilde{B} \tag{3.3}$$

$$-1 - \frac{1}{r_e}\frac{d^3E/dr^3}{d^2E/dr^2} = \frac{d\tilde{B}}{dP} \tag{3.4}$$

Equation (3.5) below gives a theoretical elastic constant C_{IJ}, which can provide two more equations for parameter fittings:

$$\begin{aligned}\Omega_0 C_{IJ} = {} & F''\left(\sum \frac{X_I f'}{r}\right)\left(\sum \frac{X_J f'}{r}\right) + F'\sum \frac{X_I X_J f'}{r^2}\left(f'' - \frac{f'}{r}\right) \\ & + \frac{1}{2}\sum \frac{X_I X_J}{r^2}\left(\varphi'' - \frac{\phi'}{r}\right)\end{aligned} \tag{3.5}$$

with $X_I = x_i x_j$, where x_i's are Cartesian coordinates. The primes on the F and f functions indicate derivatives with respect to ρ and r, respectively. The elastic

constants C_{IJ} are completely symmetric. That is, $C_{IJ} = C_{JI}$. Using the Voigt notation, a pair of Cartesian indices ij from Eq. (3.5) is replaced by a single index I according to Table 3.1. For examples, $X_1 = x_1 x_1$ and $X_4 = x_3 x_2$.

Table 3.1 The Voigt notation

ij	11	22	33	32 or 23	31 or 13	21 or 12
I	1	2	3	4	5	6

In parameter fittings for pure materials like iron, Eqns. (3.1) and (3.5) can be further simplified. The electrostatic term in Eq. (3.1) can be neglected, and the term involving F' in Eq. (3.5) is zero (see Eq. (2.11)). For pure materials with cubic structures, the elastic constants C_{11}, C_{12}, and C_{44} are usually used in parameter fittings, and they can be found from Eq. (3.5):

$$\Omega_0 C_{11} = F''\left(\sum \frac{x^2 f'}{r}\right)^2 + \frac{1}{2}\sum \frac{x^4}{r^2}\left(\varphi'' - \frac{\phi'}{r}\right) \tag{3.6}$$

$$\Omega_0 C_{12} = F''\left(\sum \frac{x^2 f'}{r}\right)^2 + \frac{1}{2}\sum \frac{x^2 y^2}{r^2}\left(\varphi'' - \frac{\phi'}{r}\right) \tag{3.7}$$

$$\Omega_0 C_{44} = \frac{1}{2}\sum \frac{x^2 y^2}{r^2}\left(\varphi'' - \frac{\phi'}{r}\right) \tag{3.8}$$

Another data point to be fitted is the relationship between elastic constants C_{ij}'s and the bulk modulus $\tilde{B}$ given by the Voigt equation:

$$9\tilde{B} = (C_{11} + C_{22} + C_{33}) + 2(C_{12} + C_{13} + C_{23}) \tag{3.9}$$

The starting values of the parameters were taken from the EAM database developed by Zhou et al. [50]. Table 3.2 shows the resulting parameters for iron in Body Centered Cubic (BCC) structure. The fitting results are compared to the target values in Table 3.3.

Table 3.2 Parameter values for iron

Fitted Parameters	Values
A	0.387830322 eV
B	0.555639102 eV
α	9.523030631
β	5.145940759
F_0	-2.913740839 eV
η	0.725524773

The pair and EAM potentials of oxygen atoms were fitted from the properties of alpha solid oxygen using the first nearest atomic neighbors. The cohesive energy, equilibrium distance, bulk modulus, pressure derivative of bulk modulus, elastic constants, and average phonon frequency were used in determining the oxygen potential parameters. Although the literature describes a few ways to find zero wave vector frequencies from potential energy, the described methods are quite complicated and cumbersome [51]. A simplified approach based on the first nearest neighbor approximation is presented here.

Table 3.3 Comparison between the fitted and target values for the iron potentials

Properties	Fitted Values	Target Values
Cohesive Energy (eV)	-4.27	-4.29
Equilibrium Pressure (GPa)	0	0
Bulk Modulus (GPa)	180.79	170.35
C_{11} (GPa)	174.91	239.55
C_{12} (GPa)	183.72	135.75
C_{44} (GPa)	111.17	120.75

The kinetic energy E_k is given by:

$$2E_k = \sum_i m_i \left(\frac{d\xi_i}{dt} \right)^2 = \sum_i m_i \dot{\xi}_i^2 \tag{3.10}$$

where ξ_i is a coordinate of an atom in a crystal and m_i is an associated mass of that atom. When atom displacements from their original positions are small, the potential U can be expanded as:

$$2U = 2U_o + 2\sum_i \left(\frac{dU}{d\xi_i} \right)\Bigg|_o q_i + \sum_i \sum_j \left(\frac{d^2U}{d\xi_i d\xi_j} \right)\Bigg|_o \xi_i \xi_j + \ldots \tag{3.11}$$

Choosing the equilibrium energy to be zero, as well as the zero force $\frac{dU}{d\xi_i} = 0$, and ignoring higher-ordered terms, the above equation for small vibrations becomes:

$$2U = \sum_i \sum_j d_{ij} \xi_i \xi_j \tag{3.12}$$

where $d_{ij} = \frac{d^2U}{d\xi_i d\xi_j} = d_{ji}$. Newton's equations of motion can be written in the form:

$$\frac{d}{dt}\frac{\partial E_k}{\partial \dot{\xi}_k} + \frac{\partial U}{\partial \xi_k} = 0 \tag{3.13}$$

Or,

$$\ddot{\xi}_k + \sum_i d_{ik}\xi_i = 0 \tag{3.14}$$

Assume the solution is in the form:

$$\xi_k = A_k \exp\left(i\left(\vec{k}\cdot\vec{r} - \omega t\right)\right) \tag{3.15}$$

where A_k is the wave amplitude, $\vec{k}$ is the wave vector, $\vec{r}$ is the space vector, ω is the angular frequency, and t is time. For $\vec{k} = 0$ (zero wave number), Eq. (3.15) becomes

$$\xi_k = A_k \cos\left(\omega t + \varepsilon\right) \tag{3.16}$$

where ε is the starting phase of the wave. Equation (3.16) represents a wave equation with zero wave number (k = 0). Substituting the assumed solution of ξ_k, it can be rewritten as:

$$\begin{bmatrix} d_{11} - m_1\omega^2 & d_{12} & \cdots & d_{1N} \\ d_{21} & d_{22} - m_2\omega^2 & \cdots & d_{2N} \\ \cdots & \cdots & \cdots & \cdots \\ d_{N1} & d_{N2} & \cdots & d_{NN} - m_N\omega^2 \end{bmatrix} \begin{bmatrix} \xi_1 \\ \xi_2 \\ \vdots \\ \xi_N \end{bmatrix} = 0 \tag{3.17}$$

The values of $\xi_k = A_k \cos\left(\omega t + \varepsilon\right)$ can be found by calculating the determinant:

$$\begin{vmatrix} d_{11} - m_1\omega^2 & d_{12} & \cdots & d_{1N} \\ d_{21} & d_{22} - m_2\omega^2 & \cdots & d_{2N} \\ \cdots & \cdots & \cdots & \cdots \\ d_{N1} & d_{N2} & \cdots & d_{NN} - m_N\omega^2 \end{vmatrix} = 0 \tag{3.18}$$

In the case of alpha solid oxygen, using the first neighbor approximation, the above determinant becomes:

$$\begin{vmatrix} -m\omega^2 & 0 & 0 \\ 0 & -m\omega^2 & 0 \\ 0 & 0 & \frac{\partial^2 E}{\partial r^2} - m\omega^2 \end{vmatrix} = 0 \tag{3.19}$$

which gives;

$$\omega^2 = \frac{1}{m}\frac{\partial^2 E}{\partial r^2} \tag{3.20}$$

Combining Eqns. (3.3) and (3.20) yields

$$\omega^2 = \frac{9\Omega_0 \tilde{B}}{m r_e^2} \tag{3.21}$$

Equation (3.21) gives the average of phonon frequency for oxygen. The reported values of ω^2 are $0.9 \times 10^{26} s^{-2}$ and $4.7 \times 10^{26} s^{-2}$ [52]. Table 3.4 below shows the fitting results with all the six data points. The corresponding parameters are shown in Table 3.5. These parameters will be used in finding a set of parameters for iron oxides.

Table 3.4 The fitted and target values of the potential energy model for solid oxygen

Properties	Fitted Values	Target Values
Cohesive Energy E_c (eV)	-2.6	-2.6
Equilibrium Pressure (GPa)	0	0
Bulk Modulus $\tilde{B}$ (GPa)	2.98	2.96
Pressure Derivative	7.76	7.78
Zero wave number frequency ω $(\times 10^{26} s^{-2})$	1.2	0.9 and 4.7
Bulk Modulus from elastic constants $\tilde{B}$ (GPa)	1.43	2.96

Table 3.5 The parameter values of the potential energy model for solid oxygen

Parameters for Oxygen Atoms	Parameter Values
α	24.1176647
β	2.660324226
A (eV)	0.011228337
B (eV)	0.069658629
F_o (eV)	-2.564913
η	0.084502875

A test run was performed to validate the oxygen potential parameters, and a serious problem was discovered. Oxygen did not diffuse out to nearby empty space as expected. Instead, the oxygen atoms stayed together as groups. This tight binding was caused by a too strong attractive part in the O-O potential as the potential was intended for atom-atom interactions. Therefore, another novel approach is implemented for oxygen. The basic idea of this approach is to have two different potentials for oxygen: one for oxygen molecules (O_2) and another one for oxygen atom (O). Each oxygen molecule and oxygen atom will be modeled in the same form, say a hard ball sphere. One hard ball sphere will represent an oxygen molecule when that sphere has no charge. However, when it carries a negative charge, it will be morphed into an oxygen atom (or ion rather). Charges on oxygen ions will be determined from the electrostatic energy minimization.

Table 3.6 shows the parameter values for O_2-O_2 pair potential. The fitting was again based on the crystal structure of alpha solid oxygen. It is further assumed that the embedded atom method (EAM) energy is small and can be neglected because only oxygen molecules are considered, instead of oxygen atoms as done previously. Therefore, only the O_2-O_2 pair potential parameters were fitted. Fitting requires four data points for four fitting parameters (A, B, α, and β). The data points are cohesive energy, equilibrium pressure, bulk modulus, and pressure derivative of bulk modulus. All the data points are the same values as used in the O-O fitting, except for the cohesive energy. Now the cohesive energy represents interactions between two oxygen molecules, not two oxygen atoms. The cohesive energy is calculated from the classical Lennard-Jones potential with the neighboring molecules up to $10\,\mathring{\mathrm{A}}$. The O_2-O_2 Lennard-Jones pair potential U as a function of separation distance r is

$$U = 4\varepsilon\left(\left(\frac{\sigma}{r}\right)^{12} - \left(\frac{\sigma}{r}\right)^{6}\right) \tag{3.22}$$

where $\varepsilon = 113/k_B$ K and $\sigma = 3.433\,\mathring{\mathrm{A}}$ (k_B is the Boltzmann constant) [53].

Table 3.6 The pair potential parameters for oxygen molecules

Pair Potential Parameters	O_2-O_2
A	0.063474454 eV
B	0.079479388 eV
α	10.59191243
β	7.128116452

Table 3.7 The fitted and target values for the O_2-O_2 pair potential

	Fitted Values	Target Values
Cohesive Energy (eV/molecule)	-0.072	-0.072
Pressure (GPa)	0.000266	0
Bulk modulus (GPa)	2.96	2.96
Pressure derivative of $\tilde{B}$	5.15	7.78

3.3 Parameter Fittings for Iron Oxides

All three iron oxides (FeO, Fe_2O_3 and Fe_3O_4) have different crystal structures. Wüstite (FeO) has the rock salt (NaCl) structure (space group (SG) number 225, Fm-3m) with the lattice parameter $a = 4.3108\,\mathring{A}$ [54]. The fractional coordinates for Fe and O in wüstite are (0, 0, 0) and (0.5, 0.5, 0.5), respectively. Hematite (Fe_2O_3) has the corundum (α -Al_2O_3) structure, belonging to the space group R-3c (SG number 167) with the lattice parameters $a = 5.038\,\mathring{A}$ and $c = 13.772\,\mathring{A}$ [55]. The fractional coordinates for Fe and O in hematite are (0, 0, 0.3553) and (0.3059, 0, 0.25), respectively. Magnetite crystals have the inverse-spinel structure (SG number 227, Fd-3m) with tetrahedral and octahedral sites reserved for iron ions (see Fig. 3.2). A tetrahedral atom sits in the center of a tetrahedron formed by four other lattice atoms (three in-plane atoms and the fourth atom at the symmetrical position on top). An octahedral site for an (interstitial) atom is the space in the interstices between 6 regular atoms that form an octahedra. Four regular atoms are positioned in a plane, and the other two are in a symmetrical position just above or below. One Fe^{3+} ion per formula resides at tetrahedral sites while the Fe^{2+} and the remaining Fe^{3+} ions randomly reside at octahedral sites. The fractional coordinates for Fe^{3+}, Fe^{2+}, and O

in magnetite are (0.125, 0.125, 0.125), (0.5, 0.5, 0.5), and (0.2549, 0.2549, 0.2549), respectively, with the lattice parameter $a = 8.3941\,\mathring{\mathrm{A}}$ [56].

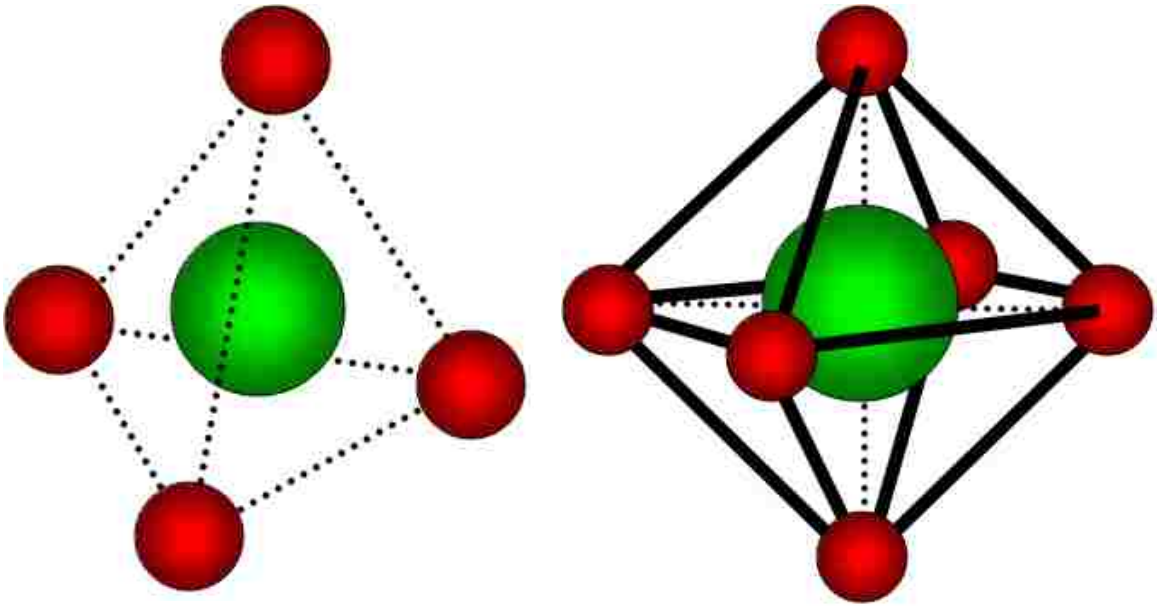

(a) (b)

Figure 3.2 A tetrahedral site in green color is shown in (a) and a octahedral site in green color is shown in (b).

Charges on ions become crucial in fitting pair potential parameters for oxides. Suppose that a reaction between x mol of a metal M and y mol of oxygen O results in an oxide compound $M_x O_y$. The electrostatic energy of one M ion from Eq. (2.15) can be rewritten as

$$E_M^{es} = E(0) + \chi_M q_M + \frac{1}{2} J_M q_M^2 + \frac{1}{2} \frac{\alpha_M k_C q_M q_O}{r_e} \tag{3.23}$$

where α_M is a Madelung constant, which is a real number representing a specific geometric arrangement in a crystal. For example, any crystal with the rock salt (NaCl)

structure will have the Madelung constant of 1.748. Using the neutrality condition that $xq_M + yq_O = 0$, Eq. (3.23) can be rewritten as:

$$E_M^{es} = E(0) + \chi_M q_M + \frac{1}{2}\left(J_M - \frac{x}{y}\frac{\alpha_M k_C}{r_e} \right) q_M^2 \tag{3.24}$$

If assuming that $E(0)$ is independent of q_M, minimizing the electrostatic energy in Eq. (3.24) gives the charges on M and O ions at equilibrium. In order for E_M^{es} to be an absolute minimum, dE_M^{es}/dq_M and $d^2E_M^{es}/dq_M^2$ must be zero and greater than zero respectively.

$$\frac{dE_M^{es}}{dq_M} = \chi_M + \left(J_M - \frac{x}{y}\frac{\alpha_M k_C}{r_e} \right) q_M = 0 \tag{3.25}$$

$$\frac{d^2E_M^{es}}{dq_M^2} = J_M - \frac{x}{y}\frac{\alpha_M k_C}{r_e} > 0 \tag{3.26}$$

Using the data from Tables 3.8 and 3.9, the resulting values of q_M and $d^2E_M^{es}/dq_M^2$ are shown in Table 3.10. Clearly, the value of $d^2E_M^{es}/dq_M^2$ indicates that the charge value q_M renders the function E_M^{es} to be an absolute maximum, instead of an absolute minimum as hoped for.

This error results from the initial assumption that an absolute minimum of the electrostatic energy exists for any given set of atomic and crystalline properties (χ, J, α_M and r_e). Since the absolute minimum does not exist, a relative or local minimum of the electrostatic energy should be sought. Mathematically, the local minimum must exist at either lower or upper charge limits of q_M. However, these limits are not the same as the absolute charge limits known for each ion (for example, iron ions can carry charges up to $+3e$, where e is the number of electrons). To illustrate this, let the upper bounds

on the iron ions in FeO and Fe_2O_3 be $+2e$ and $+3e$, respectively, when finding the local minimum electrostatic energy. Equation (3.25) gives the local minimums of FeO and Fe_2O_3 when q_M equal to 0 and $+3e$, respectively, when confining the ion charges to their physical limits. The $+3e$ iron ion charge in Fe_2O_3 might be acceptable. However, the iron ion charge in FeO has to be zero, which clearly contradicts the notion that ions have to carry non-zero charges. As a result, the physical charge limits are not applicable in this case. Without knowing an appropriate bound, which is a subset of the physical charge bounds, the usual practice of finding minima using Eqns. (3.25) and (3.26) becomes invalid. The common solution to get around this problem is to perform equilibrium charge findings and parameter fittings to experimental quantities simultaneously [58]. One way to this is to start out with $q_M = 0$ and gradually vary q_M until it reaches its physical bound. The best fitting will give the smallest error in the least squared fitting.

Table 3.8 Ion energetics data of iron and oxygen [57]

	Fe	O
Ionization Energy IE (eV)	7.9024	13.61806
Electron Affinity EA (eV)	0.1510	1.461112
Electronegativity χ (eV)	4.0267	7.539754
Self-coulomb Repulsion J (eV)	7.7514	12.156691

Table 3.9 Values used in calculating equilibrium charges of iron ions

	FeO	Fe_2O_3
x	1	2
y	1	3
α_M	1.747565	2.347099
r_e ($\mathring{A}$)	2.1554	1.9457

Table 3.10 Charge extrema and concavity of iron oxide ES energy

	FeO	Fe_2O_3
q_M	1.0262	1.0516
$\frac{d^2E_M^{es}}{dq_M^2}$	-3.9239	-3.8291

Parameter fittings for iron oxides require four data points corresponding to four unknown parameters A, B, α, and β in pair potentials. The crystal data usually used are cohesive energy, equilibrium pressure, bulk modulus, and pressure derivative of bulk modulus. Of these four properties, cohesive energy is not usually available, but it can be calculated as follows. Suppose an oxide again takes the form M_xO_y. The chemical reaction for this oxidation can be described as:

$$xM + \frac{y}{2}O_2 \longrightarrow M_xO_y \tag{3.27}$$

The cohesive energy of M_xO_y $\left(E_c^{M_xO_y}\right)$ is the heat of formation of M_xO_y $\left(\Delta H_f^{M_xO_y}\right)$ subtracted by the cohesive energy of x mol of a metal M and y mol of oxygen O:

$$E_c^{M_xO_y} = \Delta H_f^{M_xO_y} - xE_c^M - yE_c^O \tag{3.28}$$

The value of E_c^M are readily available and the value of E_c^O is 2.58 eV [59]. Table 3.11 and 3.12 shows the results of parameter fitting. The fitting begins with considering only the first nearest neighbors in calculations. Once the starting values of the parameters are known, the calculations are extended to the neighbors distanced at 10 $\mathring{A}$ (a typical cut-off). The comparisons between the fitting and target results are shown in Tables 3.13 and 3.14. Each set of parameters has been tested with Moldy to see if the parameters yield a stable structure. A typical test is to run a pre-formed oxide with a corresponding set of the fitted parameters at 300 K for 10 ps. The structural stability can be observed from Moldy movie files and radial distribution curves.

Table 3.11 Pair potential parameters for iron oxides

Parameters	Fe-O in FeO	Fe-O in Fe_2O_3
A (eV)	1.813926	0.789382
B (eV)	2.992601	0.084102
α	14.30119	10.80134
β	6.574424	0.177024

Table 3.12 Fitted charges on iron ions

	Fe^{2+} in FeO	Fe^{3+} in Fe_2O_3
q_M	$+1.21e$	$+0.73e$

Table 3.13 The fitted and target values for the pair potential of FeO

Properties of FeO	Fitted Values	Target Values
Cohesive Energy (eV/atom)	-4.86	-4.86
Pressure (GPa)	-0.00146	0
Bulk modulus (GPa)	152.21	152.21
Pressure derivative of $\tilde{B}$	5.5	5.5

Table 3.14 The fitted and target values for the pair potential of Fe_2O_3

Properties of Fe_2O_3	Fitted Values	Target Values
Cohesive Energy (eV/atom)	-4.98	-4.98
Pressure (GPa)	-0.00006	0
Bulk modulus (GPa)	182.65	182.65
Pressure derivative of $\tilde{B}$	3.5	3.5

3.3 Modeling of Magnetite (Fe_3O_4)

Molecular dynamics simulations of magnetite have been done using pre-formed bulk structure and fixed charges on tetrahedral and octahedral iron ions [60]. One pair potential between iron and oxygen was used. The charges for tetrahedral and octahedral iron ions are fixed +2.5*e* and +3*e*, respectively. The fact is that magnetite (Fe_3O_4) is composed of two iron oxide compounds: wüstite (FeO) and hematite (Fe_2O_3). Therefore, to model magnetite formation in iron oxidation more correctly, two different pair potential functions corresponding to the two oxidation states of iron should be used. The steps in modeling magnetite formation are outlined here:

1. Find potentials for pure materials (iron and oxygen) and the iron-oxygen atomic pair.

2. Use the charge calculations from Chapter 2 to find ion charges at each time step.

3. Assign oxidation states (Fe^{2+} and Fe^{3+}) to iron ions so that the populations of Fe^{2+}:Fe^{3+} being 1:2 after all the charges in the system are known.

4. Apply the potentials corresponding to the oxidation states.

5. For interactions between iron atoms (with zero charge) and oxygen, pick one of the two pair potentials that gives the lowest energy.

After the ES energy minimization (see Chapter 2), each iron ion will be categorized as either Fe^{2+} or Fe^{3+}. This grouping process is quite simple, and it is only based on the charges that iron ions carry. The idea is to arrange all the iron ions in order of the charge magnitude from minimum to maximum. The cutoff charge magnitude will be determined to make the population of Fe^{2+}:Fe^{3+} be 1:2. The 1:2 population ratio corresponds to the actual chemical formula of magnetite $(FeO)(Fe_2O_3)$, which is equivalent to Fe_3O_4. Therefore, three groups of iron, neutral Fe (zero charge), Fe^{2+}, and Fe^{3+}, always exist in magnetite formation modeling.

As mentioned earlier, magnetite (Fe_3O_4) is composed of wüstite (FeO) and hematite (Fe_2O_3). After all iron ions have been branded with either Fe^{2+} or Fe^{3+}, two different sets of pair potentials for iron-oxygen pairs are used: one for the Fe^{2+}-O pair and another one for Fe^{3+}-O pair. Each set of potential parameters has been fitted to the corresponding crystal structures and properties of wüstite (FeO) and hematite (Fe_2O_3). For a pair of a neutral iron atom and oxygen (Fe-O pair), potential energy calculated from the pair potentials of the Fe^{2+}-O and Fe^{3+}-O pairs will be compared. The separation distance between a particular pair of an iron atom and an oxygen atom/ion differs from

one time step to another time step. So the pair potential that gives the lowest potential energy will be the choice for that Fe-O pair in that time step.

3.4 Benchmarking with Experiment

A simulation system to compare with the experiment consists of a semi-infinite slab of iron with oxygen on only one side. The slab of body-centered cubic iron is $57.33\,\mathring{A}$ angstrom thick. The temperature is kept constant using a Nose-Hoover heat bath. The system was run at 300 K and 423 K, corresponding to the actual temperatures in the experiment to be benchmarked [61]. The run time for each simulation is 40 picoseconds (ps) with a time step of 0.0002 ps for the total of 200,000 time steps.

Using the morphing scheme for oxygen, the results from this new oxygen potential approach are satisfactory. The oxygen gas diffuses out to nearby empty space as it should. The trajectories of iron and oxygen atoms/ions can be visualized using VMD. The root mean square displacement (RMSD) of several forefront oxygen ions in the slab have been calculated using the RMSD feature in VMD. As the name suggests, RSMD is the square root of mean square displacement (MSD) that is defined as:

$$\left\langle \left| r(t) - r(0) \right|^2 \right\rangle = \frac{1}{N} \sum_{i=1}^{N} \left| r_i(t) - r_i(0) \right|^2 \tag{3.29}$$

where N is the number of particles in a system, $r_i(t)$ is the distance of particle i from a reference point at time t. The distance squared is always positive no matter how a particle moves as moving forward and backward do not cancel the distance traveled. Both MSD and RMSD, analogous to variance and standard deviation, can be used to analyze the simulation results. By tracking the movements of each particle or a cluster of

particles or atoms against time, MSD and RSMD tell how active an atom or a cluster is during a simulation course. Figures 3.3 and 3.4 show forefront oxygen ions relatively settle by the end of each simulation. This means that the oxide layer growth relatively stops.

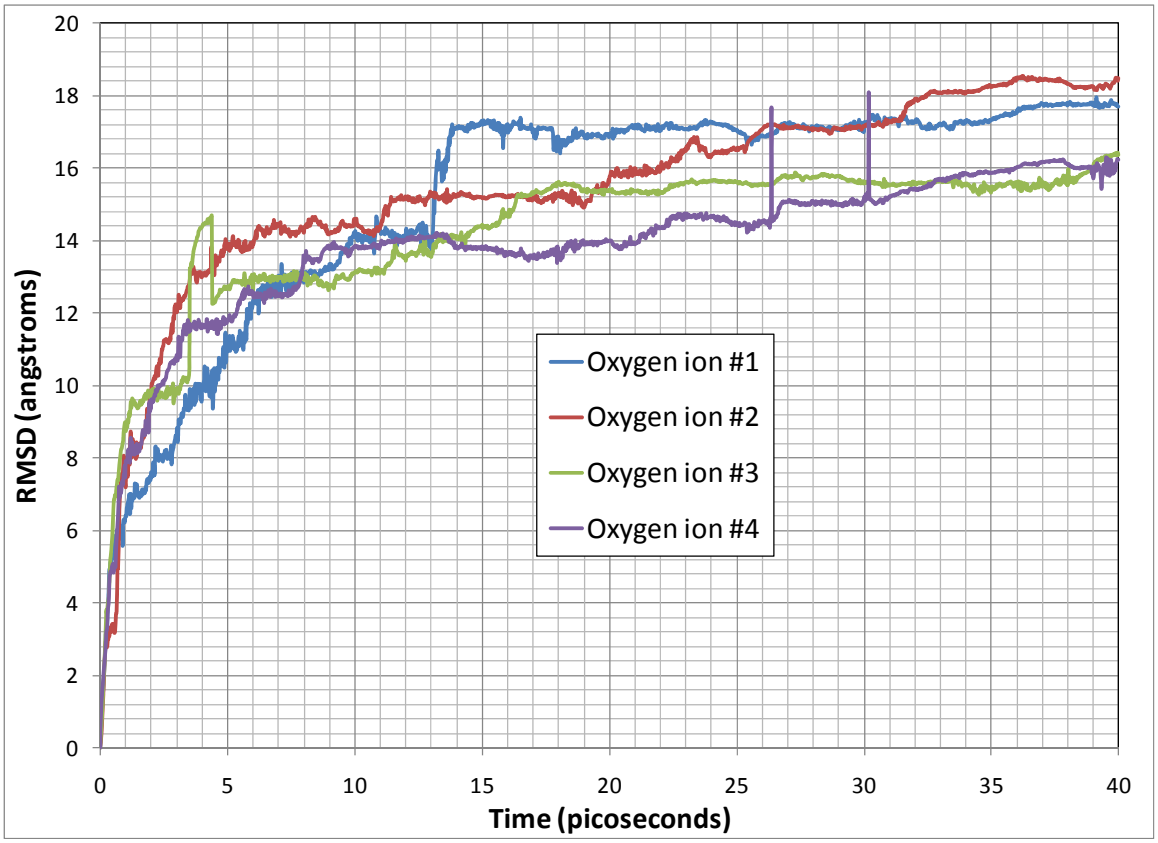

Figure 3.3 Root mean square distance of four forefront oxygen ions in the slab at 300 K

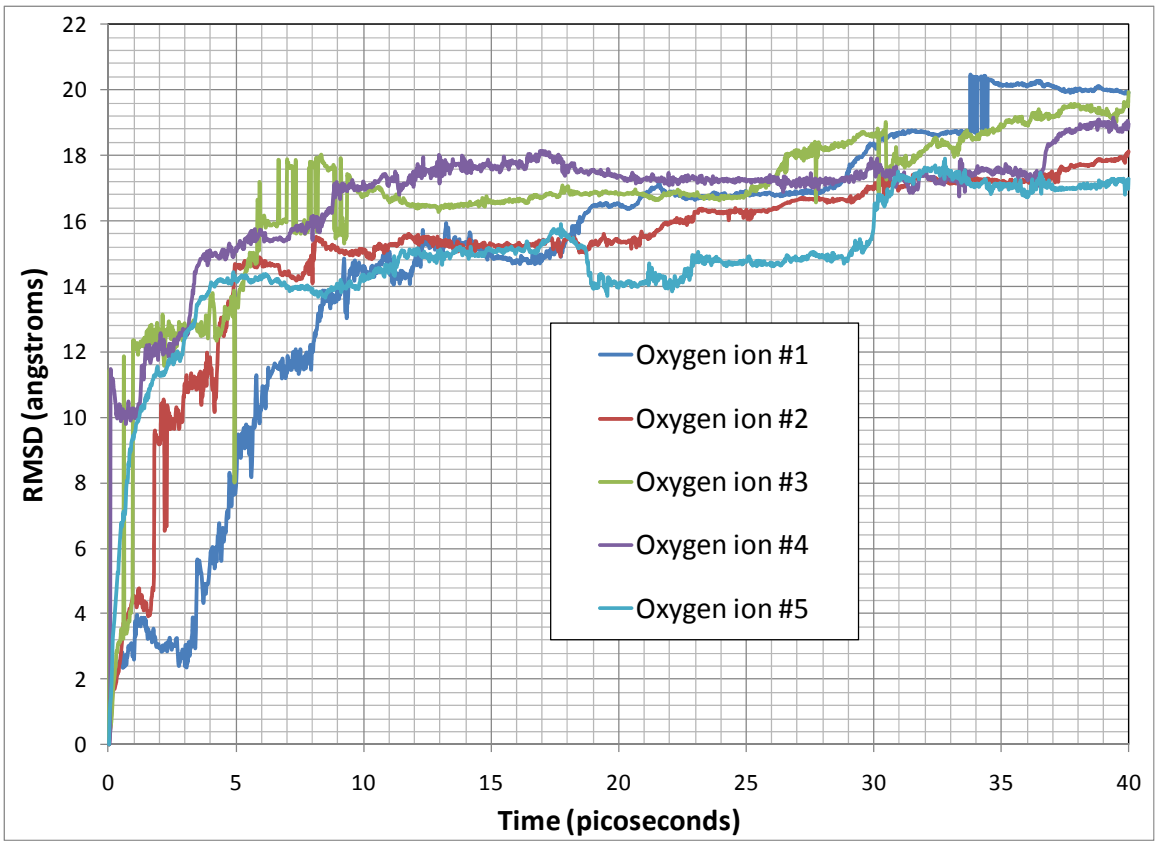

Figure 3.4 Root mean square distance of five forefront oxygen ions in the slab at 423 K

The oxide layer thicknesses from the simulations (see Figs. 3.5 and 3.6) are in the same order as the experimental results by Grosvenor et al. [61] as shown in Table 3.15. The oxide layer thicknesses are the distances from the slab surfaces to the points where the disorders of the iron lattices occur, which can be easily observed from the distribution histograms (Figs. 3.7 and 3.8). The sections between the two highlighted lines indicate the oxide layers. The iron ion populations are shown in Figs. 3.9 and 3.10. Note that the experiment results are from three different partial pressure environments, ranging from 0.013 Pa to 130 Pa (see Table 3.16). To complete the comparisons, the role of oxygen partial pressure is discussed in the next section.

Table 3.15 Comparison between the magnetite modeling and experiment results

	Present Calculation	Grosvenor et al. [61]
Oxide thickness at 300K	~2.3 nm	1.9 nm to 3.3 nm
Oxide thickness at 423K	~2.5 nm	3.1 nm to 5.1 nm

Table 3.16 The oxide thicknesses at various experiment conditions [61]

	0.013 Pa	1.3 Pa	130 Pa
300K	1.9 nm	2.9 nm	3.3 nm
423K	3.1 nm	4.0 nm	5.1 nm

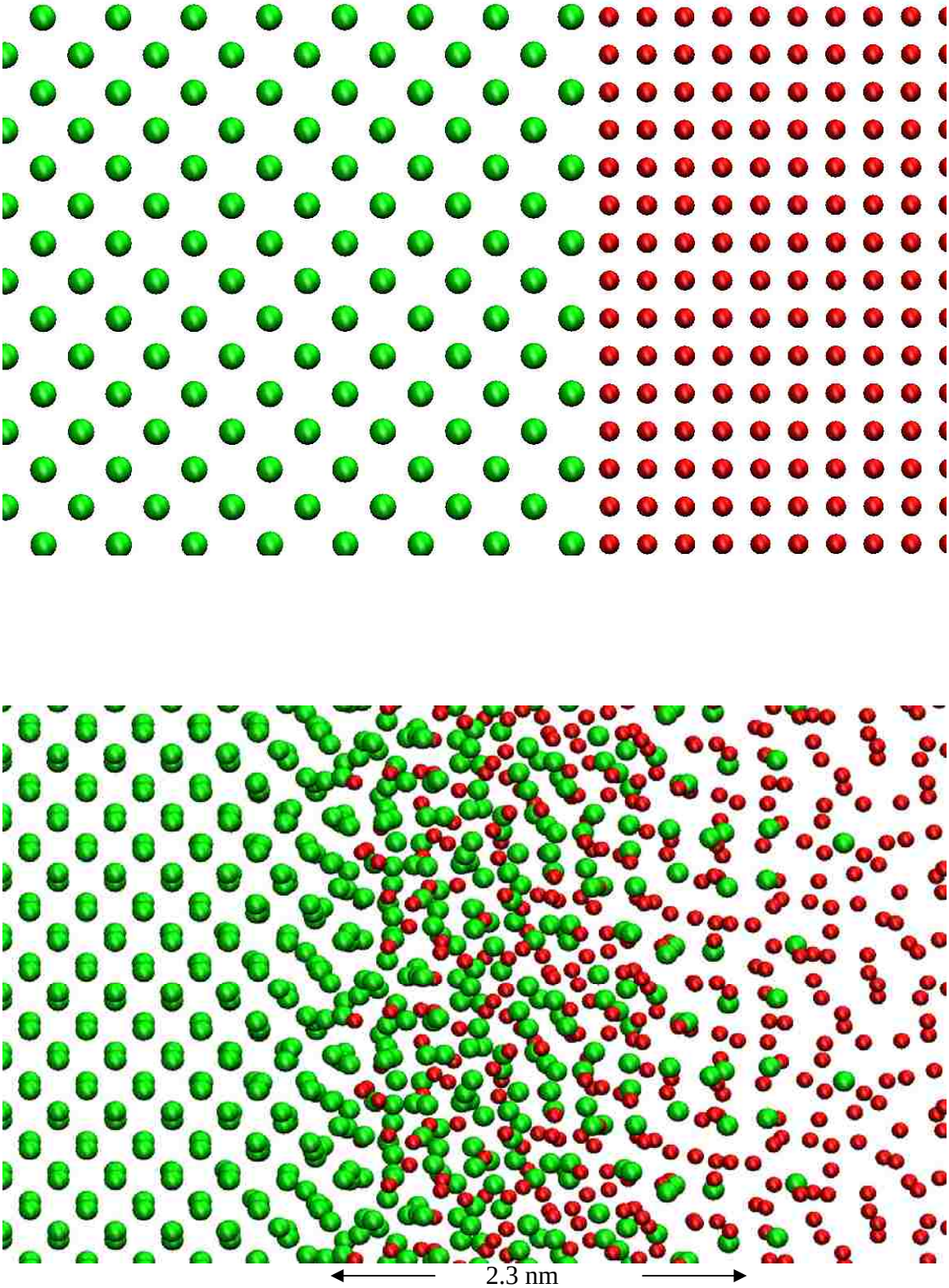

Figure 3.5 The x-z plane view of the iron slab (green) exposed to oxygen (red) at 300 K (top) At time $t = 0$ (bottom) At time $t = 20$ ps, the oxide thickness is about 2 nm.

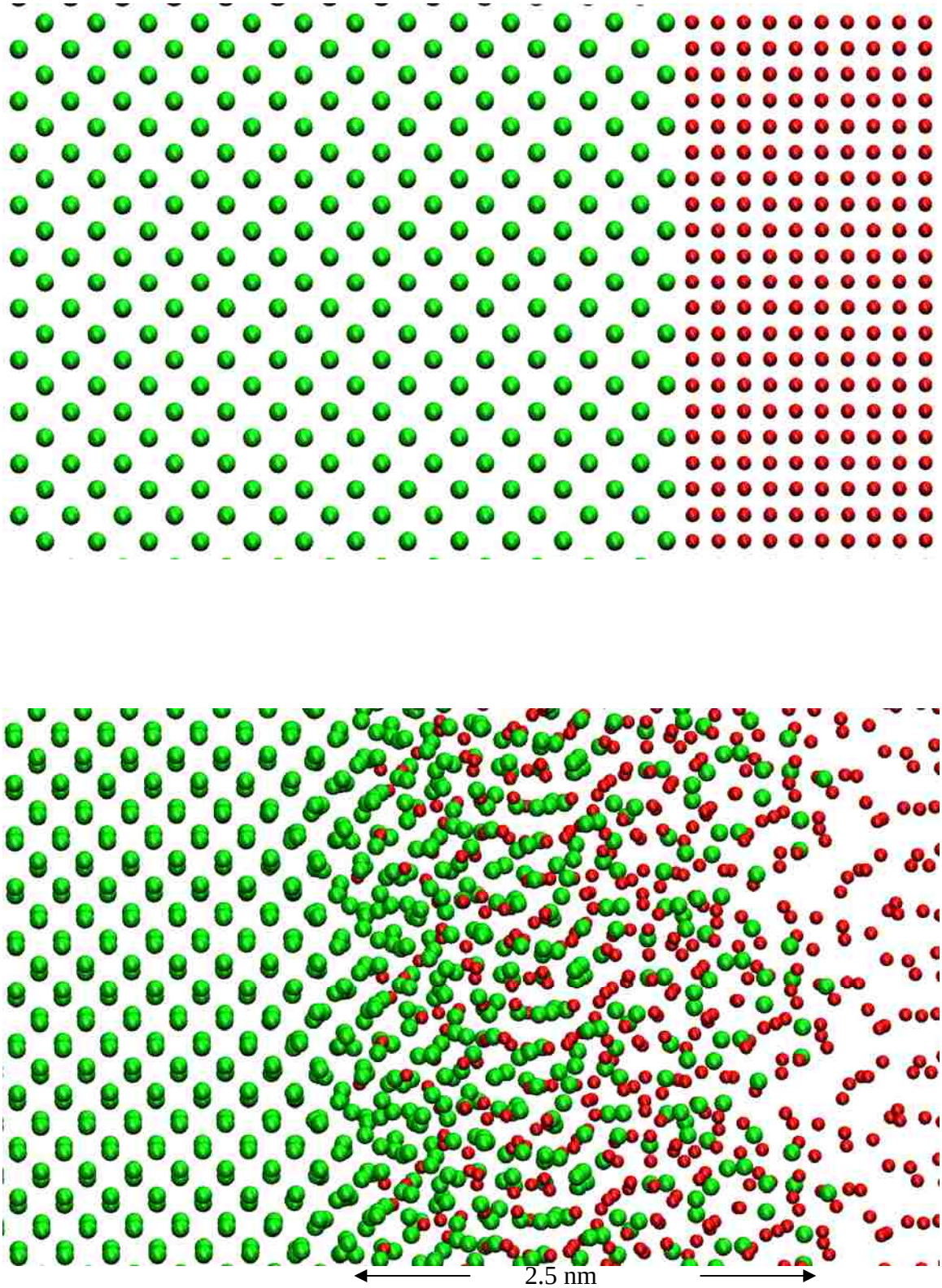

Figure 3.6 The x-z plane view of the iron slab (green) exposed to oxygen (red) at 423 K (top) At time $t = 0$ (bottom) At time $t = 20$ ps, the oxide thickness is about 2.6 nm.

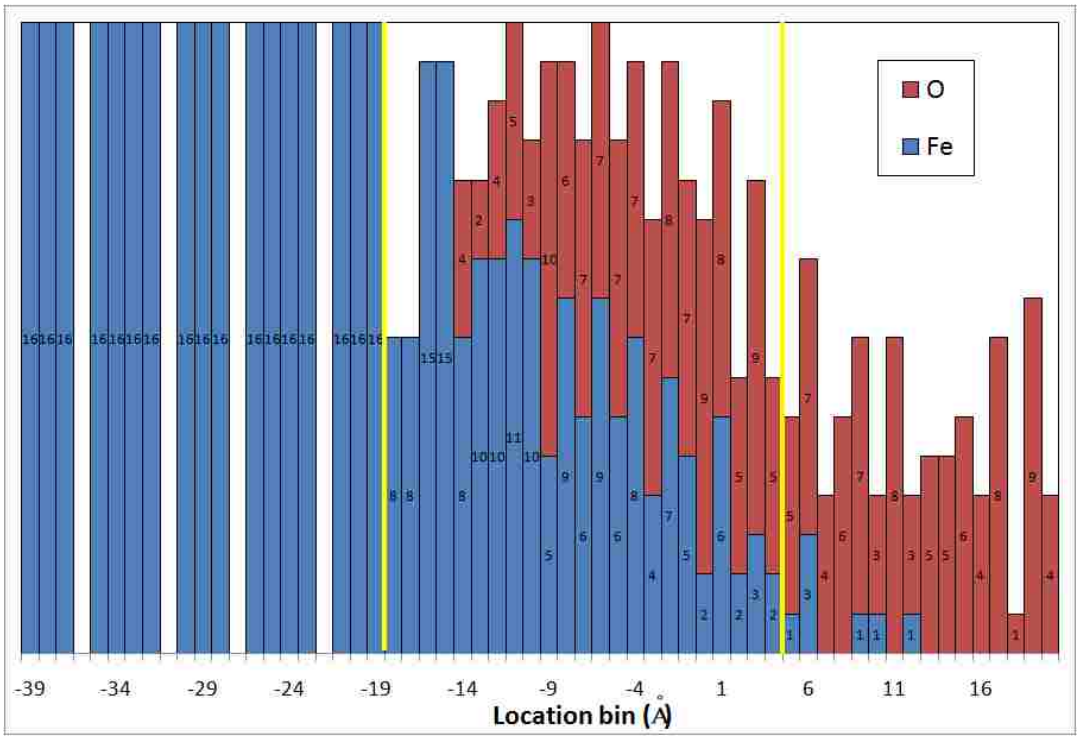

Figure 3.7 Histogram of iron and oxygen positions along the z direction at 300 K

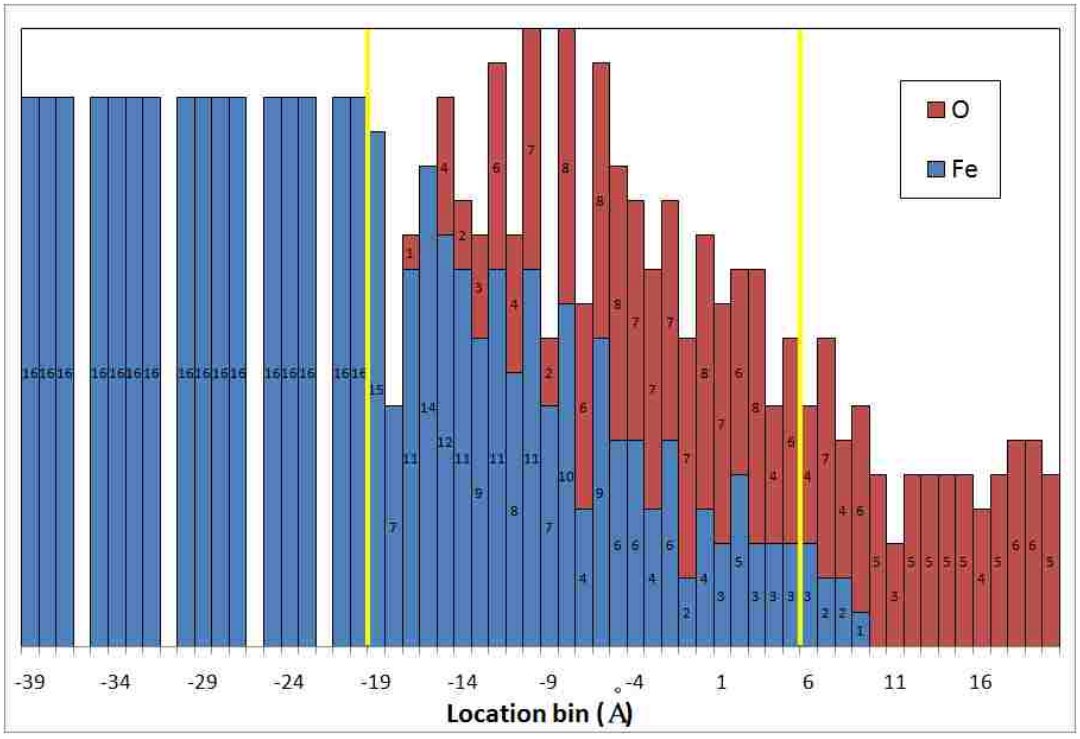

Figure 3.8 Histogram of iron and oxygen positions along the z direction at 423 K

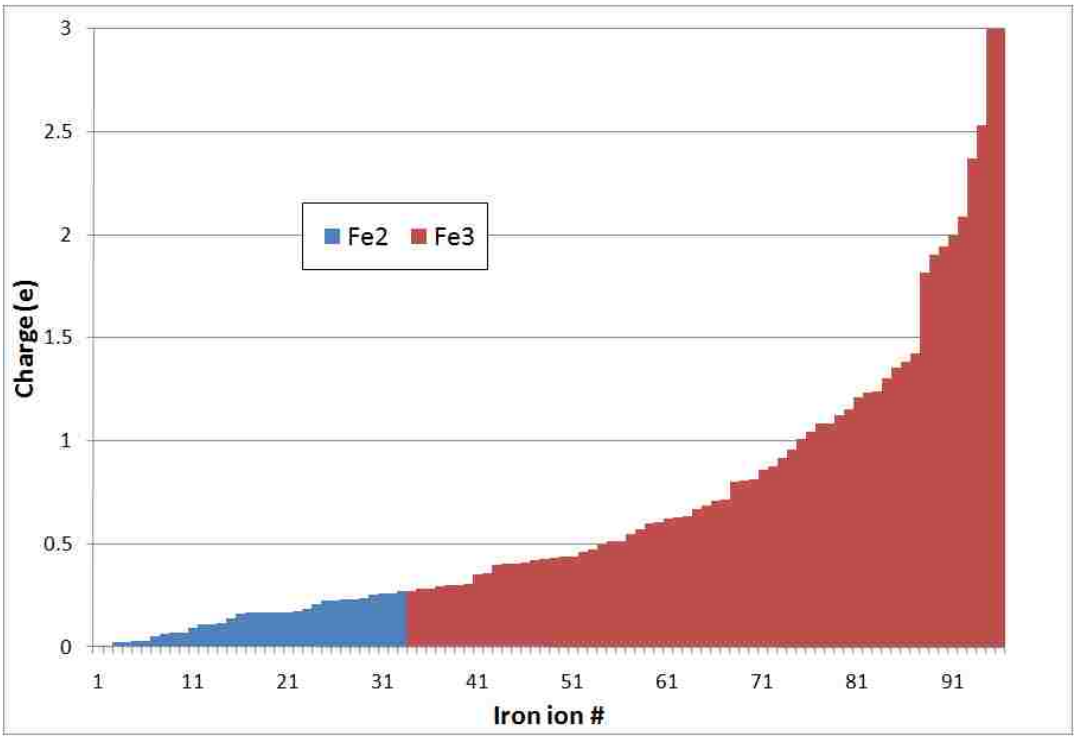

Figure 3.9 Population of Fe^{2+} and Fe^{3+} at the 1:2 ratio when T = 300 K

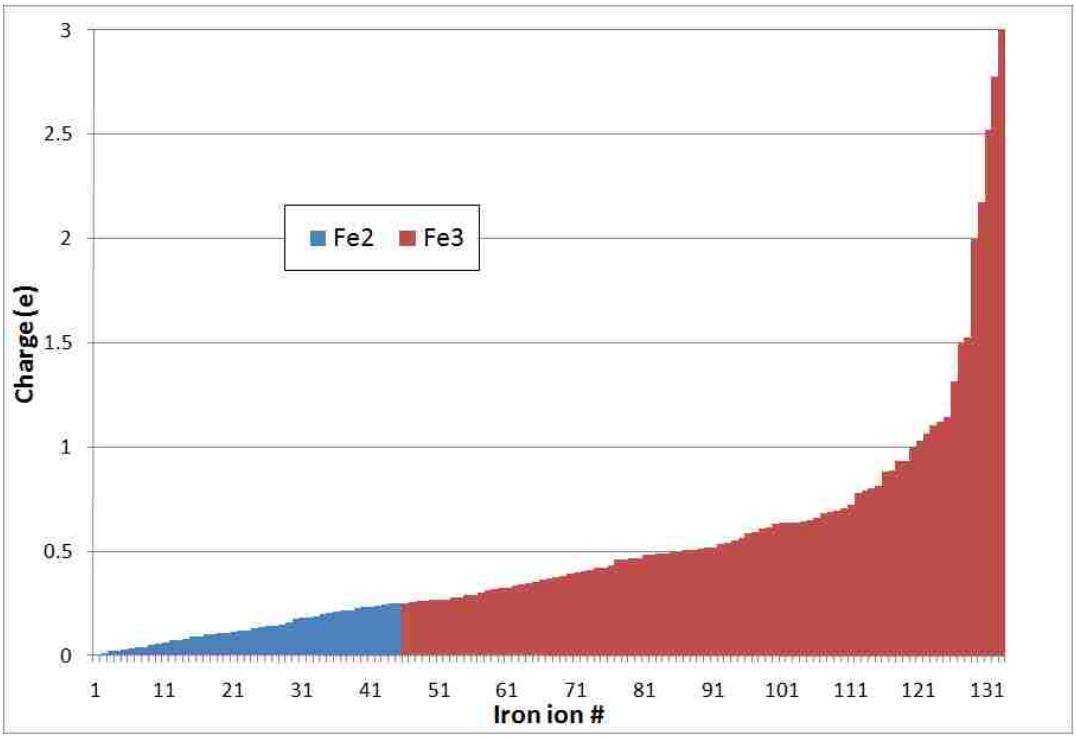

Figure 3.10 Population of Fe^{2+} and Fe^{3+} at the 1:2 ratio when T = 423 K

3.5 Role of Oxygen Partial Pressure

Oxidation studies often report amount of oxygen by partial pressure in atm or Pa. The results from the benchmarking experiment involve three different oxygen partial pressures: 0.013 Pa, 1.3 Pa, and 130 Pa. Ideally, to compare the results from the experiments and simulations, the conditions, which include temperature and pressure, have to be the same in both experiment and simulation studies. However, typical pressures in molecular dynamics simulations are in the order of MPa, not Pa. This is due to much smaller sizes of molecular dynamics systems, which are usually in the order of angstroms. To illustrate this problem of scale, assume that oxygen gas behaves like an ideal gas. So, n mol of oxygen at temperature T inside a volume V will have the pressure P equal to

$$P = nRT / V \tag{3.30}$$

where the gas constant R is 8.314472 J/mol–K. Using Eq. (3.30), the sizes of the cubic volumes for one oxygen molecule are listed in Table 3.17 below.

Table 3.17 The occupied cubic sizes of one O_2 at various experiment conditions

	0.013 Pa	1.3 Pa	130 Pa
300 K	6830.81 Å	1471.65 Å	317.06 Å
423 K	7659.7 Å	1650.23 Å	355.53 Å

As seen from Table 3.17, the cubic sizes of one oxygen molecule at the experiment conditions are very large compared to the cubic cell size of iron, which is 2.8665 Å.

Therefore, to include, say, 10 oxygen molecules, a system size will have to be in the order of microns, instead of angstroms - the typical molecular dynamics scale. In addition, a micron-sized system is impractical in terms of computational time and memory for a personal computer. Hence, the question remains: how will the pressure in the models be compared to the actual experiment?

Grosvenor et al. reported the experiment results with the inclusion of the direct logarithmic oxide thickness model [61]. They found that the experiment results are well fitted with the direct logarithmic oxide thickness model. The model describes an oxide layer thickness x as a function of time t as [62]:

$$\frac{dx}{dt} = A_0 e^{-\frac{E_0}{RT}} P^{0.6} e^{-\frac{\gamma_0 x}{RT}} \tag{3.31}$$

where A_0 is the pre-exponential value, E_0 is the activation energy, R is the gas constant, T is temperature, P is reaction pressure, γ_0 is increase in activation free energy with thickness of the oxide film. Using the initial condition that $x(t=0)=0$, the oxide layer thickness x is:

$$x = \frac{RT}{\gamma_0} \ln\left(\frac{\gamma_0 A_0}{RT} e^{-\frac{E_0}{RT}} P^{0.6} t + 1 \right) \tag{3.32}$$

Or,

$$x = \frac{1}{b_0} \ln\left(C_0 P^{0.6} t + 1 \right) \tag{3.32a}$$

where b_0 is defined as $\frac{\gamma_0}{RT}$ and C_0 is defined as $b_0 A_0 e^{-\frac{E_0}{RT}}$. The values of γ_0 and E_0 are listed in Table 3.18 [63]. Using the data provided by Grosvenor et al. [61, 63], A_0 is

calculated to be approximately 10^8 nm/Pa$^{0.6}$–s at 300 K and 10^7 nm/Pa$^{0.6}$–s at 423 K. Table 3.19 lists the values of b_0 and C_0 at 300 K and 423 K.

Figure 3.11 shows the plot of Eq. (3.32) when the pressures are at 1 MPa and 1 Pa and the temperatures are at 300 K and 423 K. The plot clearly indicates that the role of oxygen partial pressure is to either slow or hasten the initial oxide layer growth. During a transient period, an oxide layer grows faster at a higher oxygen partial pressure. However, once the oxide layer approaches its equilibrium growth, the effect of oxygen partial pressure diminishes. For clarity, Fig. 3.12 shows the ratio between the two oxide thicknesses at the same temperature but different pressures from Fig. 3.11. After the transient period, the oxide thickness at 1 MPa is only about 1.7 times the oxide thickness at 1 Pa, even though the pressure is one million times higher. Since the experiment shows that the oxide thicknesses range from 1.9 nm to 5.1 nm at pressures in the order of Pa, one would expect the oxide thicknesses to approximately range from 3.23 nm to 8.67 nm at pressures in the order of MPa. The simulation results with the pressures in the order of MPa yield the oxide thicknesses of about 2.3 nm and 2.5 nm at 300 K and 423 K, respectively, which are still in the same order of magnitude of the expected values.

Table 3.18 The values of γ_0 and E_0 for the reaction of Fe with O_2 [63]

Conditions	γ_0 (kJ/mol-nm)	E_0 (kJ/mol)
~1.3×10^{-2} Pa at 300 K	10 ± 1	32 ± 6
~1.3×10^{-2} Pa at 423 K	17 ± 1	32 ± 6

Table 3.19 The values of b_0 and C_0 at 300 K and 423 K

Temperatures	b_0 (1/nm)	C_0 (1/ $Pa^{0.6}$–s)
300 K	4.0	1075
423 K	4.8	4483

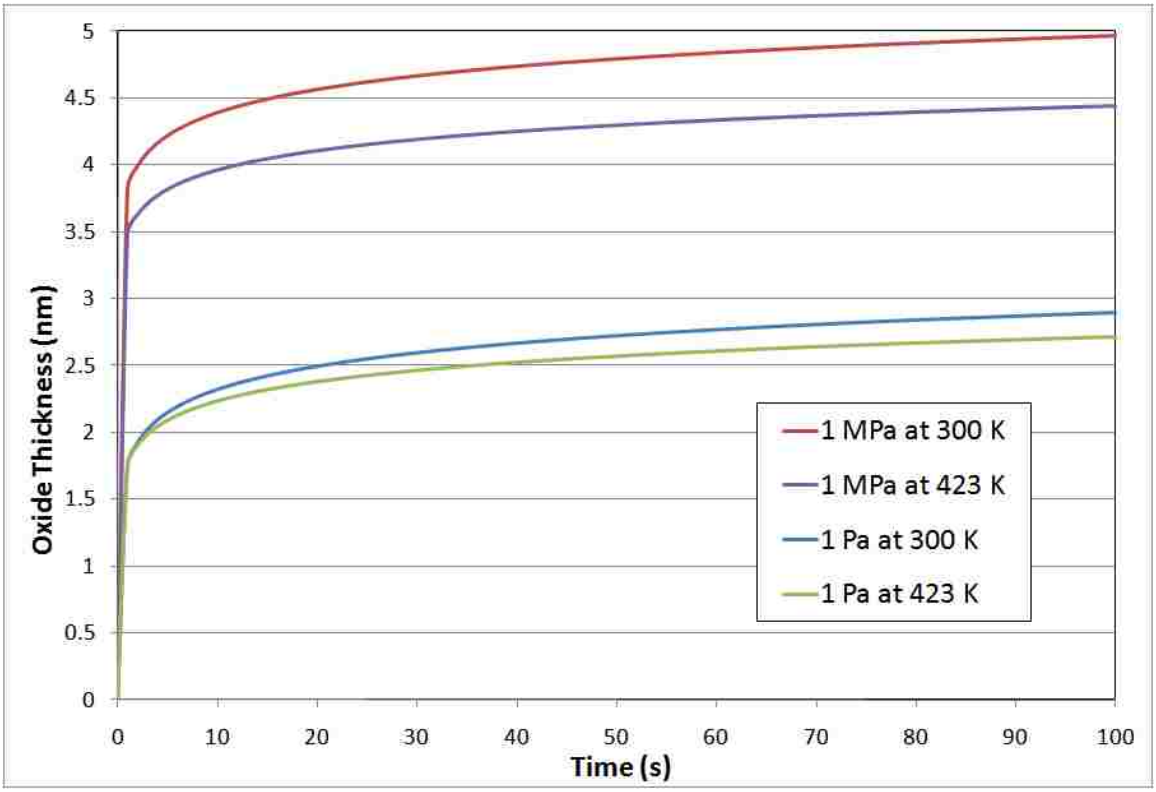

Figure 3.11 Oxide thicknesses according to the direct logarithmic oxide thickness model

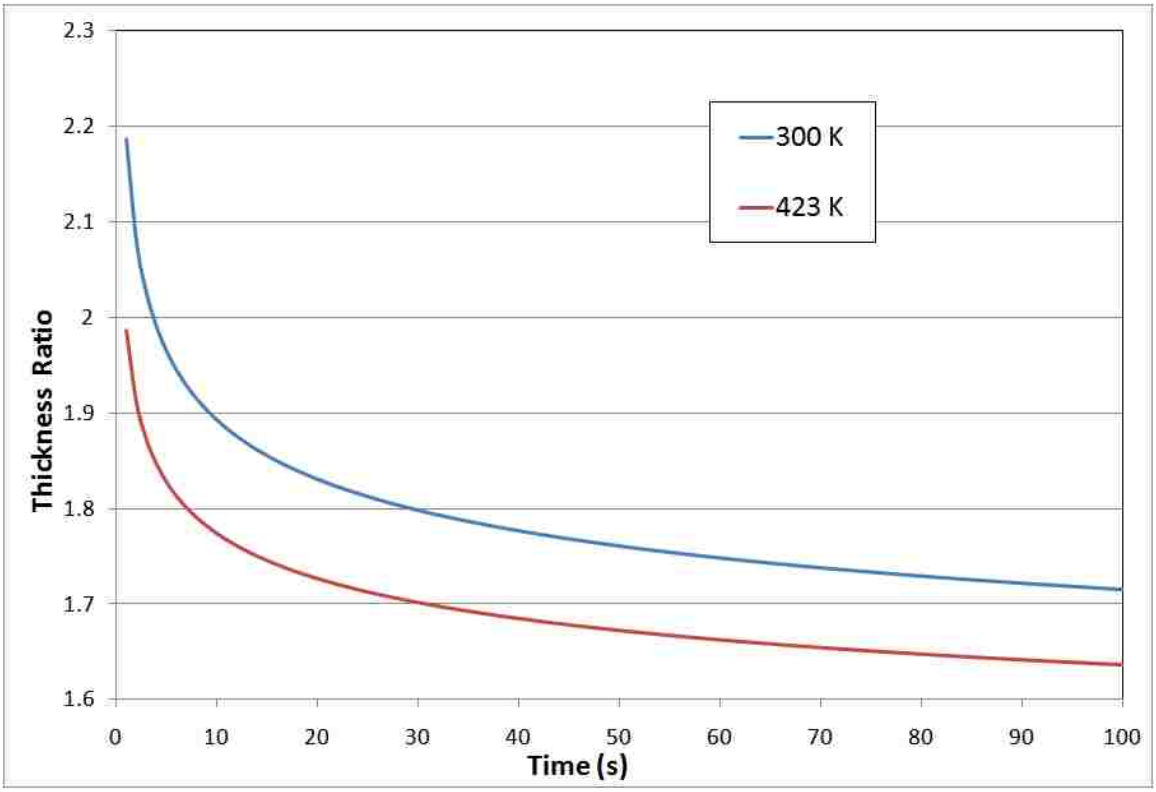

Figure 3.12 Oxide thickness ratios at 300 K and 423 K

3.6 Conclusion

This chapter presents a new approach in modeling oxidation of iron in the magnetite form. The approach is to use appropriate pair potentials based on charge distributions obtained from energy minimization. The simulation results agree with the experiment in terms of oxide layer thickness. Magnetite modeling provides a basis for modeling protective oxide layers that prevent lead diffusion into iron. The next chapter will present simulations of a mixture of lead, iron, and oxygen.

CHAPTER 4

MODELING IRON IN LIQUID LEAD UNDER OXYGEN CONTROL

4.1 Introduction

This chapter brings together the applications from the previous two chapters, namely charge optimization, metal oxidation modeling, and embedded atom method (EAM) potential. The simulated systems in this chapter are composed of solid iron, liquid lead, and oxygen at 550 $^{\circ}$C (823.15 K), a typical operating temperature for lead-cooled reactors. It is well known that liquid lead deteriorates structural steel because solid iron dissolves in liquid lead. Several methods to combat liquid lead corrosion problems have been mentioned in Chapter 1. One of those prevention methods relies on active oxygen control.

Several studies indicate that active oxygen control sustains oxide layers that protect against penetration of lead [64-66]. The formation of protective oxide layers is:

$$\frac{3}{4}Fe_{(s)} + \frac{1}{2}O_{2(g)} \longrightarrow \frac{1}{4}Fe_3O_{4(s)} \tag{4.1}$$

It has been experimentally proven that in a non-isothermal system, pre-oxidized steel cannot prevent lead corrosion attacks [64]. Unless self-healing of the protective oxide films takes place, Fe_3O_4-based oxide films will be disappearing according to the following reduction equation:

$$\frac{1}{4}Fe_3O_{4(s)} + Pb_{(l)} \longleftrightarrow \frac{3}{4}Fe_{(dissolved)} + PbO_{(dissolved)} \tag{4.2}$$

The above equation shows that protective oxide layers vanish when lead is oxidized, forming solid lead oxides (PbO) that can block the circulation flow of liquid lead. The two chemical reactions above are competing: one to repel oxide layers and one to repair

oxide layers. Therefore, an optimum operating condition should be such that the healing effect overcomes the damaging effect, and yet minimizes the formation of lead oxides in the system. This is when oxygen control comes into play. Too much oxygen in a system will excessively produce PbO. Too little oxygen in the system will deteriorate protective oxide layers.

An optimum oxygen level in the system will always fall between the two extremes: lower bound to sustain protective oxide layers and upper bound to deter lead oxide formations. Thermodynamics allows rough estimates on the upper and lower limits of oxygen in the system. The maximum oxygen level is simply the solubility limit of oxygen in liquid lead as mentioned in Chapter 1, which is given by:

$$\log C_O^{\max} = 3.2 - 5000/T \tag{1.1}$$

where $C_O^{\max}$ is the concentration of oxygen in wt % and T is the temperature in Kelvin. The minimum oxygen level will be the level that can sustain the protective oxide layers. Reference [1] reports the minimum oxygen level to be:

$$\log C_O^{\min} = -\frac{3}{4}\log C_{Fe} + 2.355 - 10600/T \tag{4.3}$$

where $C_O^{\min}$ is the concentration of oxygen in wt. %, C_{Fe} is the concentration of iron in wt. %, and T is the temperature in Kelvin. Equation 4.3 assumes that some iron atoms are already dissolved in liquid lead. For simplicity, let the existing dissolved iron concentration be 10^{-6} wt. %. So, Eq. 4.3 becomes:

$$\log C_O^{\min} = 6.855 - 10600/T \tag{4.3a}$$

Figure 4.1 shows the maximum and minimum oxygen levels for liquid lead coolant.

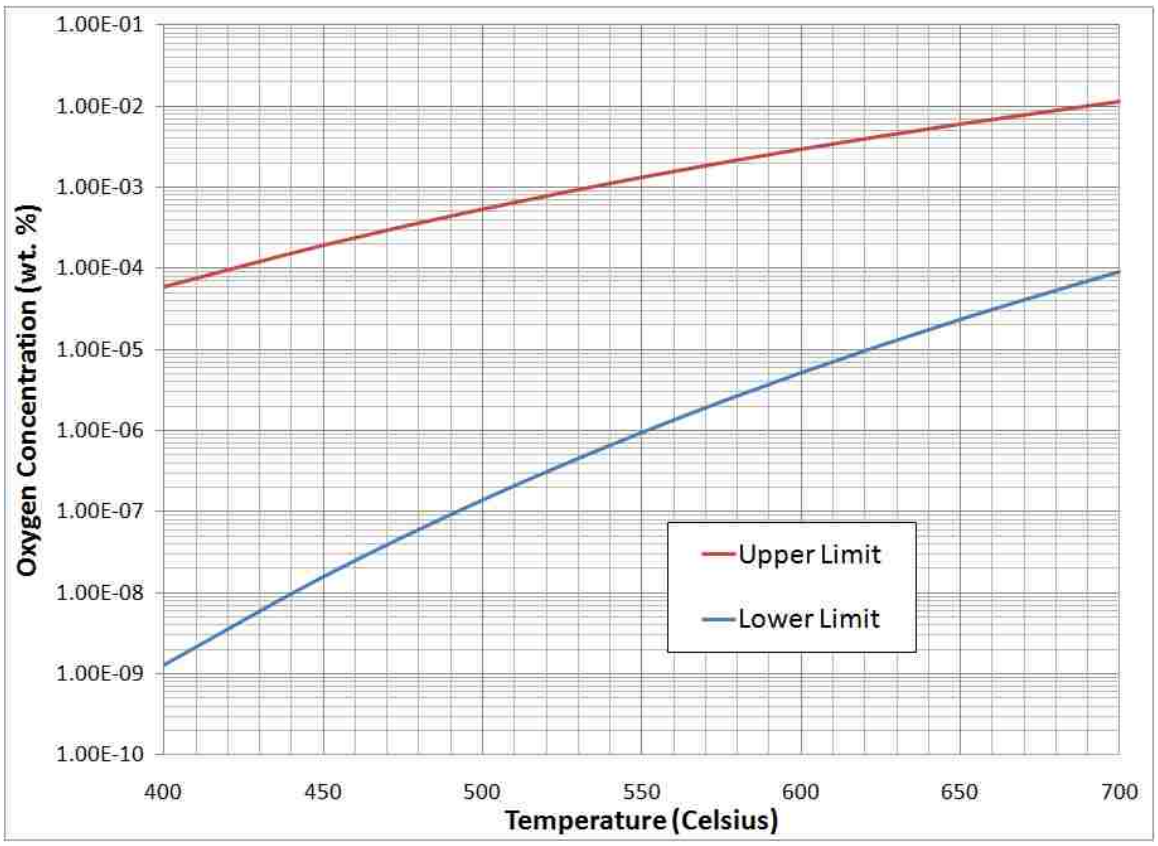

Figure 4.1 The lower and upper limits of oxygen concentration in liquid lead coolant

This chapter provides basis simulation studies of iron in liquid lead at various oxygen concentrations. The aims are to gain a basic understanding of system behaviors and see if the simulation results come out as expected. The next section explains the parameterization of the lead oxide (PbO) potential. After having all the necessary parameter values for the EAM potentials of lead and its oxide (PbO), several systems of iron in liquid lead with different oxygen concentrations will be studied. Finally, the simulation results are discussed, and conclusions are drawn.

4.2 Parameter Fittings for Lead and Lead Oxide (PbO)

Lead has a faced-centered-cubic (FCC) structure with the lattice parameter equal to 4.9508 $\mathring{A}$. The atomic properties of lead are listed in Table 4.1. Table 4.2 lists the fitted values of six pair potential and EAM parameters against the properties of lead. The fitting starts with the initial values of A, B, a, and b from Ref. [50]. Once the parameters for lead are obtained, the next step is to find parameters for a lead oxide that is stable at 550 $^{\circ}$C.

Lead oxides formed in lead and lead alloy coolants are found to be lead monoxides (PbO) [1]. The lead monoxides (PbO) exist in two forms as shown in Figs. 4.2 and 4.3: the red tetragonal α-PbO (litharge) and the yellow orthorhombic β-PbO (massicot). The stability of lead monoxides depends on operating temperatures. Litharge transforms into massicot at about 640 $^{\circ}$C (913.15 K). Since the temperature domain of interest in this dissertation is below 640 $^{\circ}$C, litharge is assumed to be the only form of lead oxides.

Litharge is in the spacegroup number 129 (P4/nmm) with the crystal parameters $a = 3.975\,\mathring{A}$ and $c = 5.023\,\mathring{A}$ [67]. The fractional coordinates of Pb and O in litharge is (0, 0.5, 0.2351) and (0, 0, 0), respectively. Table 4.3 lists the necessary values for parameterization of the Pb-O pair potential. Using the first nearest neighbors, the Pb-O pair potential parameter values are listed in Table 4.4 below. The fitted charge on lead ions is found to be $+0.5e$. Table 4.5 shows the parameter fitting results for the pair potential of PbO (litharge).

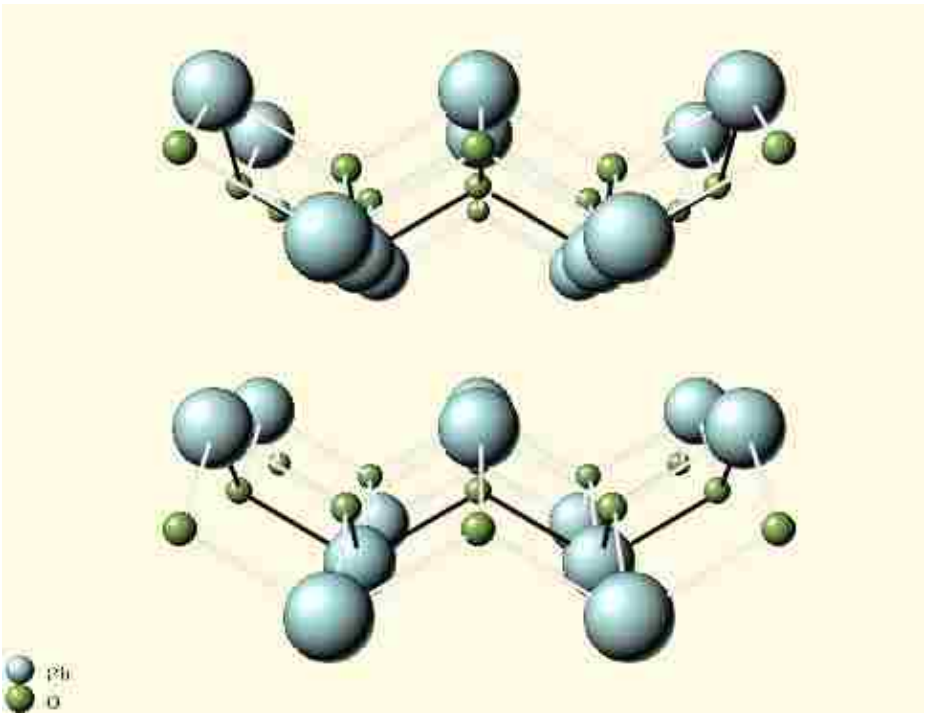

Figure 4.2 Crystal structure of litharge

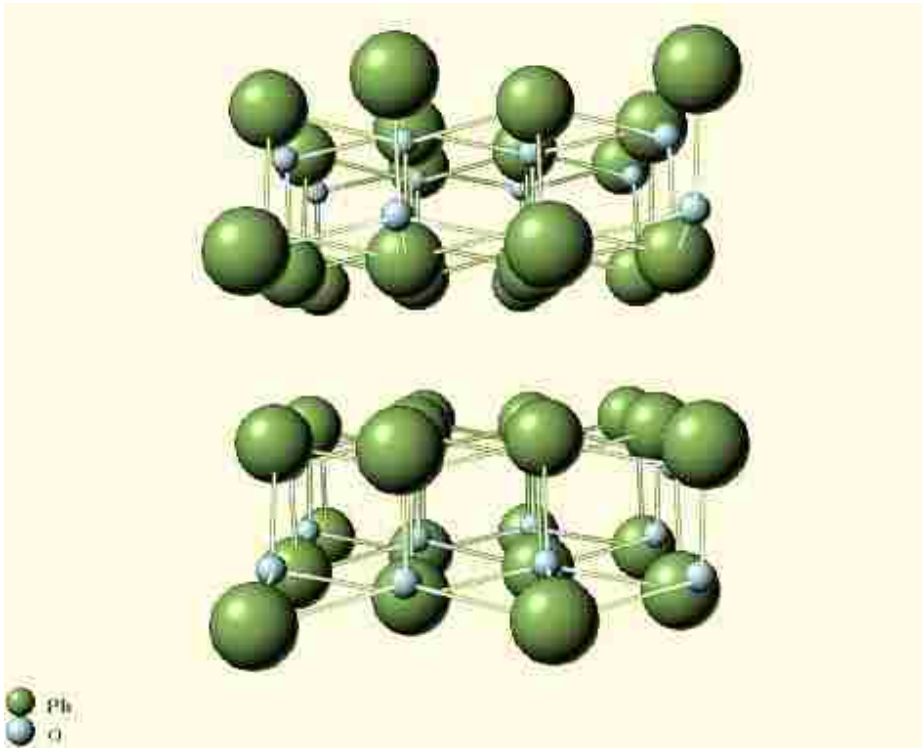

Figure 4.3 Crystal structure of massicot.

Table 4.1 Atomic properties of lead [57]

Ionization Energy IE (eV)	7.4167
Electron Affinity EA (eV)	0.3640
Electronegativity χ (eV)	3.8904
Self-coulomb Repulsion J (eV)	7.0527

Table 4.2 EAM parameter values of lead

Parameters of Lead	Value
A (eV)	0.14108114
B (eV)	0.210710421
α	8.62110911
β	4.806186728
f_e	0.65089
η	1.173139
F_0	-1.44638

Table 4.3 Values used in calculating equilibrium charges of lead ions

x	1
y	1
α_M	1.6543
r_e ($\mathring{A}$)	2.3115

Table 4.4 Pair potential parameter values for the Pb-O pair

Potential parameter	Pb-O
A (eV)	0.030194
B (eV)	2.524427
α	22.17366
β	0.009659

Table 4.5 The fitted and target values for the pair potential of PbO (litharge)

Properties of PbO	Fitted Values	Target Values
Cohesive Energy (eV/atom)	-3.42	-3.44
Pressure (GPa)	-0.32	0
Bulk modulus (GPa)	43.26	22.43 (Ref. [68])
Pressure derivative of $\widetilde{B}$	6.9	7.0 (Ref. [68])

4.3 Cross-Potential

Unlike the simulated systems in Chapters 3 and 4, the systems in this chapter consist of more than one metal. That is, each system contains iron and lead atoms, and that requires a cross pair potential between iron and lead. Johnson proposed the alloy EAM model to find a pair potential between two different metals [69]. Consider a binary alloy made of type-*a* and type-*b* atoms. Here, the alloy potential ϕ^{ab} has the form:

$$\phi^{ab} = \frac{1}{2}\left[\frac{f^{b}}{f^{a}}\phi^{aa} + \frac{f^{a}}{f^{b}}\phi^{bb} \right] \tag{4.4}$$

where ϕ^{aa} and ϕ^{bb} are the pair potentials of the type-*a* and type-*b* atoms, respectively, and f^{a} and f^{b} are the electron density functions of the type-*a* and type-*b* atoms, respectively. The derivation of the alloy potential begins with the transformations of the EAM function and pair potential. The derivation presented in this dissertation has minor differences from what Johnson did [69]. Under the transformations, the total energy must remain the same in order for the transformations to be invariant. Recall that the EAM energy F is a function of the total electron density ρ at a given atom site. The original derivation of the EAM function provides the following transformation of F into G [30]:

$$G(\rho) = F(\rho) + k\rho \tag{4.5}$$

where k is an arbitrary constant. Once the EAM transformation is known, the concurrent transformation to the pair potential can be derived. Recall Eq. (2.1), the energy E between a pair of atoms or particles separated by a distance r is

$$E = F(\rho) + \frac{1}{2}\phi(r) \tag{2.1}$$

If the EAM function $F(\rho)$ is transformed into $G(\rho)$, the pair potential $\phi(r)$ must also be inevitably converted into a new pair potential, say $\psi(r)$, in order to keep the same total energy. That is, under the transformations Eq. (2.1) becomes:

$$E = G(\rho) + \frac{1}{2}\psi(r) \tag{4.6}$$

Substituting Eq. (4.5) into the above equation gives:

$$E = F(\rho) + k\rho + \frac{1}{2}\psi(r) = F(\rho) + \frac{1}{2}\phi(r) \tag{4.7}$$

Therefore,

$$\psi(r) = \phi(r) - 2k\rho \tag{4.8}$$

Recall Eq. (2.4),

$$\rho = \sum_i f(r_i) \tag{2.4}$$

In the case of one pair of atoms, Eq. (2.4) reduces to $\rho = f(r)$, and Eq. (4.8) becomes:

$$\psi(r) = \phi(r) - 2kf(r) \tag{4.9}$$

The concurrent transformations as shown in Eqns. (4.5) and (4.9) will be required in deriving Eq. (4.4), the alloy potential.

A binary alloy of type-*a* and type-*b* atoms carries the total energy of:

$$E_t = \sum_i F^a(\rho_i) + \sum_i F^b(\rho_i) + \frac{1}{2}\left[\sum_{i,j\neq i}\phi^{aa}(r_{ij}) + \sum_{i,j\neq i}\phi^{ab}(r_{ij}) + \sum_{i,j\neq i}\phi^{bb}(r_{ij}) + \sum_{i,j\neq i}\phi^{ba}(r_{ij})\right] \tag{4.10}$$

The task here is to construct the cross-potential terms $\phi^{ab}(r)$ and $\phi^{ba}(r)$ from the monatomic potentials $\phi^{aa}(r)$ and $\phi^{bb}(r)$. Since $\phi^{ab}(r) = \phi^{ba}(r)$, the above equation can be rewritten as:

$$E_t = \sum_i F^a(\rho_i) + \sum_i F^b(\rho_i) + \frac{1}{2}\left[\sum_{i,j\neq i}\phi^{aa}(r_{ij}) + \sum_{i,j\neq i}\phi^{bb}(r_{ij})\right] + \sum_{i,j\neq i}\phi^{ab}(r_{ij}) \qquad (4.11)$$

Equations (4.5) and (4.9) give the following transformed potentials:

$$G^a(\rho) = F^a(\rho) + k^a\rho \qquad (4.12)$$

$$G^b(\rho) = F^b(\rho) + k^b\rho \qquad (4.13)$$

$$\psi^{aa}(r) = \phi^{aa}(r) - 2k^a f^a(r) \qquad (4.14)$$

$$\psi^{bb}(r) = \phi^{bb}(r) - 2k^b f^b(r) \qquad (4.15)$$

Equation (4.11) with the transformed potentials $(F \to G$ and $\phi \to \psi)$ becomes:

$$E_t = \sum_i G^a(\rho_i) + \sum_i G^b(\rho_i) + \frac{1}{2}\left[\sum_{i,j\neq i}\psi^{aa}(r_{ij}) + \sum_{i,j\neq i}\psi^{bb}(r_{ij})\right] + \sum_{i,j\neq i}\psi^{ab}(r_{ij}) \qquad (4.16)$$

Substituting Eqns. (4.11) to (4.15) into the above equation gives:

$$\begin{aligned} E_t = {} & \sum_i F^a(\rho_i) + k^a\sum_i \rho_i^a + \sum_i F^b(\rho_i) + k^b\sum_i \rho_i^b \\ & + \frac{1}{2}\sum_{i,j\neq i}\phi^{aa}(r_{ij}) - k^a\sum_{i,j\neq i} f^a(r_{ij}) \\ & + \frac{1}{2}\sum_{i,j\neq i}\phi^{bb}(r_{ij}) - k^b\sum_{i,j\neq i} f^b(r_{ij}) \\ & + \sum_{i,j\neq i}\psi^{ab}(r_{ij}) \end{aligned} \qquad (4.17)$$

For clarity in dealing with summations, assume that there are N^a and N^b atoms of the type-*a* and type-*b* atoms, respectively. The equation above can be expanded as:

$$
\begin{aligned}
E_t = & \sum_{i=1}^{N^a} F^a(\rho_i) + k^a \sum_{i=1}^{N^a} \left[\sum_{j=1, j\neq i}^{N^a} f^a(r_{ij}) + \sum_{j=1}^{N^b} f^b(r_{ij}) \right] \\
& + \sum_{i=1}^{N^b} F^b(\rho_i) + k^b \sum_{i=1}^{N^b} \left[\sum_{j=1}^{N^a} f^a(r_{ij}) + \sum_{j=1, j\neq i}^{N^b} f^b(r_{ij}) \right] \\
& + \frac{1}{2} \sum_{i=1}^{N^a} \sum_{j=1, j\neq i}^{N^a} \phi^{aa}(r_{ij}) - k^a \sum_{i=1}^{N^a} \sum_{j=1, j\neq i}^{N^a} f^a(r_{ij}) \\
& + \frac{1}{2} \sum_{i=1}^{N^b} \sum_{j=1, j\neq i}^{N^b} \phi^{bb}(r_{ij}) - k^b \sum_{i=1}^{N^b} \sum_{j=1, j\neq i}^{N^b} f^b(r_{ij}) \\
& + \sum_{i, j\neq i} \psi^{ab}(r_{ij})
\end{aligned}
\tag{4.18}
$$

With cancellations of the terms, the above equation becomes:

$$
\begin{aligned}
E_t = & \sum_{i=1}^{N^a} F^a(\rho_i) + k^a \sum_{i=1}^{N^a} \sum_{j=1}^{N^b} f^b(r_{ij}) + \sum_{i=1}^{N^b} F^b(\rho_i) + k^b \sum_{i=1}^{N^b} \sum_{j=1}^{N^a} f^a(r_{ij}) \\
& + \frac{1}{2} \sum_{i=1}^{N^a} \sum_{j=1, j\neq i}^{N^a} \phi^{aa}(r_{ij}) + \frac{1}{2} \sum_{i=1}^{N^b} \sum_{j=1, j\neq i}^{N^b} \phi^{bb}(r_{ij}) + \sum_{i, j\neq i} \psi^{ab}(r_{ij})
\end{aligned}
\tag{4.19}
$$

Or, in a reduced notation,

$$
\begin{aligned}
E_t = & \sum_{i} F^a(\rho_i) + \sum_{i} F^b(\rho_i) + \frac{1}{2} \sum_{i, j\neq i} \phi^{aa}(r_{ij}) + \frac{1}{2} \sum_{i, j\neq i} \phi^{bb}(r_{ij}) \\
& + \sum_{i, j\neq i} \psi^{ab}(r_{ij}) + k^a \sum_{i, j\neq i} f^b(r_{ij}) + k^b \sum_{i, j\neq i} f^a(r_{ij})
\end{aligned}
\tag{4.20}
$$

Comparing the above equation with Eq. (4.11) gives

$$
\psi^{ab}(r) = \phi^{ab}(r) - k^a f^b(r) - k^b f^a(r) \tag{4.21}
$$

The above equation also reduces to Eq. (4.9) as it should if $a = b$. Further assume that alloy potentials result from combinations of monatomic potentials. That is, there exist the functions $M^a(r)$ and $M^b(r)$ such that

$$
\phi^{ab}(r) = M^a(r)\phi^{aa}(r) + M^b(r)\phi^{bb}(r) \tag{4.22}
$$

$$
\psi^{ab}(r) = M^a(r)\psi^{aa}(r) + M^b(r)\psi^{bb}(r) \tag{4.23}
$$

Substituting the two equations above into Eq. (4.21) yields:

$$\begin{aligned} & M^a(r)\phi^{aa}(r) + M^b(r)\phi^{bb}(r) - k^a f^b(r) - k^b f^a(r) \\ & = M^a(r)\left[\phi^{aa}(r) - 2k^a f^a(r)\right] + M^b(r)\left[\phi^{bb}(r) - 2k^b f^b(r)\right] \end{aligned} \tag{4.24}$$

Further simplifications give:

$$2k^a f^a(r) M^a(r) + 2k^b f^b(r) M^b(r) = k^a f^b(r) + k^b f^a(r) \tag{4.25}$$

By inspection, the functions $M^a(r)$ and $M^b(r)$ must be

$$M^a(r) = \frac{1}{2}\frac{f^b(r)}{f^a(r)} \tag{4.26}$$

$$M^b(r) = \frac{1}{2}\frac{f^a(r)}{f^b(r)} \tag{4.27}$$

The two equations above give Eq. (4.4), the alloy potential.

4.4 Setting up Grain Boundaries

As mentioned in Chapter 1, one of the corrosion problems is due to crystal defects. Grain boundaries are the places where crystal defects, called dislocations, accumulate. At grain boundaries, each single crystal in a polycrystalline solid has slight disorientations with respect to its neighboring single crystals. Therefore, grain boundaries generally carry different densities and atomic configurations than those of the perfect single crystals. As a result, grain boundaries, acting like sinks, attract impurities and solutes, which normally segregate to interfaces. Consequently, grain boundaries offer easy paths for diffusion and cracking (along the grain boundaries).

This chapter compares the simulation results of iron crystals with and without grain boundaries at various oxygen concentrations. One way to create grain boundaries used in the simulations is to piece together two crystals with opposite rotations about the

same axis. The two-dimensional rotation matrix is used in finding new coordinates of crystals after rotations. The two-dimensional rotation matrix has the form:

$$\mathbf{R} = \begin{bmatrix} \cos\theta & \sin\theta \\ -\sin\theta & \cos\theta \end{bmatrix} \tag{4.28}$$

where θ is the angle of counter-clockwise rotation about the origin. For a vector $\vec{v}$ from the origin (0, 0) to a coordinate (x, y), the new vector $\vec{v}'$ after a rotation is:

$$\mathbf{R}\vec{v} = \begin{bmatrix} \cos\theta & \sin\theta \\ -\sin\theta & \cos\theta \end{bmatrix} \begin{bmatrix} x \\ y \end{bmatrix} = \begin{bmatrix} x\cos\theta + y\sin\theta \\ -x\sin\theta + y\cos\theta \end{bmatrix} = \vec{v}' \tag{4.29}$$

The new coordinate is $(x\cos\theta + y\sin\theta, -x\sin\theta + y\cos\theta)$.

4.5 Simulations of Iron in Liquid Lead at Various Oxygen Concentrations

This dissertation is intended to provide a basis for future simulation studies of iron in liquid lead under oxygen control. The six cases shown in Table 4.6 have been simulated at 550 °C (823.15 K). Oxygen is randomly distributed in liquid lead, and its concentrations in these cases represent three extreme limits: (1) zero oxygen, (2) oxygen at the maximum solubility limit (1.3×10^{-3} wt. %) in liquid lead at 550 °C (823.15 K), and (3) one-to-one atomic ratio between oxygen and lead. The iron slabs in the simulations are finite in the z-direction and infinite in the x-y plane. In the cases where iron crystals have grain boundaries, the tilt angle of all the grain boundaries is 30 degrees as shown in Fig. 4.4.

Table 4.6 The simulation cases of Fe in liquid Pb at various O_2 concentrations

	No Grain Boundary	With Grain Boundary
No Oxygen	•	•
Oxygen at Solubility Limit	•	•
Pb:O at 1:1 atomic ratio	•	•

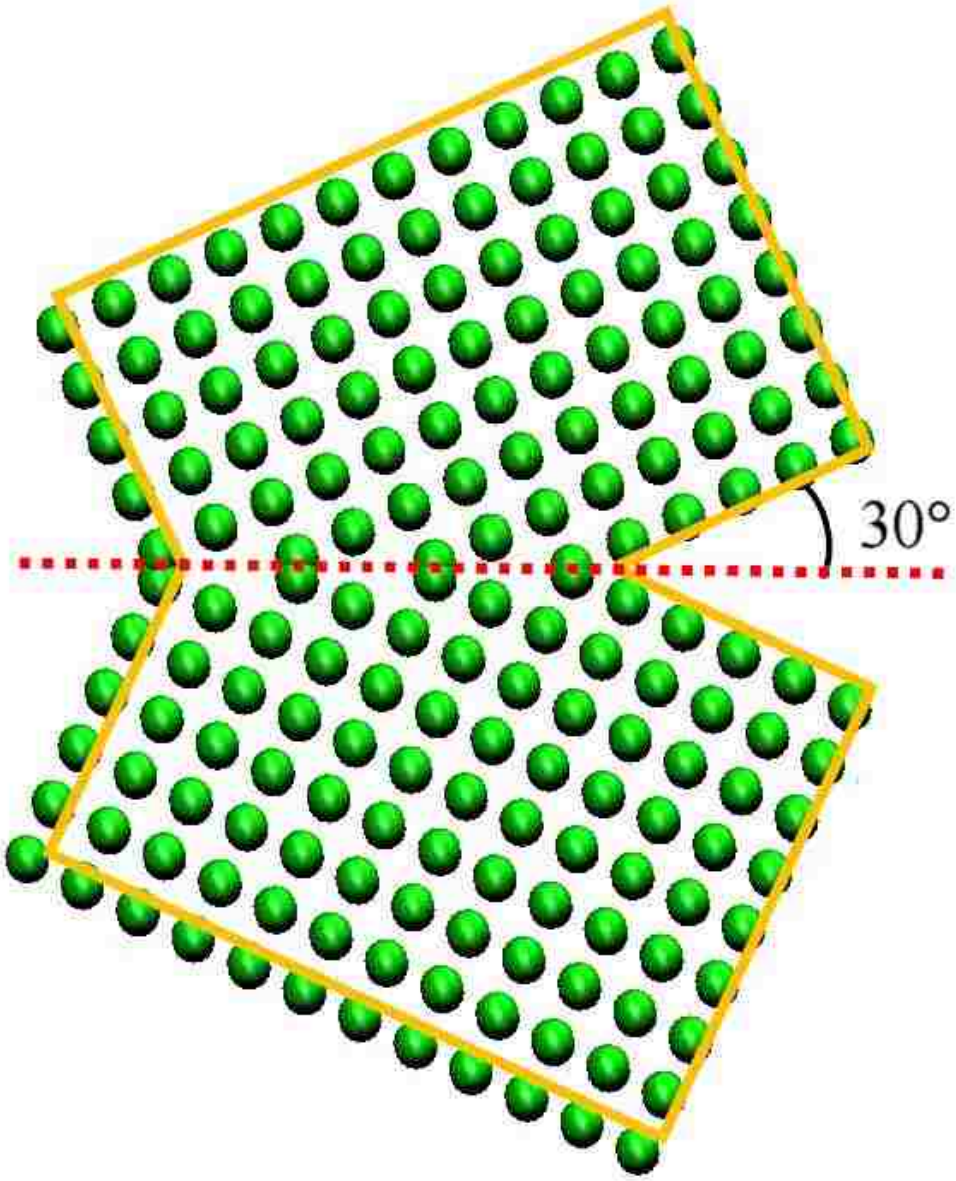

Figure 4.4 A simple schematic of two iron crystals with a grain boundary

4.5.1 Single Crystal of Iron in Liquid Lead without Oxygen

A semi-infinite single crystal of iron is put in liquid lead at 550 $^{\circ}$C. The iron crystal is $43.02\,\mathring{A}$ thick in the z direction and infinite in the x-y plane. The simulation run lasts 10 picoseconds (ps) in 20,000 time steps with the temperature control via a Nose-Hoover heat bath. Figures 4.5 and 4.6 show the system at the start and at the end of the simulation run, respectively. At the end of the 10-ps run, the thickness of the iron slab reduces from $43.02\,\mathring{A}$ to about $37.64\,\mathring{A}$. Liquid lead exerts pressure on both sides of the slab and, at the same time, iron atoms form a denser network to counter ingress of lead atoms. This results in the thickness reduction of the slab. A few iron atoms also begin to dissolve in liquid lead. At around 2.5 picoseconds in the simulation run, the mean squared displacement plot, especially in the z direction, clearly illustrates the sinusoid-like pattern as the system approaches equilibrium (Figs. 4.7 and 4.8). The radial distribution function of iron-lead atoms shows that the closest distance between a pair of iron and lead atoms is about $2.8\,\mathring{A}$ (see Fig. 4.9).

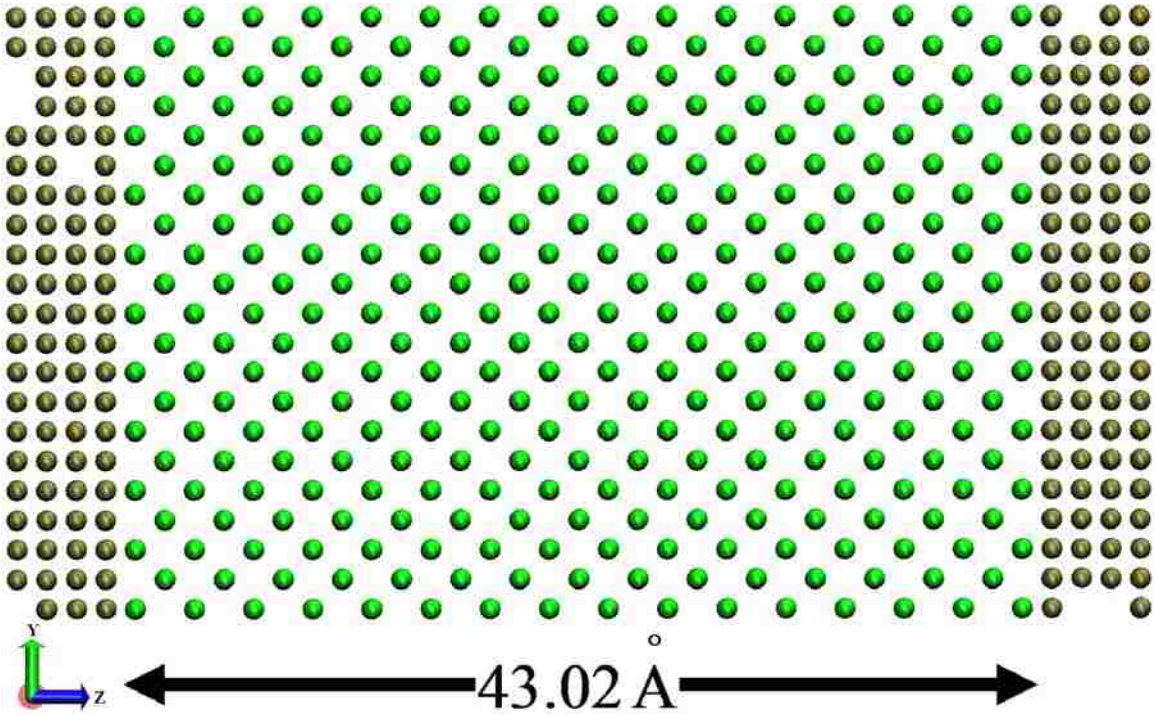

Figure 4.5 The initial setup of a single crystal of iron in liquid lead without oxygen. Iron and lead atoms are in green and ocher colors respectively.

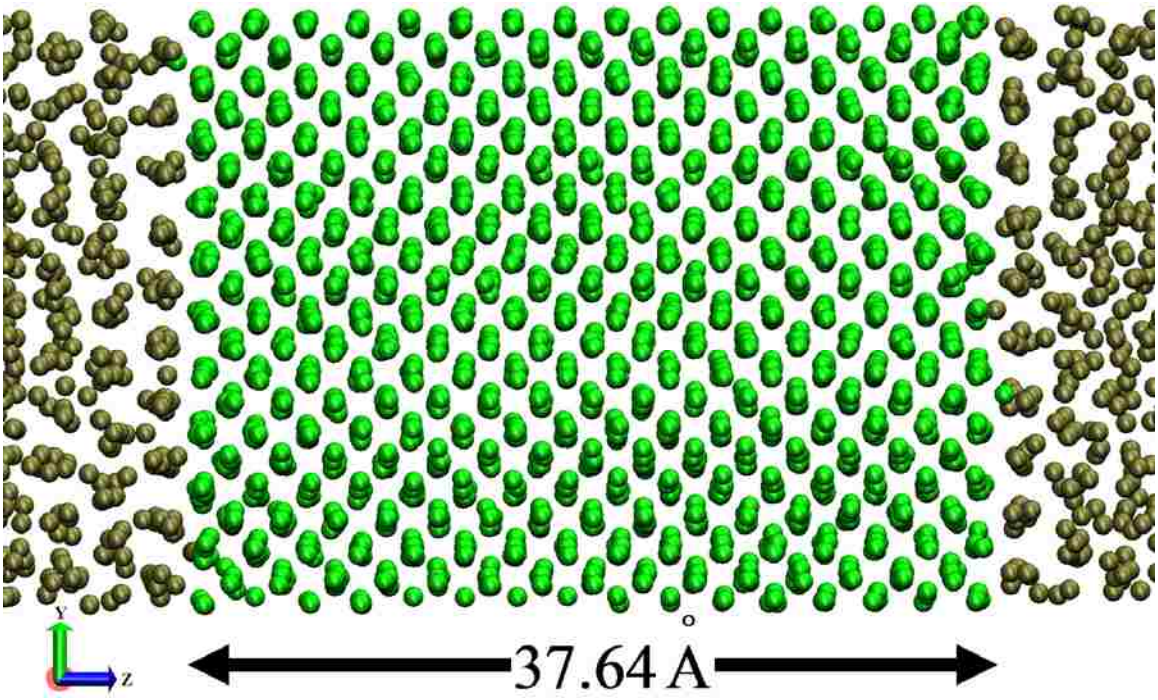

Figure 4.6 The single crystal of iron in liquid lead at the end of the 10-ps simulation run

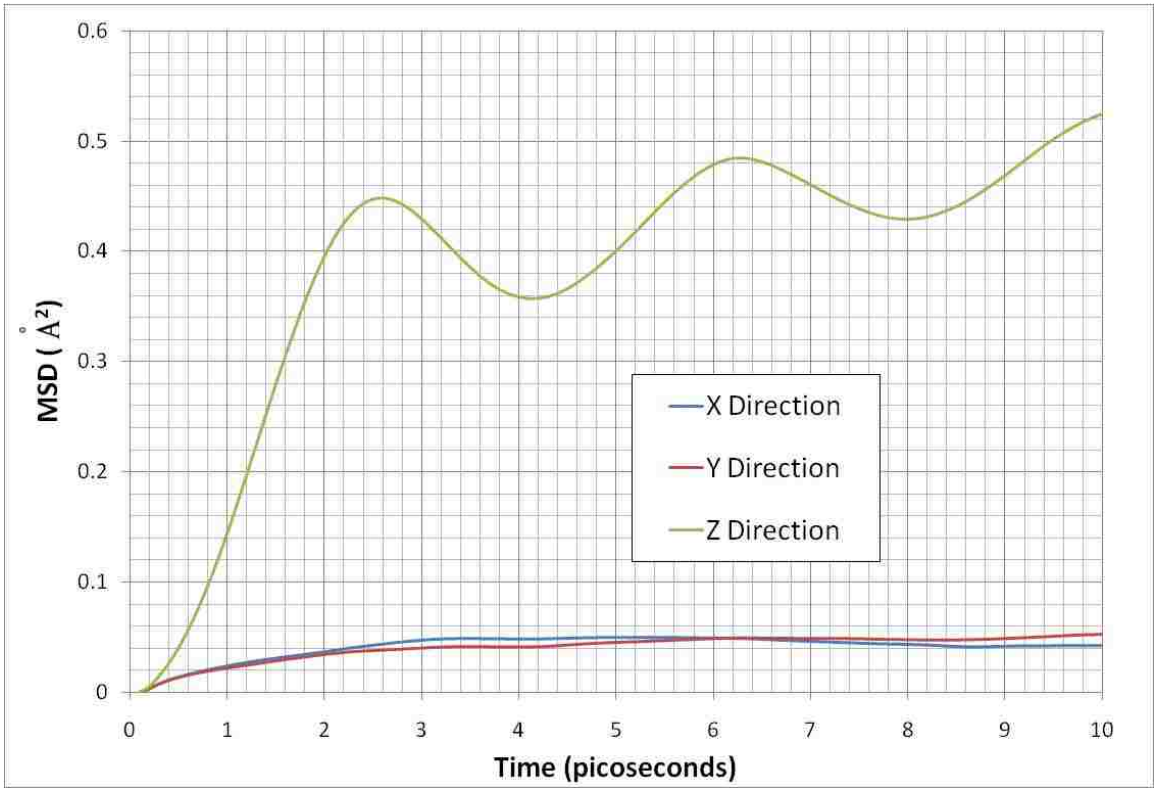

Figure 4.7 Mean square displacements of iron for the case of single iron crystal in liquid lead without oxygen

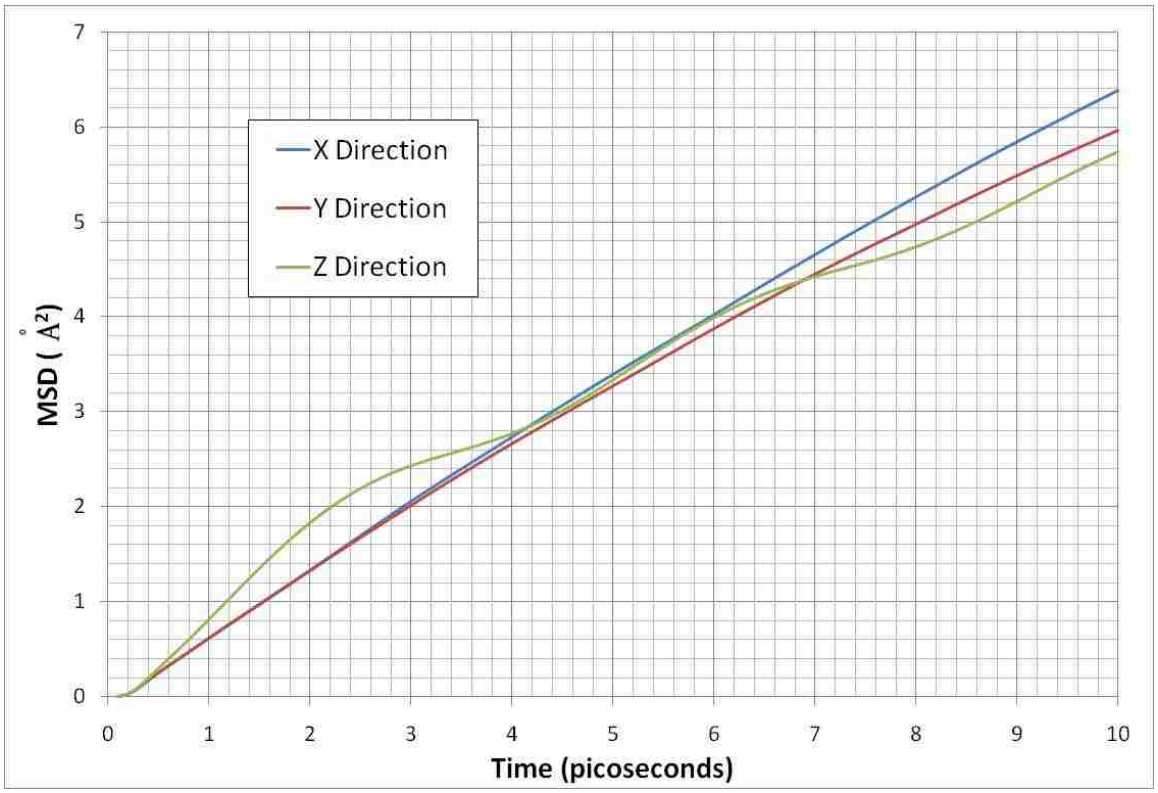

Figure 4.8 Mean square displacement of lead for the case of single iron crystal in liquid lead without oxygen

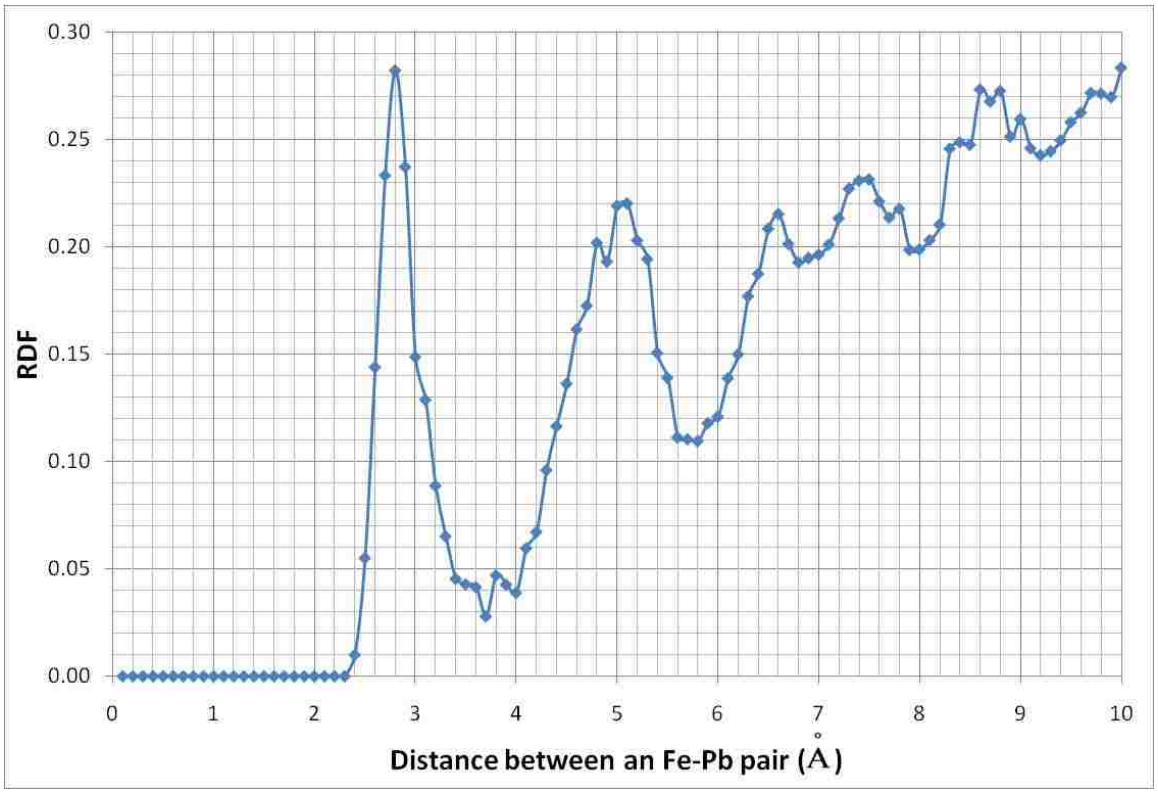

Figure 4.9 Fe-Pb radial distribution function for the case of single iron crystal in liquid lead without oxygen

4.5.2 Single Crystal of Iron in Liquid Lead with Oxygen at 1.3×10^{-3} wt. %

A semi-infinite single crystal of iron is put in liquid lead at 550 °C. Oxygen is randomly distributed in liquid lead at the ratio of one oxygen atom to sixty lead atoms, corresponding to 1.3×10^{-3} wt. %. The iron crystal is 43.02 Å thick in the z direction and infinite in the x-y plane. The simulation run lasts 10 picoseconds in 20,000 time steps. Figures 4.10 and 4.11 show the system at the start and at the end of the simulation run, respectively. The movements of iron atoms become somewhat limited by the present of oxygen, compared to the previous case that has no oxygen, as seen from the mean square displacement plot of iron (Fig. 4.12). The mean square displacement plots of lead and

oxygen (Figs. 4.13 and 4.14) show a typical result of mean square displacement for liquid.

At the end of the 10-ps run, the thickness reduces to about $37.64\,\text{Å}$, and virtually there is no penetration of lead atoms into the bulk of the slab. There is no formation of oxide films as there no excess oxygen to react with iron. The slab surfaces show protrusions of iron into liquid lead. More iron atoms also begin to dissolve in liquid lead. The radial distribution function (RDF) of iron and lead atoms (Fig. 4.15) shows the closest distance between a pair of iron and lead is about $2.8\,\text{Å}$, the same as in the previous case. The shape of the RDF curve is also similar to that of the previous case.

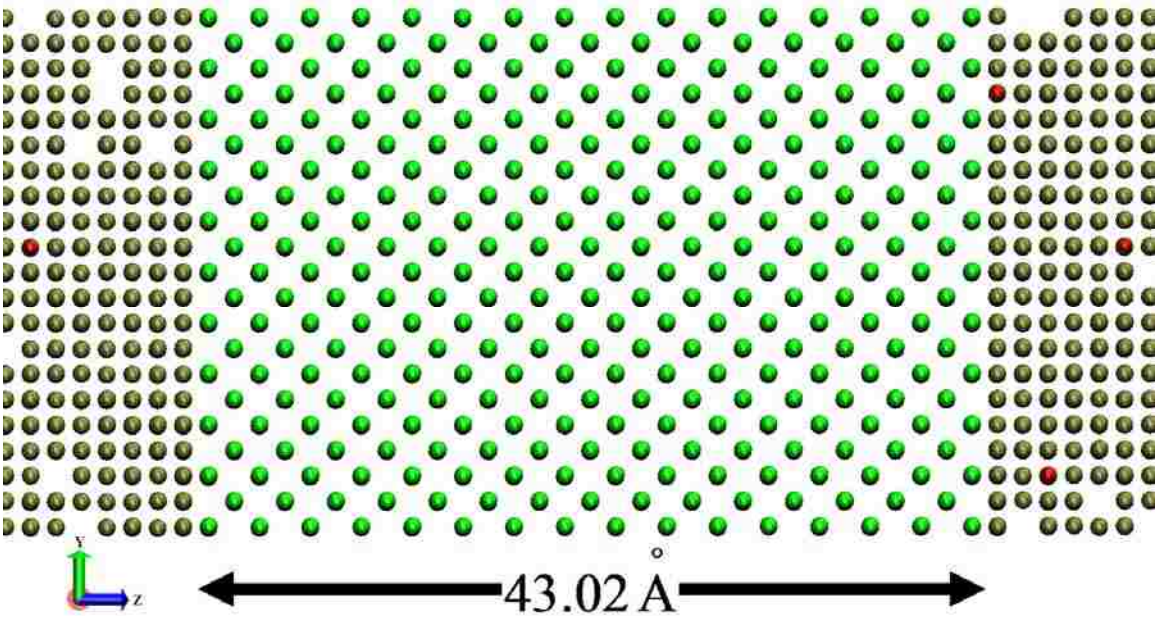

Figure 4.10 The initial setup of a single crystal of iron in liquid lead with dissolved oxygen at 1.3×10^{-3} wt. %. Oxygen is displayed in red color.

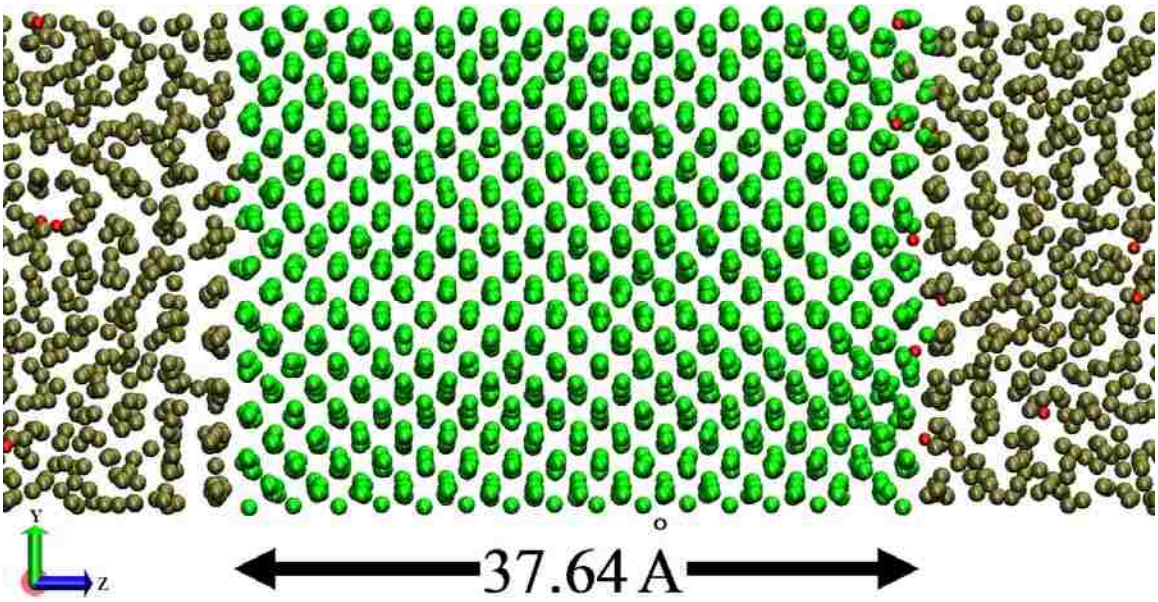

Figure 4.11 The end of the 10-ps simulation run of the single crystal of iron in liquid lead with dissolved oxygen at 1.3×10^{-3} wt. %

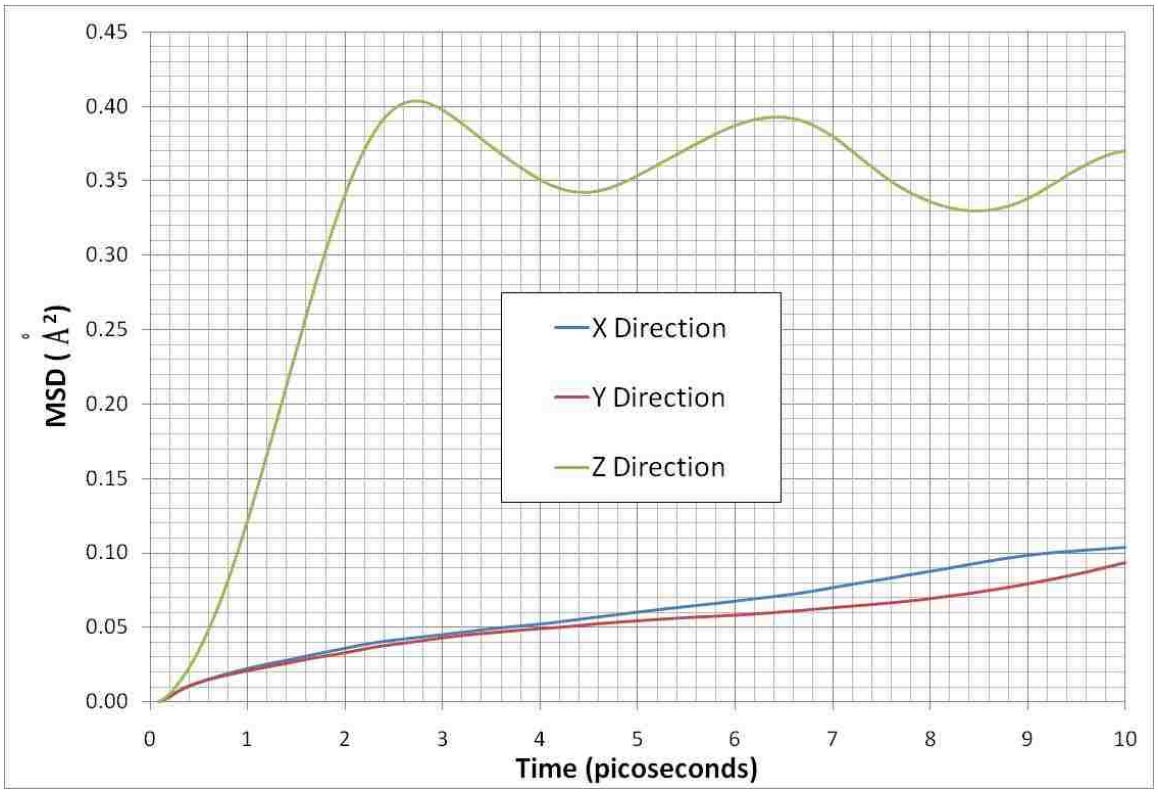

Figure 4.12 Mean square displacements of iron for the case of single iron crystal in liquid lead with dissolved oxygen at 1.3×10^{-3} wt. %

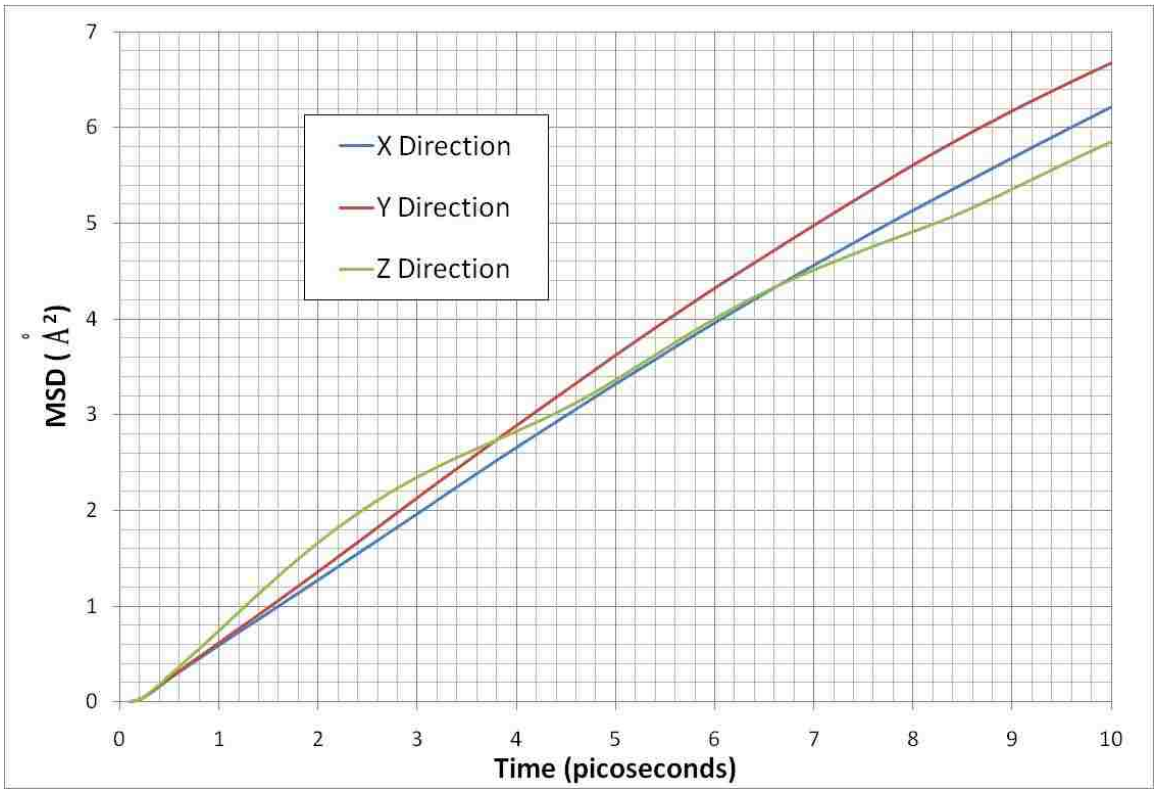

Figure 4.13 Mean square displacements of lead for the case of single iron crystal in liquid lead with dissolved oxygen at 1.3×10^{-3} wt. %

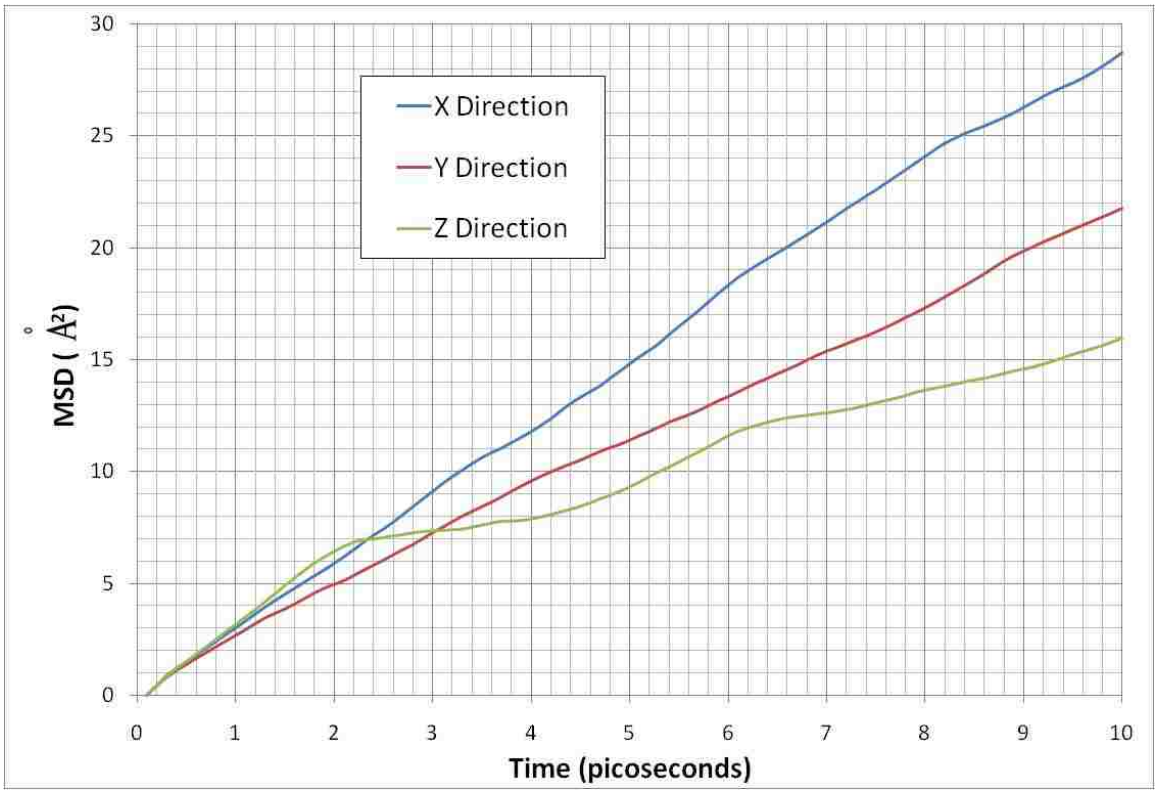

Figure 4.14 Mean square displacements of oxygen for the case of single iron crystal in liquid lead with dissolved oxygen at 1.3×10^{-3} wt. %

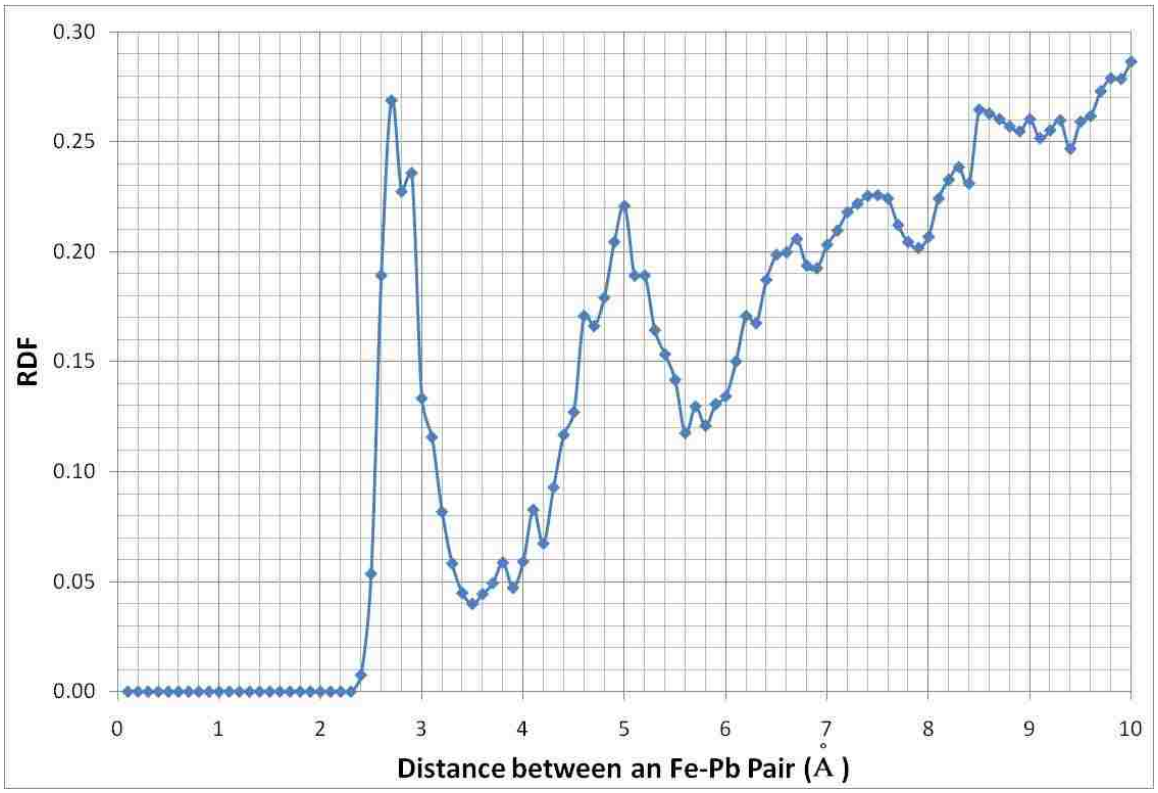

Figure 4.15 Fe-Pb radial distribution function for the case of single iron crystal in liquid lead with dissolved oxygen at 1.3×10^{-3} wt. %

4.5.3 Single Crystal of Iron in Liquid Lead with Oxygen at Pb:O = 1:1

A semi-infinite single crystal of iron is put in liquid lead at 550 °C. Oxygen is randomly distributed in liquid lead with one oxygen atom for every one lead atom, corresponding to the actual chemical formula of PbO. The iron crystal is 43.02 Å thick in the z direction and infinite in the x-y plane. The simulation run lasts 10 picoseconds in 50,000 time steps. Figures 4.16 and 4.17 show the system at the start and at the end of the simulation run, respectively.

At the end of the 10-ps run, the thickness of the slab reduces to about $40.51\,\text{Å}$. The iron slab is oxidized, forming $5.05\,\text{Å}$-thick oxide films on both sides of the slab. The mean square displacement of iron (Fig. 4.18) show that the system approaches equilibrium relatively faster than the previous two cases. The MSD plot of iron has no sinusoidal pattern. The MSD plots of lead and oxygen (Figs. 4.19 and 4.20) show a typical MSD result for liquid. However, the movement of lead atoms is somewhat limited as seen from a decrease in its MSD magnitude. The RDF plot (Fig. 4.21) shows that the closest distance between iron and lead atoms remains $2.8\,\text{Å}$.

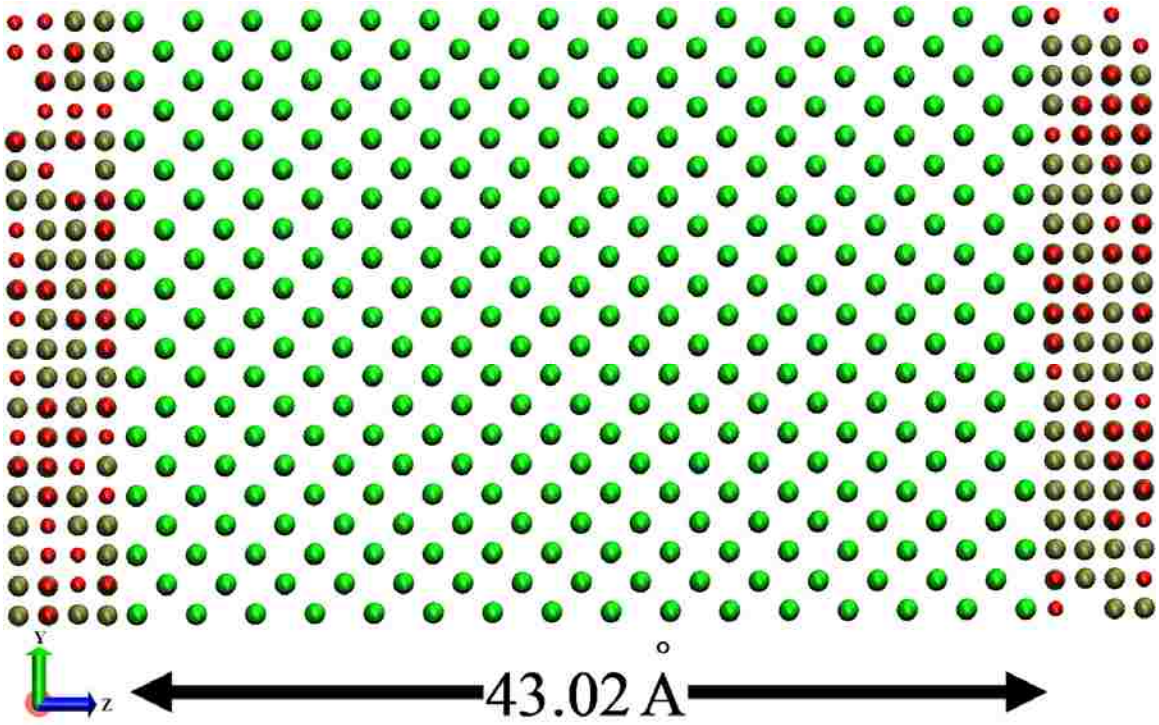

Figure 4.16 The initial setup of an single crystal of iron in liquid lead with the Pb:O atomic ratio at 1:1

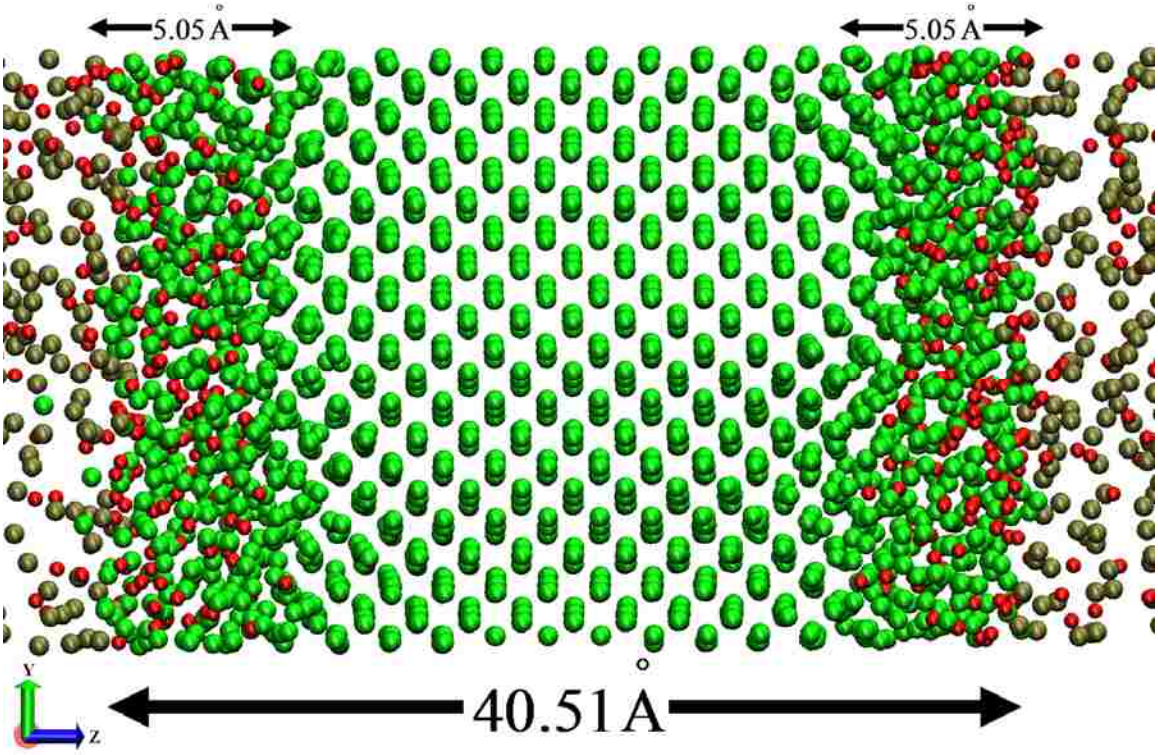

Figure 4.17 The end of the 10-ps simulation run of the single crystal of iron in liquid lead with the Pb:O atomic ratio at 1:1

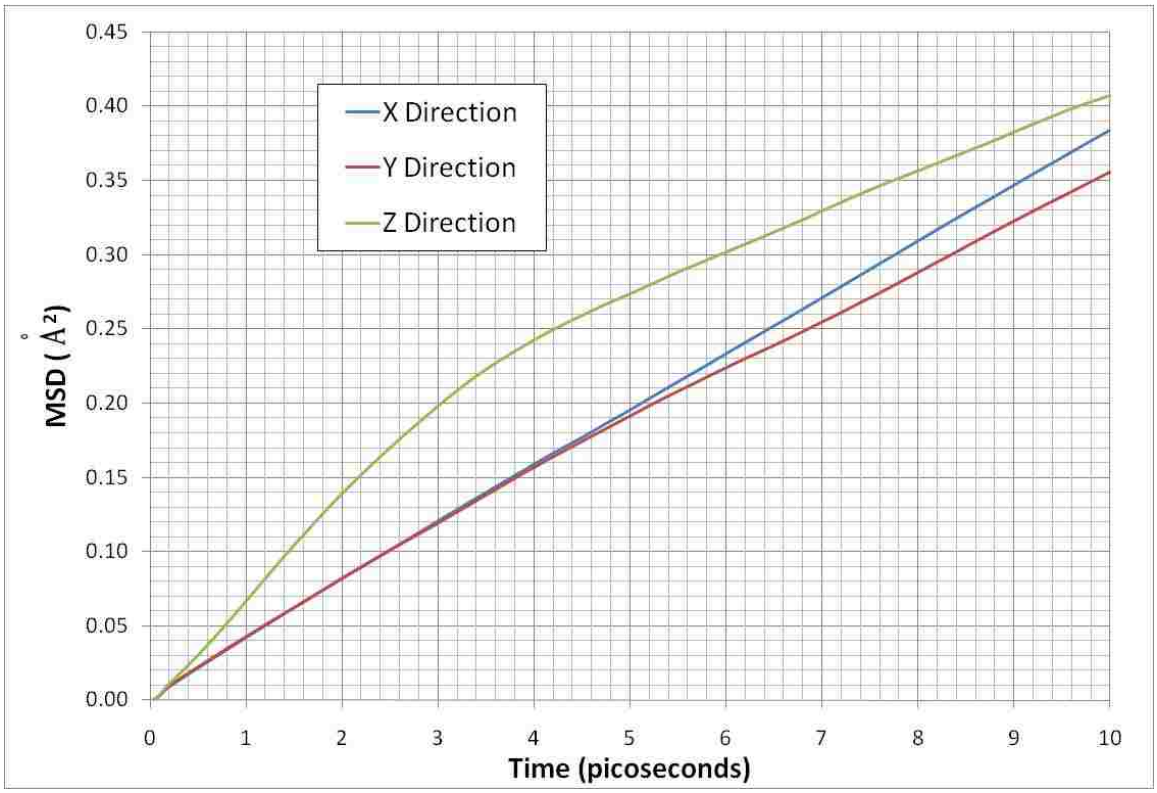

Figure 4.18 Mean square displacements of iron for the case of single iron crystal in liquid lead with the Pb:O atomic ratio at 1:1

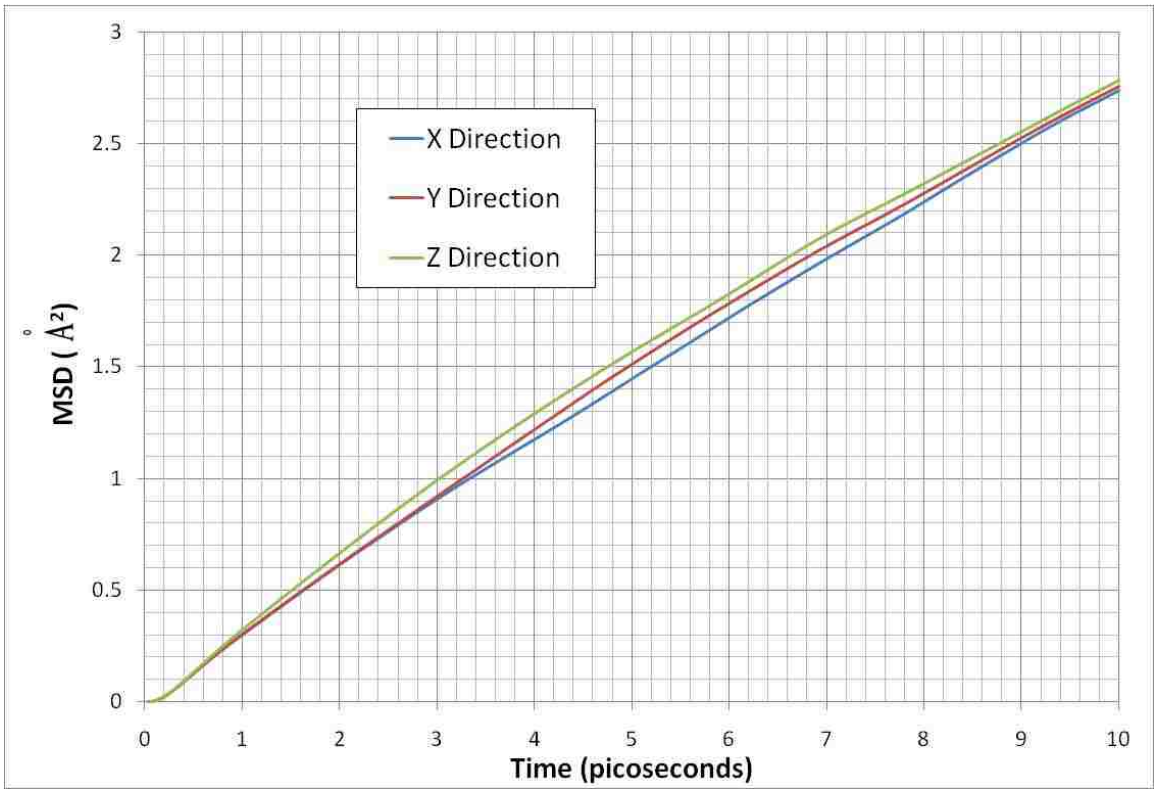

Figure 4.19 Mean square displacements of lead for the case of single iron crystal in liquid lead with the Pb:O atomic ratio at 1:1

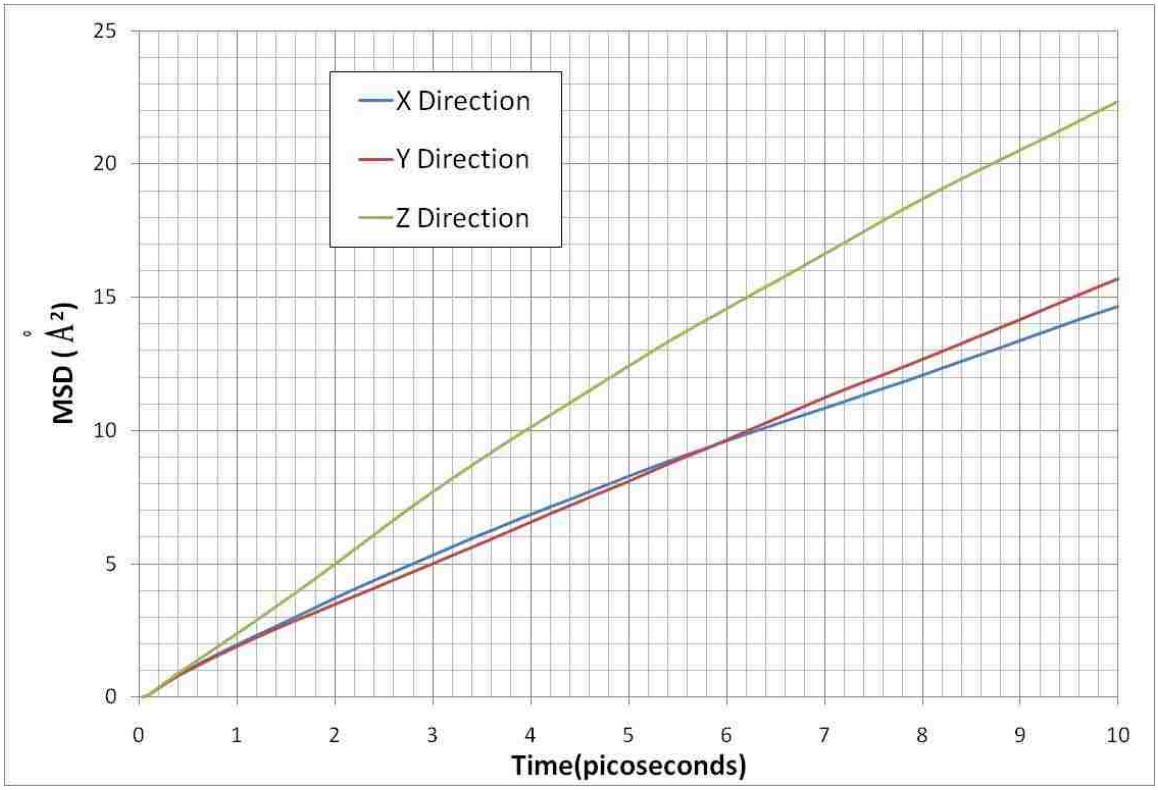

Figure 4.20 Mean square displacements of oxygen for the case of single iron crystal in liquid lead with the Pb:O atomic ratio at 1:1

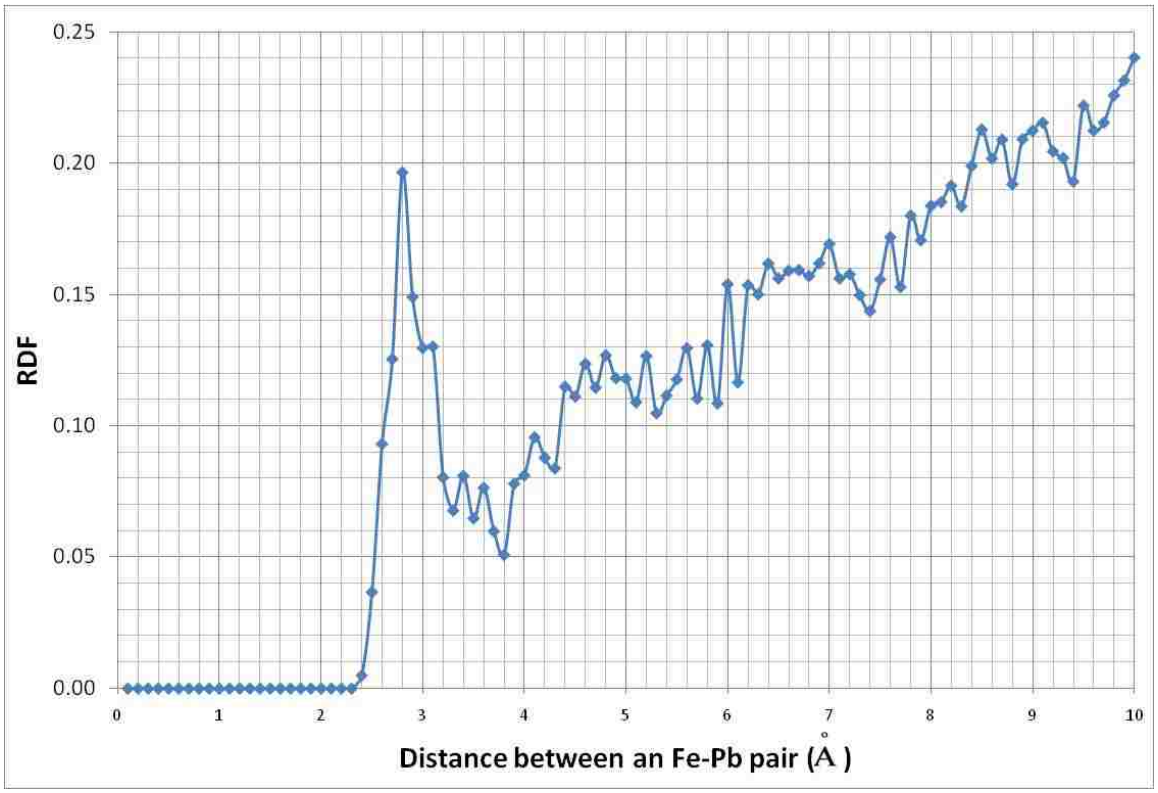

Figure 4.21 Fe-Pb radial distribution function for the case of single iron crystal in liquid lead with the Pb:O atomic ratio at 1:1

4.5.4 Iron Crystals in Liquid Lead without Oxygen

A semi-infinite stab of iron with grain boundaries is put in liquid lead at 550 °C. The iron crystal is 42.67 Å thick in the z direction and infinite in the x-y plane. The simulation run lasts 10 picoseconds in 20,000 time steps. Figures 4.22 and 4.23 show the system at the start and at the end of the simulation run, respectively. At the end of the run, the iron slab is clearly deformed. The slab becomes denser, and, as a result, the overall dimension shrinks. The thickness reduces to 36.54 Å. No lead atoms reach the core of the iron slab.

Lead atoms obviously creep into the slab via the grain boundaries as seen by the blunt penetrations on the surfaces. This is expected because grain boundaries are the sources of defects, which provide easy diffusion paths. However, the grain boundaries are somewhat hard to be noticed at the end of the simulation due to the relaxation of crystals. When heated, the atoms in crystals arrange themselves in order to reduce internal energy as much as possible by eliminating grain boundaries. Small crystals are very quick to relax when heated, and it is not surprising that the same happens in this case. The mean square displacement plots indicate that the system is not approaching an equilibrium after 10 ps (see Figs. 4.24 and 4.25). The closest distance between iron and lead atoms remains $2.8\,\mathring{A}$ as seen from the RDF plot (Fig. 4.26).

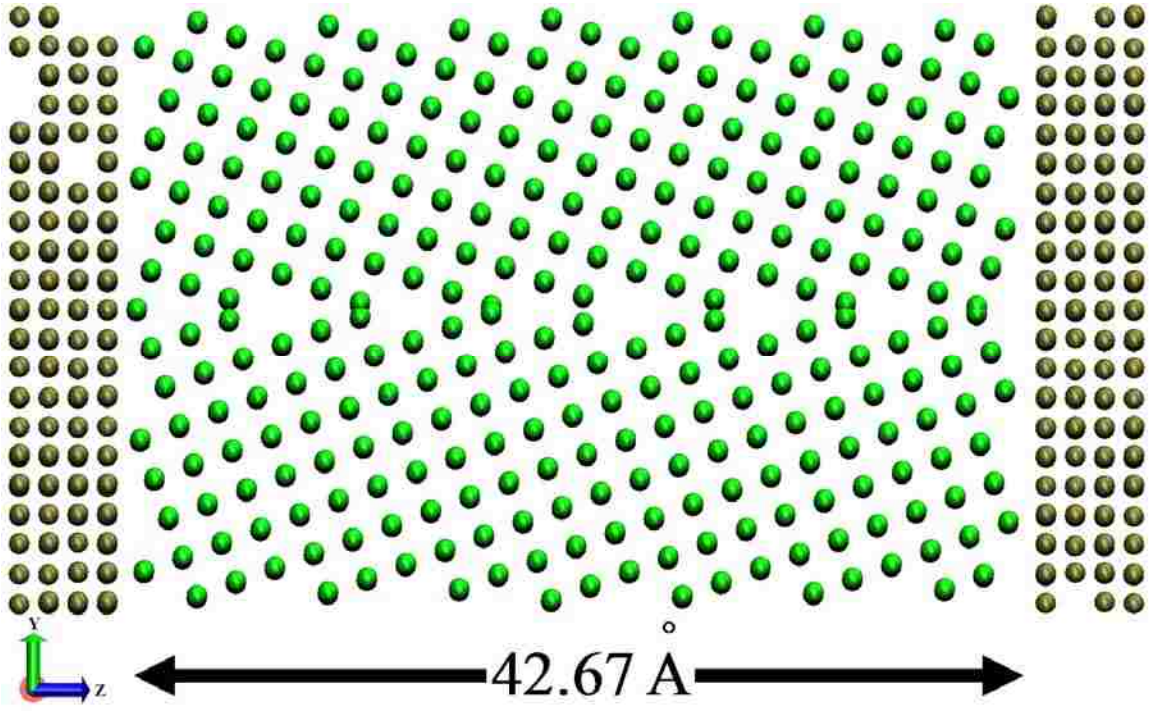

Figure 4.22 The initial setup of iron crystals in liquid lead without oxygen

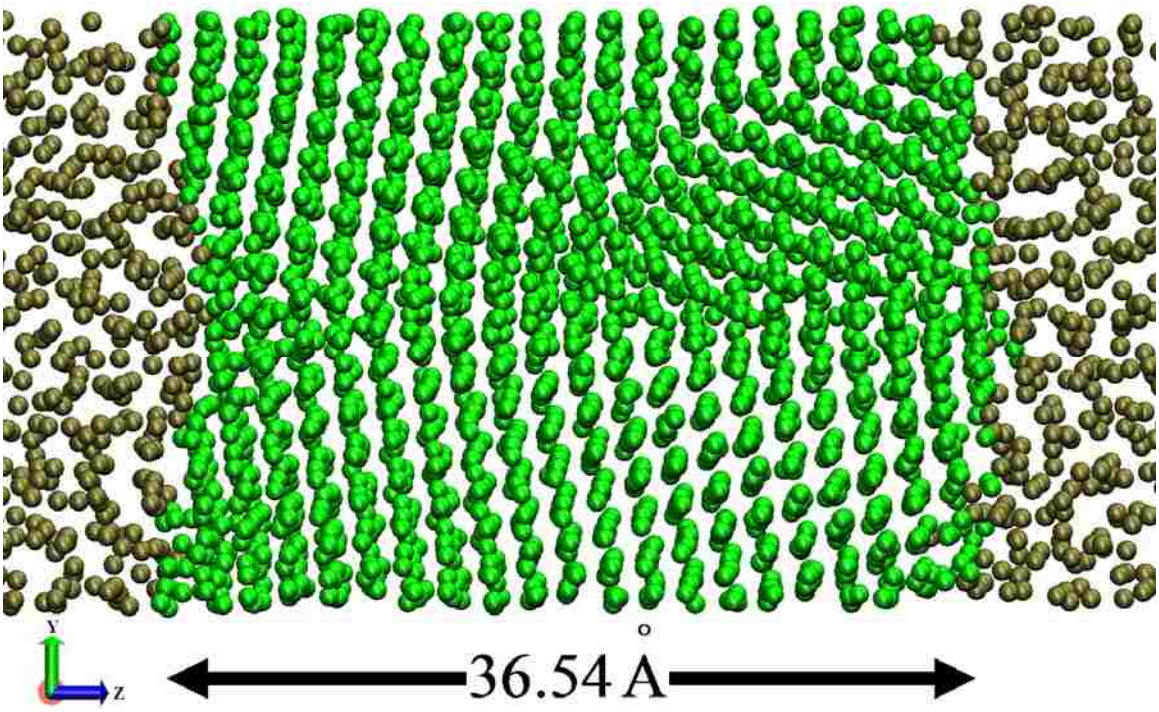

Figure 4.23 Iron crystals in liquid lead without oxygen at the end of the 10-ps simulation run

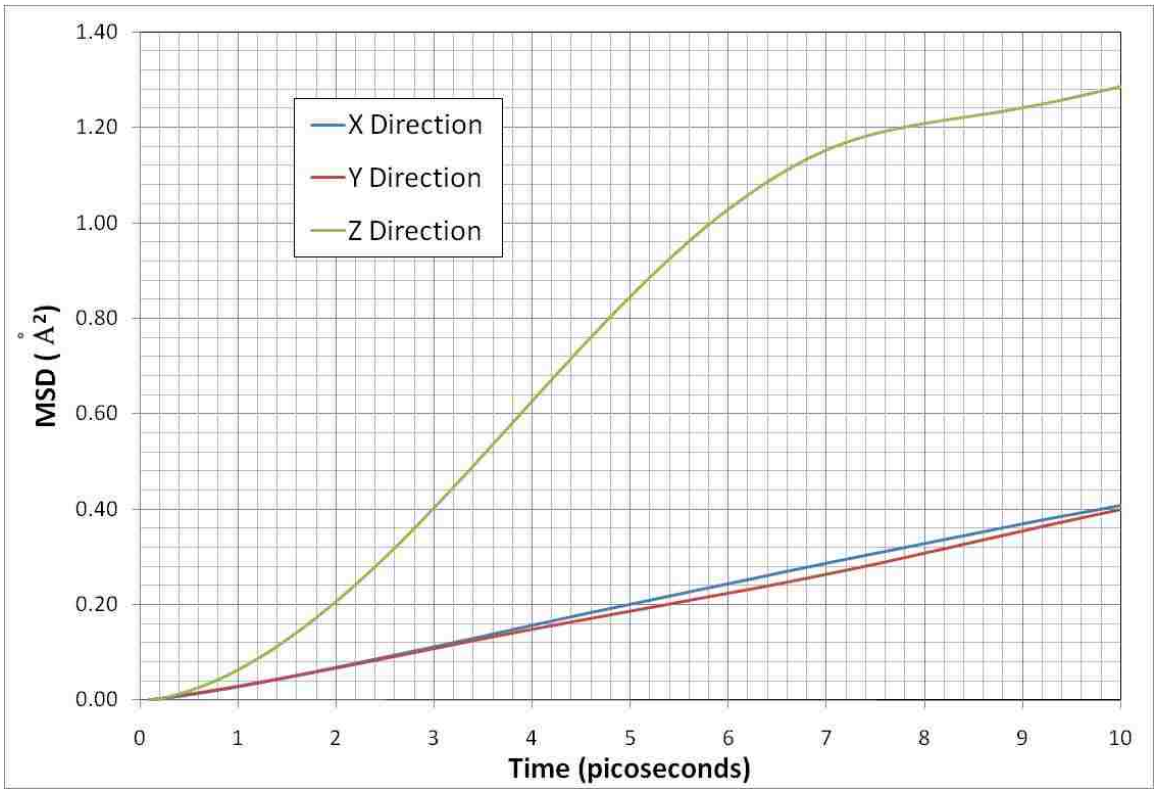

Figure 4.24 Mean square displacements of iron for the case of iron crystals in liquid lead without oxygen

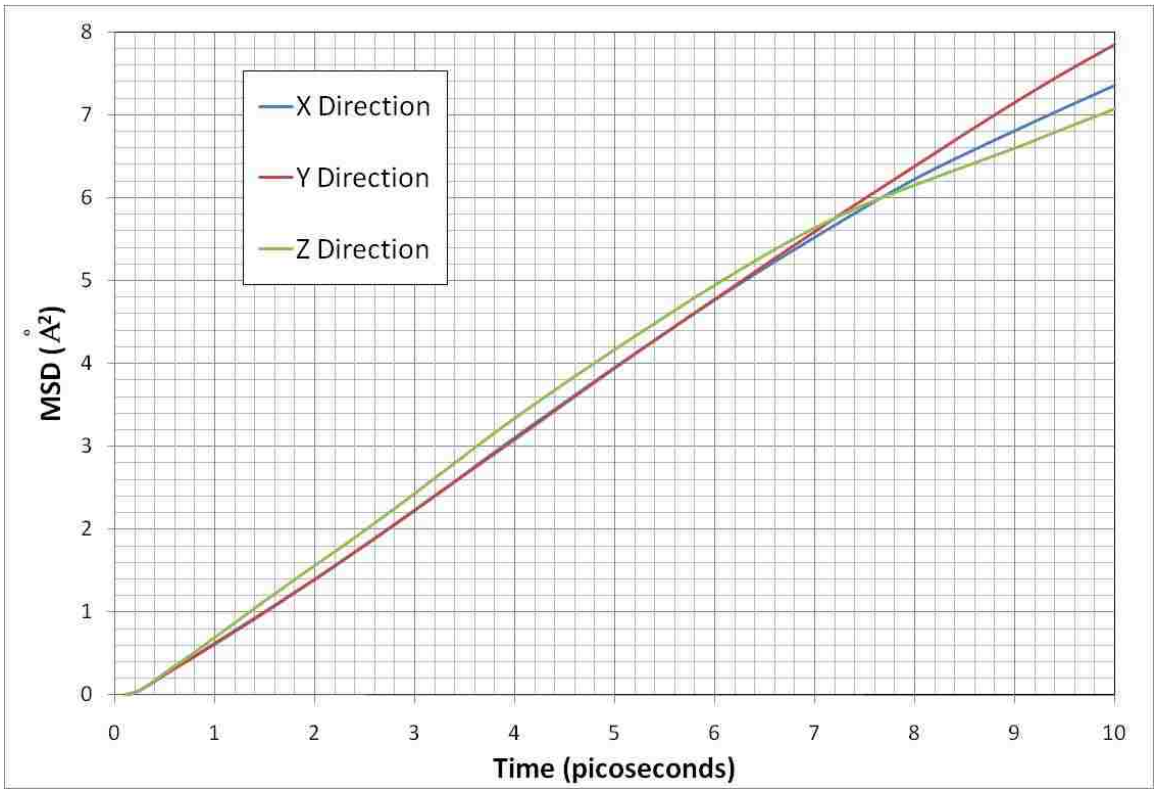

Figure 4.25 Mean square displacements of lead for the case of iron crystals in liquid lead without oxygen

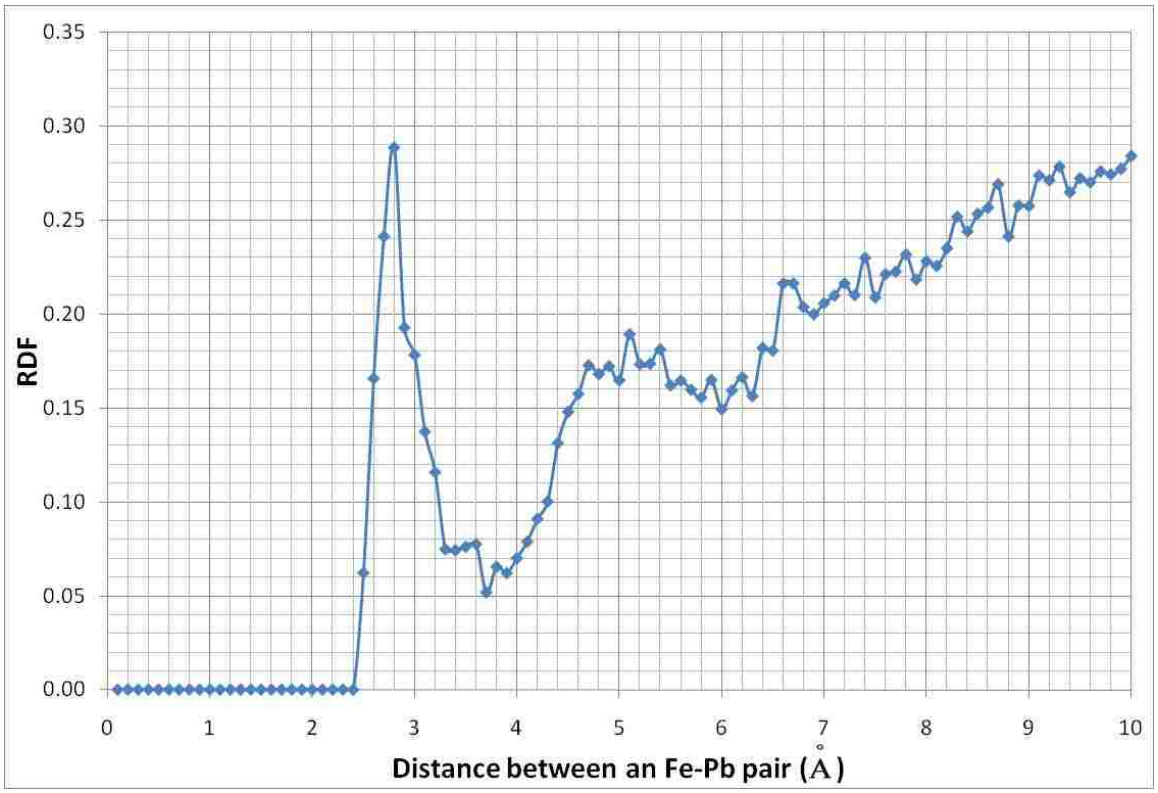

Figure 4.26 Fe-Pb radial distribution function for the case of iron crystals in liquid lead without oxygen

4.5.5 Iron Crystals in Liquid Lead with Oxygen at 1.3×10^{-3} wt. %

A semi-infinite stab of iron with grain boundaries is put in liquid lead at 550 °C. Oxygen is randomly distributed in liquid lead at the ratio of one oxygen atom to sixty lead atoms, corresponding to 1.3×10^{-3} wt. %. The iron crystal is 42.67 Å thick in the z direction and infinite in the x-y plane. The simulation run lasts 10 picoseconds in 50,000 time steps.

Figures 4.27 and 4.28 show the system at the start and end of the simulation run, respectively. At the end of the 10-ps run, the iron slab is not as badly deformed as in the previous case of the no-oxygen system. The grain boundaries are easier to be noticed

compared to the previous case. The mobility of iron atoms becomes limited compared to the previous case as shown in the MSD plot of iron (Fig 4.29). Lead atoms still try to penetrate at the grain boundaries, obviously at a slower rate as seen from the MSD plot of lead (Fig. 4.30). The MSD plot of oxygen is shown in Fig. 4.31. Oxygen in the system acts as a corrosion inhibitor, and it slows down the activity of lead. So the lead atoms do not creep into slab as deep as in the previous case. The mean square plots also support this limited mobility of lead atoms in the x, y, and z directions, compared to the previous case. The RDF plot in Fig. 4.32 shows that the closest distance between iron and lead atoms is $4.27\,\mathring{A}$, $1\,\mathring{A}$ closer than all previous cases.

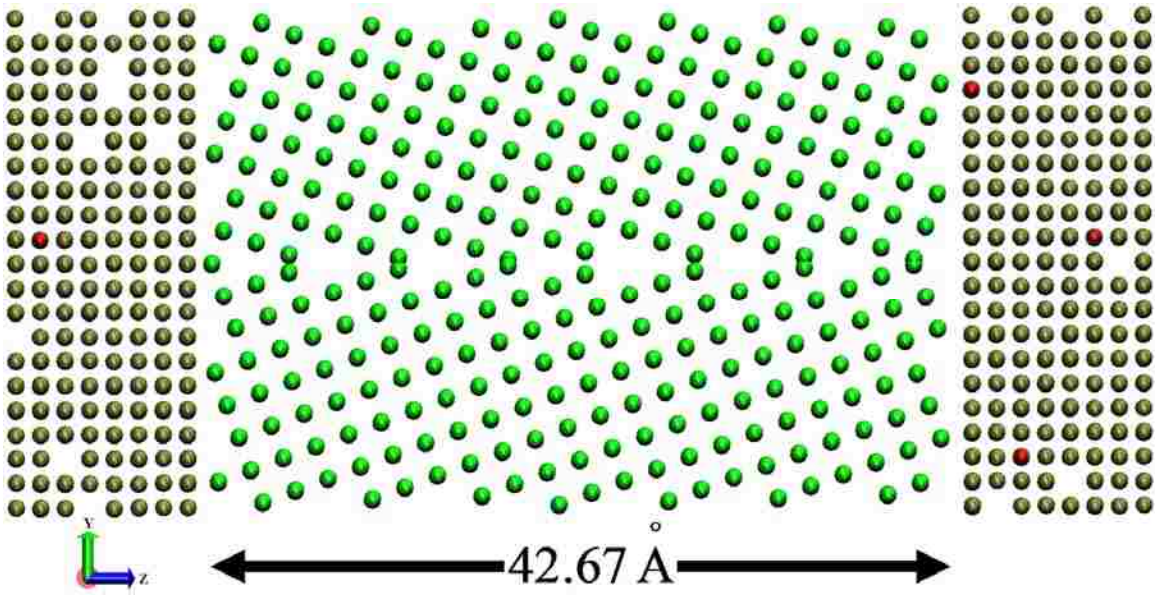

Figure 4.27 The initial setup of iron crystals in liquid lead with dissolved oxygen at 1.3×10^{-3} wt. %

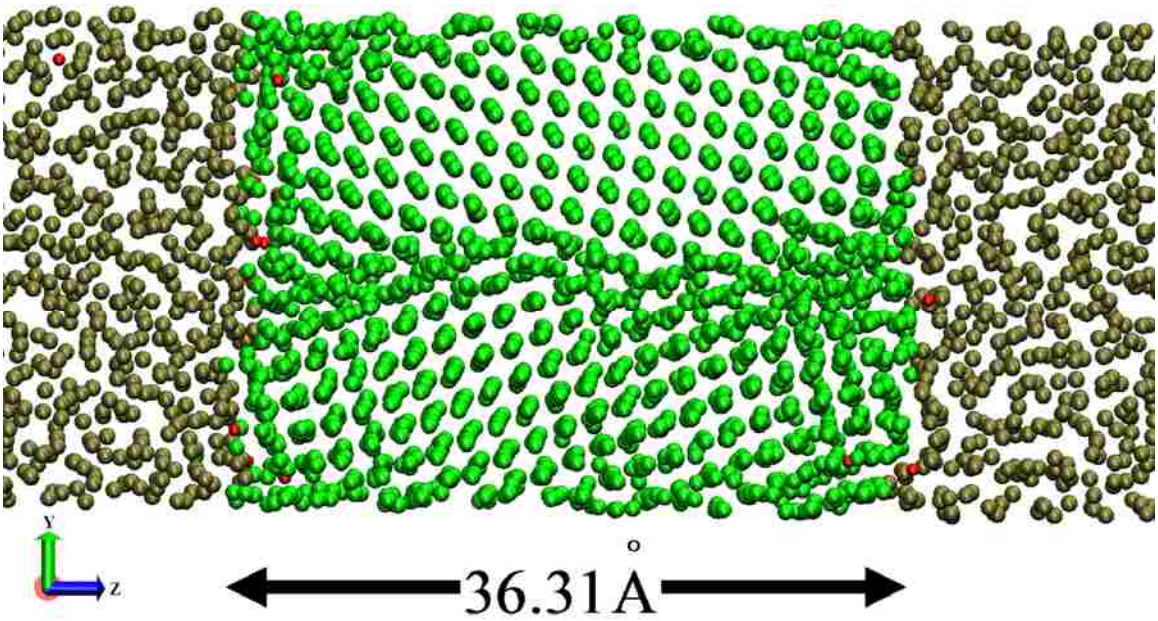

Figure 4.28 Iron crystals in liquid lead with dissolved oxygen at 1.3×10^{-3} wt. % at the end of 10-ps simulation run

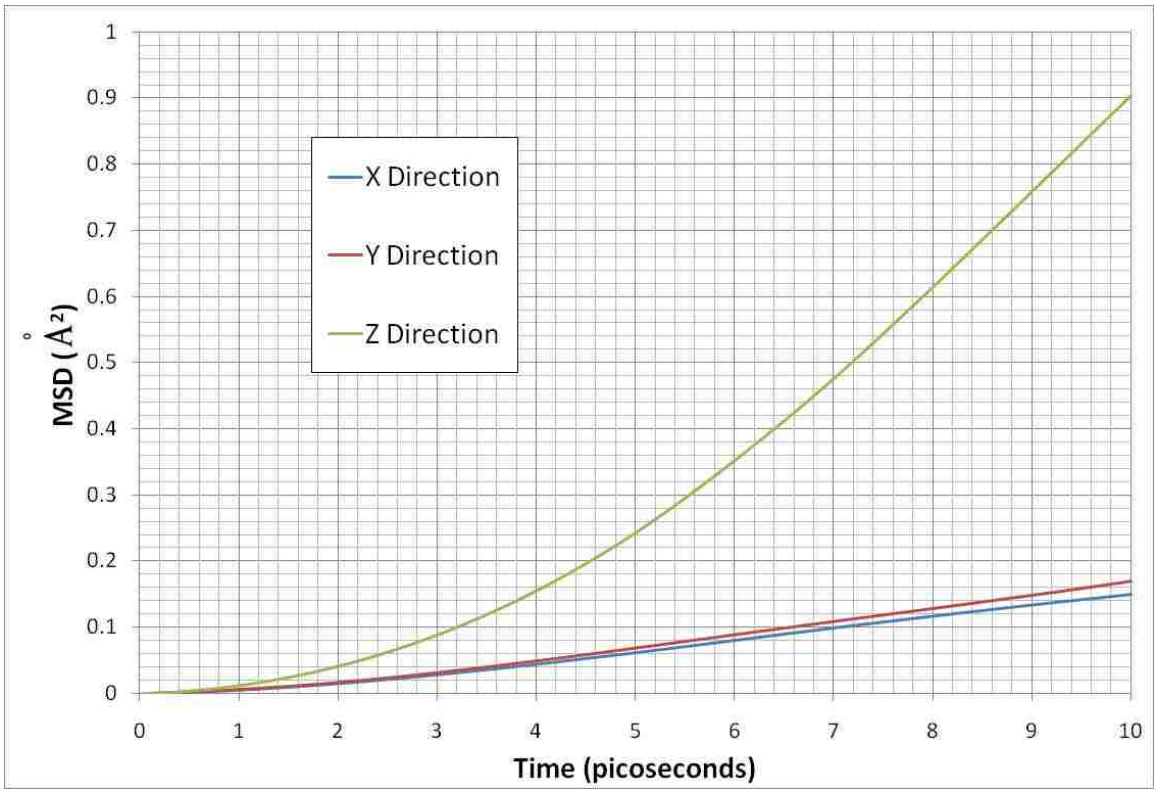

Figure 4.29 Mean square displacements of iron for the case of iron crystals in liquid lead with dissolved oxygen at 1.3×10^{-3} wt. %

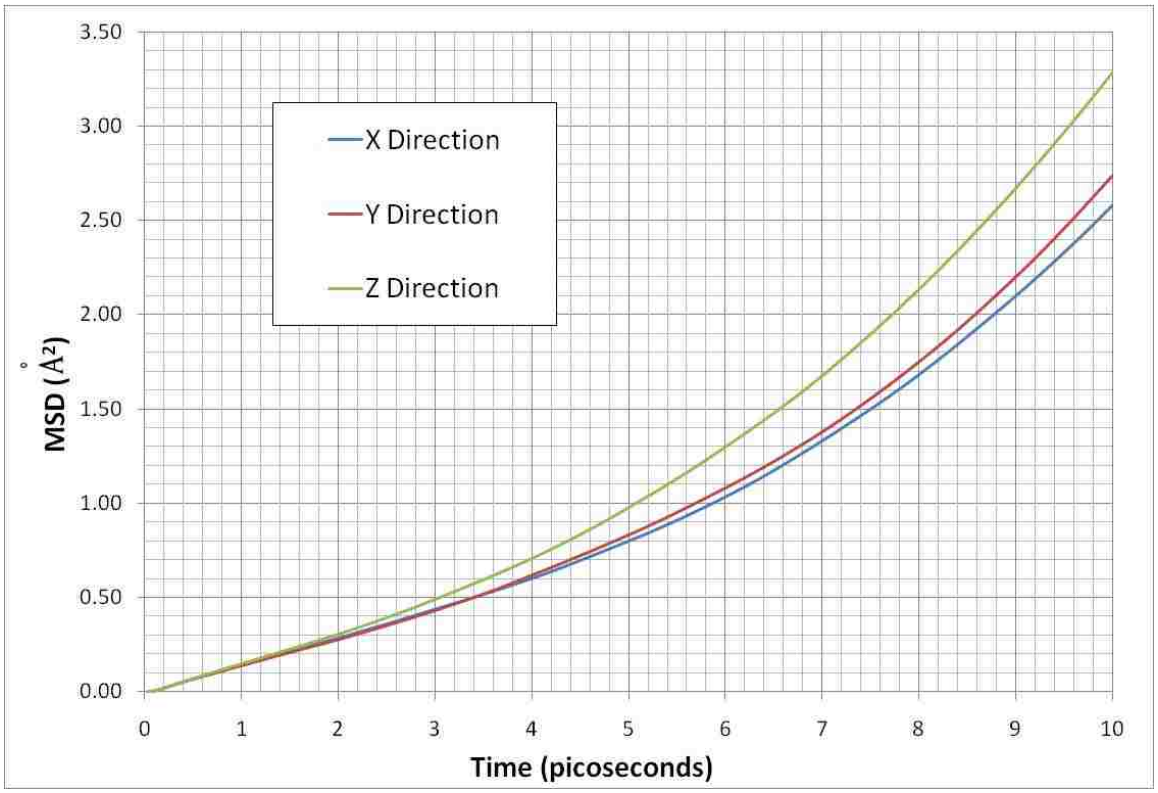

Figure 4.30 Mean square displacements of lead for the case of iron crystals in liquid lead with dissolved oxygen at 1.3×10^{-3} wt. %

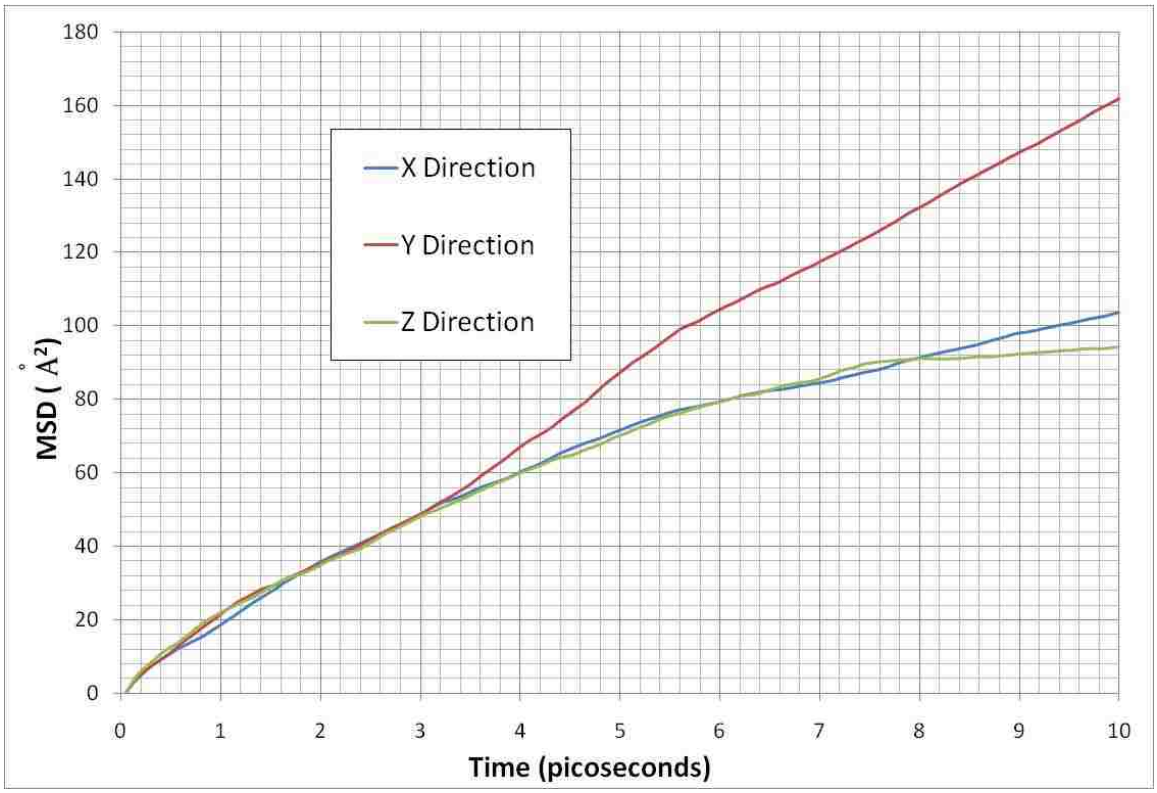

Figure 4.31 Mean square displacements of oxygen for the case of iron crystals in liquid lead with dissolved oxygen at 1.3×10^{-3} wt. %

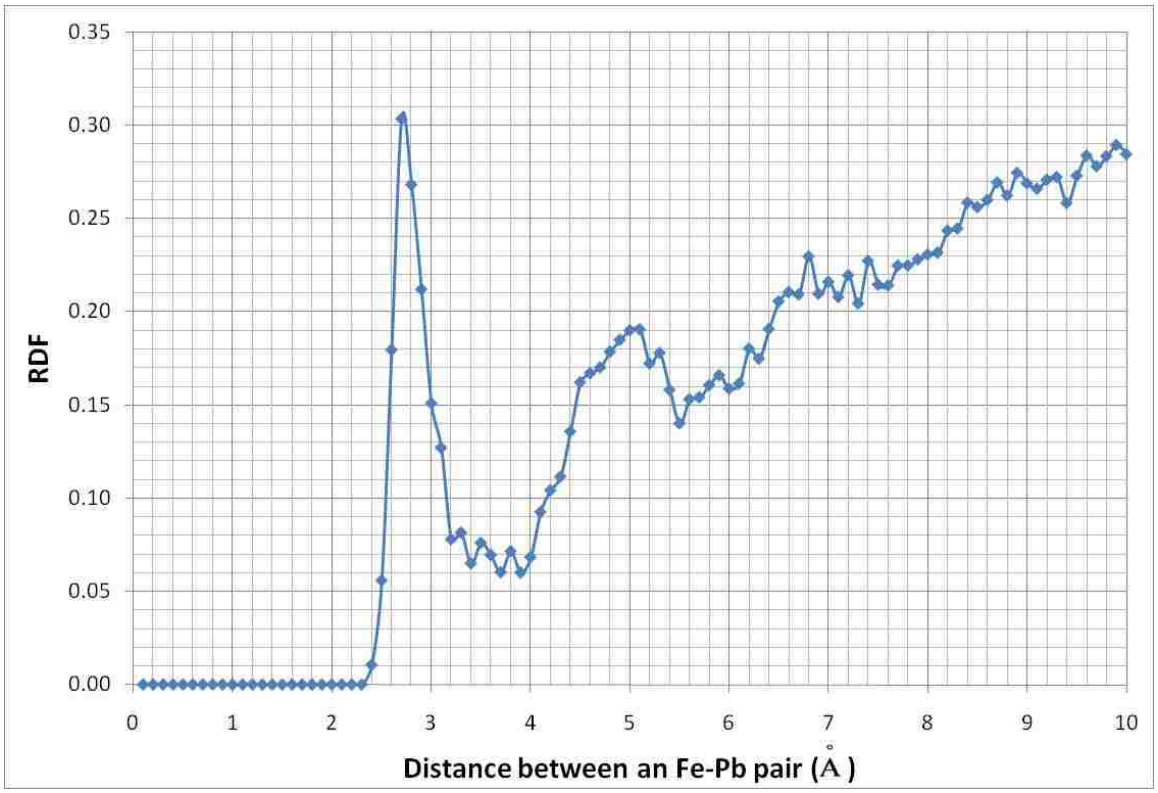

Figure 4.32 Fe-Pb radial distribution function for the case of iron crystals in liquid lead with dissolved oxygen at 1.3×10^{-3} wt. %

4.5.6 Iron Crystals in Liquid Lead with Oxygen at Pb:O = 1:1

A semi-infinite stab of iron with grain boundaries is put in liquid lead at 550 °C. Oxygen is randomly distributed in liquid lead at the ratio of one oxygen atom to one lead atom. The iron crystal is 42.67 Å thick in the z direction and infinite in the x-y plane. The simulation run lasts 10 picoseconds in 50,000 time steps.

Figures 4.33 and 4.34 show the system at the start and end of the simulation run, respectively. At the end of the 10-ps run, the grain boundaries remain noticeable. The iron slab is oxidized on both sides of the slab with the oxide film thickness of about 4.1 Å. Virtually, no lead atoms reach the slab core. Most of lead atoms stay on the slab

surfaces, and only a few lead atoms manage to get below the surfaces. The mean square displacement plots (Figs. 4.35 to 4.37) suggest that the system does not approach its equilibrium after 10 ps. According to the radial distribution function for iron and lead atoms (Fig. 4.38), the closest distance between a pair of iron and lead is $2.8\,\mathring{A}$

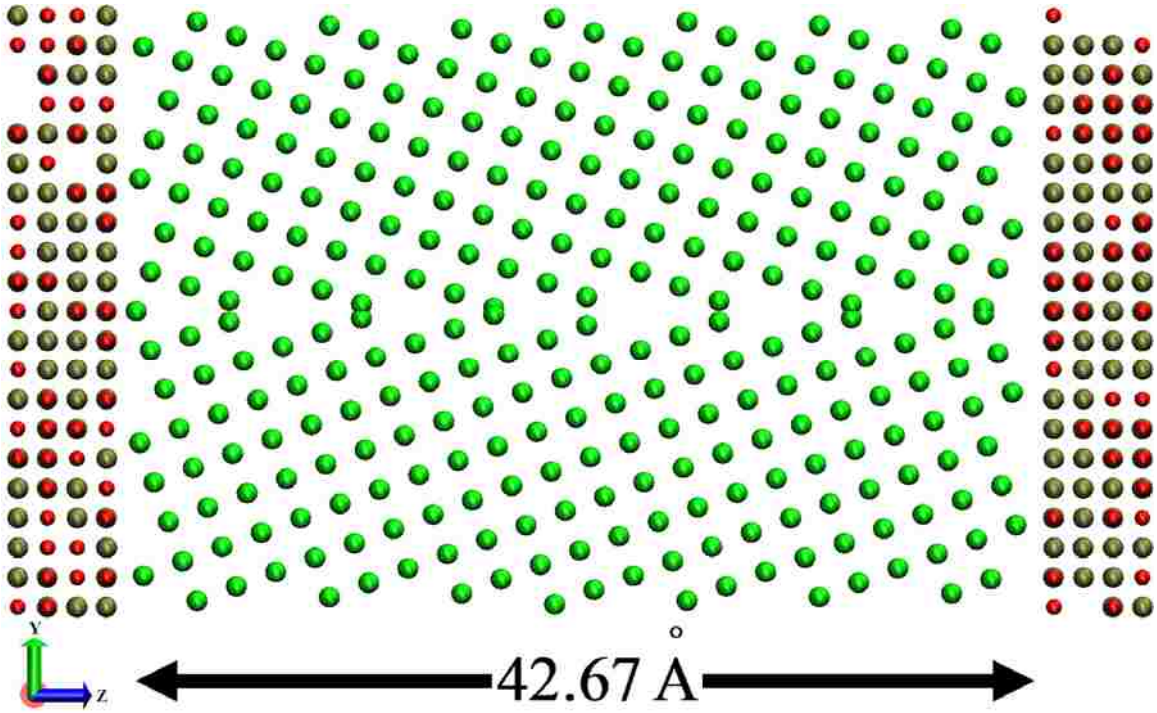

Figure 4.33 The initial setup of iron crystals in liquid lead with the Pb:O atomic ratio at 1:1.

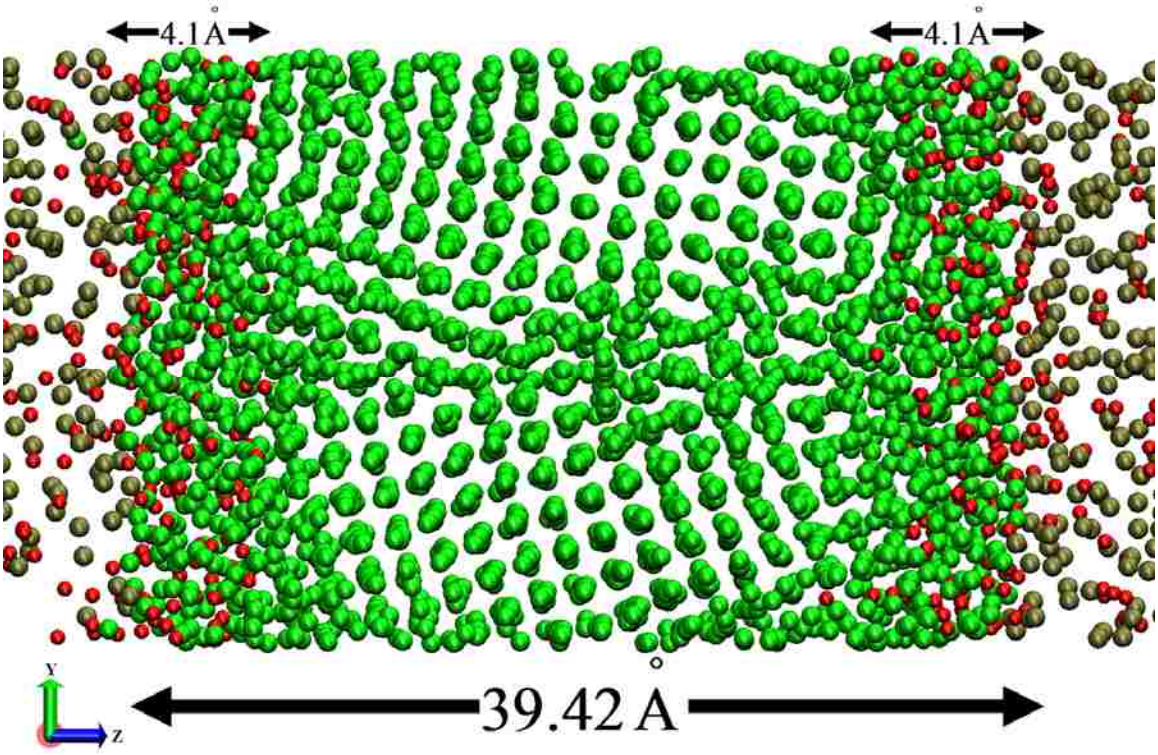

Figure 4.34 The end of the 10-ps simulation run of the iron crystals in liquid lead with the Pb:O atomic ratio at 1:1

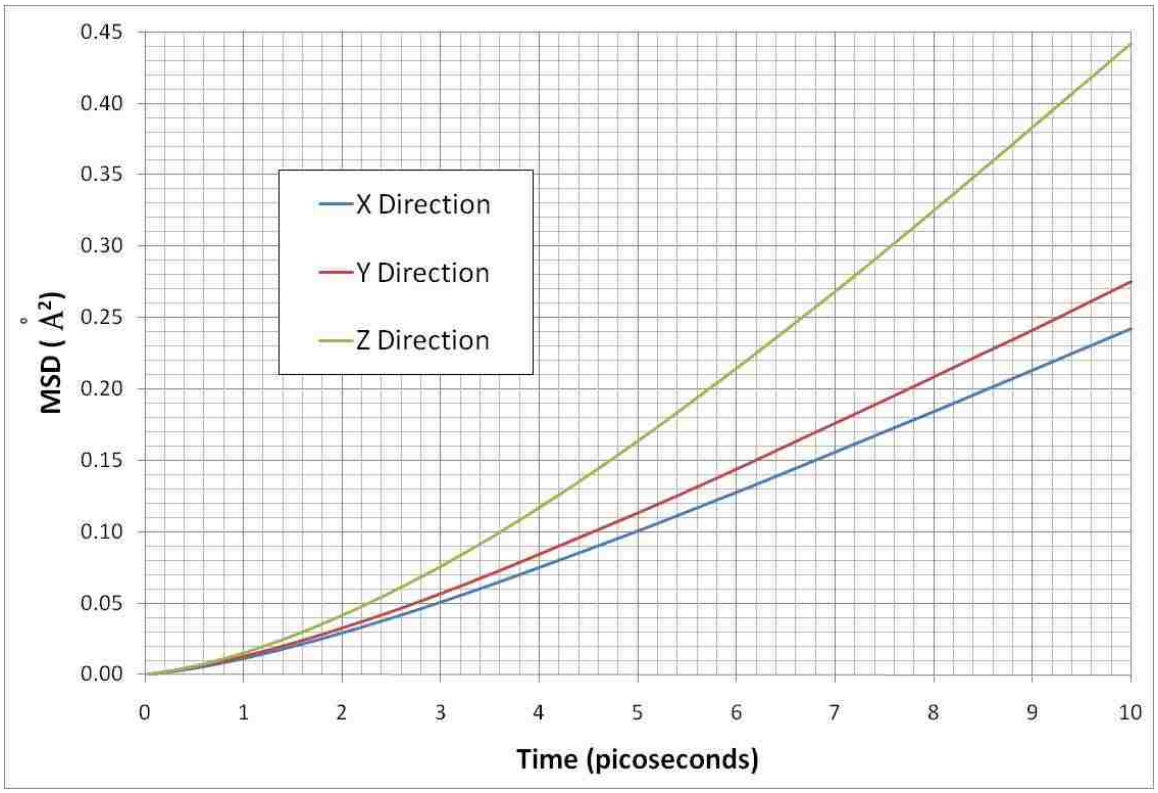

Figure 4.35 Mean square displacements of iron for the case of iron crystals in liquid lead with the Pb:O atomic ratio at 1:1

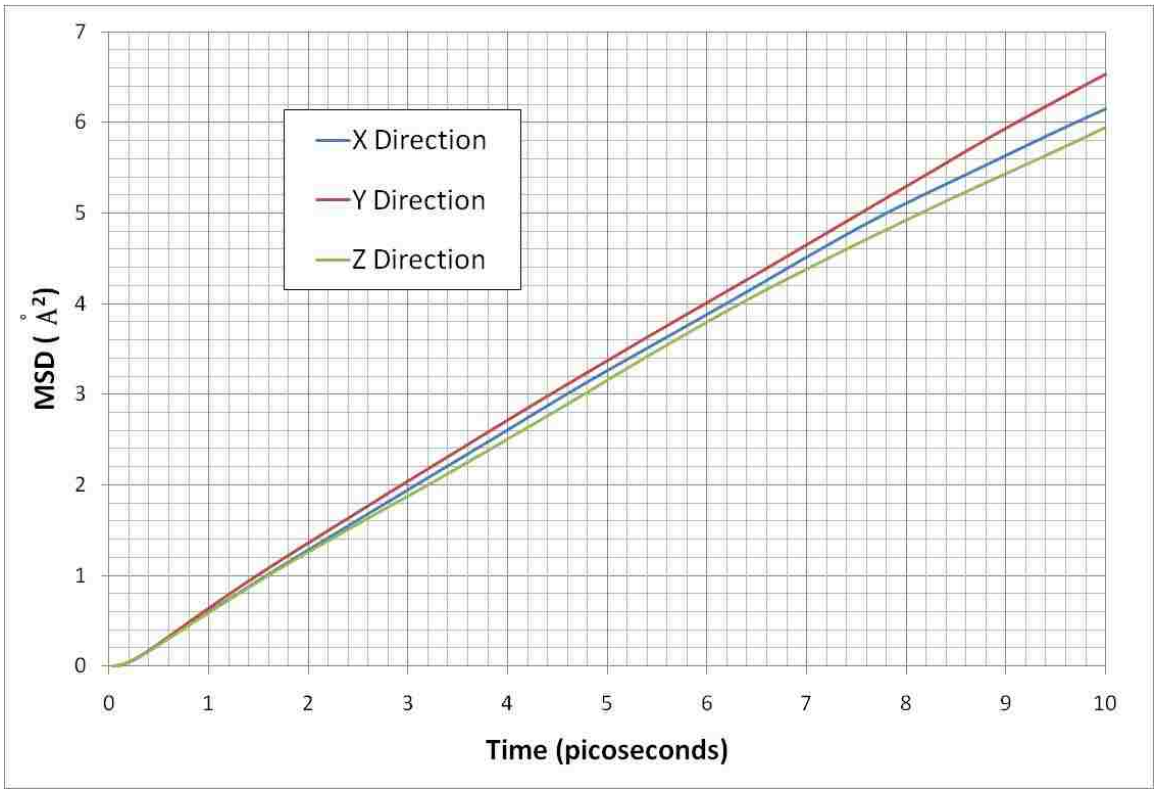

Figure 4.36 Mean square displacements of lead for the case of iron crystals in liquid lead with the Pb:O atomic ratio at 1:1

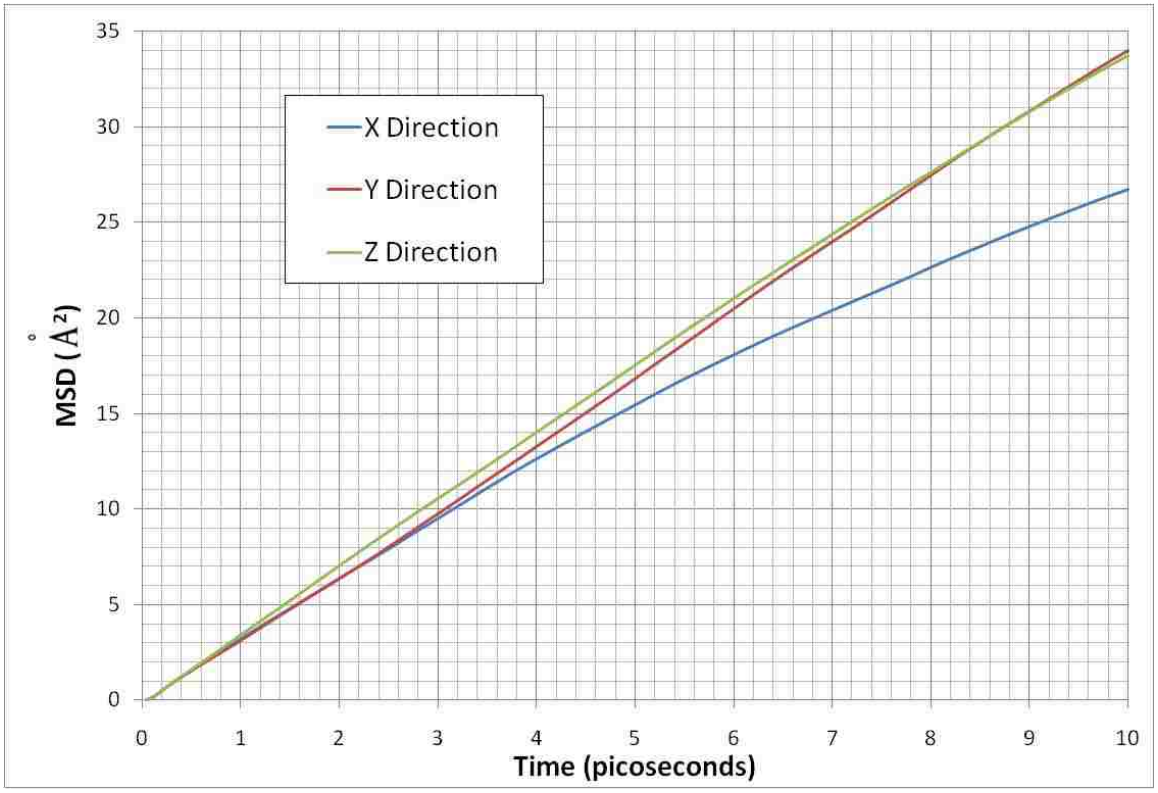

Figure 4.37 Mean square displacements of oxygen for the case of iron crystals in liquid lead with the Pb:O atomic ratio at 1:1

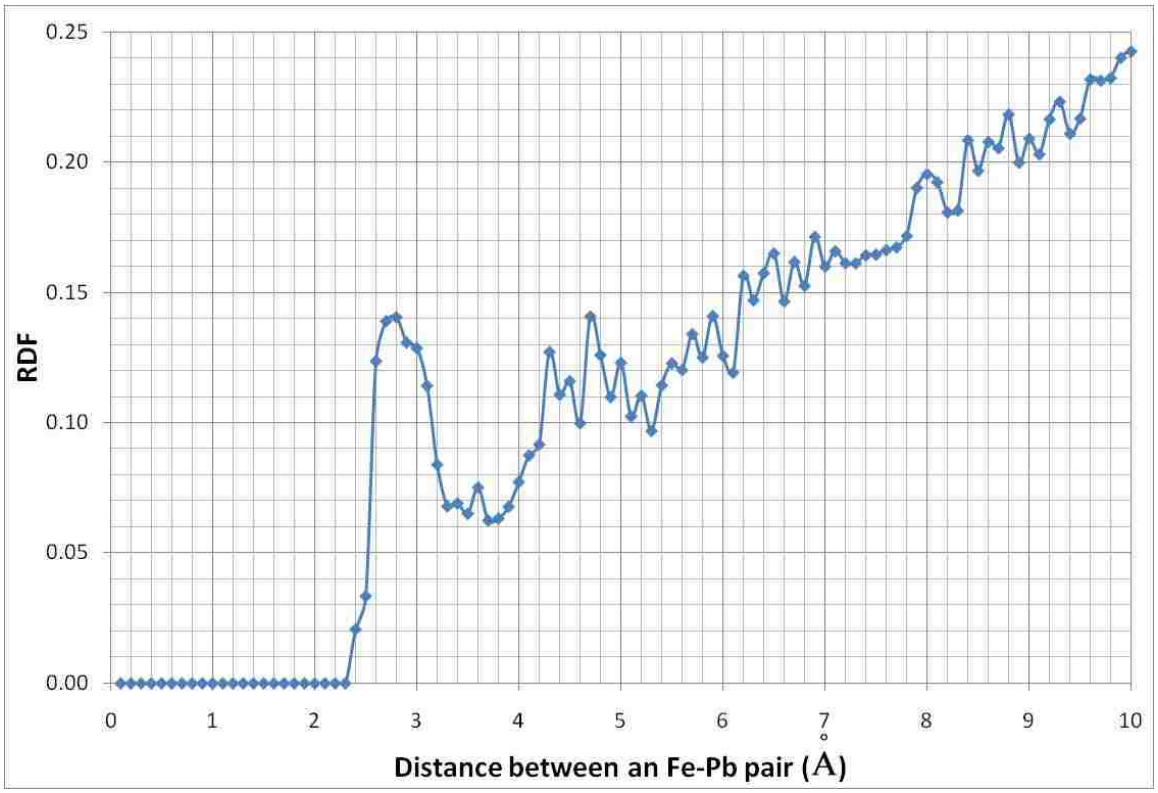

Figure 4.38 Fe-Pb radial distribution function for the case of iron crystals in liquid lead with the Pb:O atomic ratio at 1:1

4.6 Discussion of Simulation Results

The simulation runs as shown in Table 4.6 have been completed. All six cases represent the limiting scenarios in the systems consisting of iron, liquid lead, and oxygen. Below are the detailed discussions regarding the following four attributions from the six cases: (1) deformation, (2) wettability, (3) penetration depth of lead, and (4) dissolution.

In all cases, the slabs exhibit deformation from their original shapes to some extent. The slab thickness is calculated by first finding the averaged z-coordinate z_{avg} and then seeking a positive value Δz such that the 95% of the total iron atoms locate between $z_{avg} \pm \Delta z$. This represents the conventional 95% confidence interval, and the

slab thickness is approximated by $2\Delta z$. Table 4.7 shows the value of $z_{avg} \pm \Delta z$ at the end of the simulation in all six cases. The reduction in the slab thickness ranges from about 6% to 15% as shown in Table 4.8. Overall, the cases with grain boundaries have larger reductions in thickness, compared to the single crystal cases. This is because grain boundaries provide extra space for iron atoms to relocate to when lead atoms are compressing the iron slab surfaces.

Wettability enhances penetration of lead into bulk iron. Better wettability usually provides good surface adsorption. In the atomic level, wettability of lead on the surfaces of iron can be roughly gleaned from how dense lead atoms on the contacting surfaces are. The distribution histograms offer this information. Figures 4.39 to 4.44 show the histograms with the number of atoms displayed for each location bin. Each bin contains the atoms that have the z coordinates between the intervals on the axis. The highlighted sections represent the majority of the iron atoms (more than 95% of the total iron atoms) making up the slabs. Across the six cases, the cases with grain boundaries clearly stand out as having "wetter" surfaces. There are more lead atoms on the surfaces of the multi-crystalline slabs than those of the single-crystal slabs (see Table 4.9). In the single iron crystal cases, oxygen adversely affects the well-ordered, uniform surfaces of those single crystals. The surfaces of the single crystals become rough when reacted with oxygen, and that favor the wettability of lead atoms.

Table 4.7 The iron slab positions along the z-direction at the end of the simulations

	Z-coordinate range of slab iron $z_{avg} \pm \Delta z$ ($\mathring{A}$)	
	No Grain Boundary	With Grain Boundary
No Oxygen	0.78 ± 18.82 (-18.04 to 19.60)	0.07 ± 18.27 (-18.20 to 18.34)
O_2 at solubility limit	0.28 ± 18.82 (-18.54 to 19.10)	-0.17 ± 18.16 (-18.33 to 17.98)
Pb:O at 1:1 (atomic)	-0.05 ± 20.26 (-20.31 to 20.20)	-0.14 ± 19.71 (-19.85 to 19.57)

Table 4.8 Thicknesses of the iron slabs at the end of the simulation runs

	Slab Thickness ($\mathring{A}$)					
	No Grain Boundary			With Grain Boundary		
	Start	End	% chg	Start	End	% chg
No Oxygen	43.02	37.64	13%	42.67	36.54	14%
Oxygen at solubility limit	43.02	37.64	13%	42.67	36.31	15%
Pb:O at 1:1 atomic ratio	43.02	40.51	6%	42.67	39.42	8%

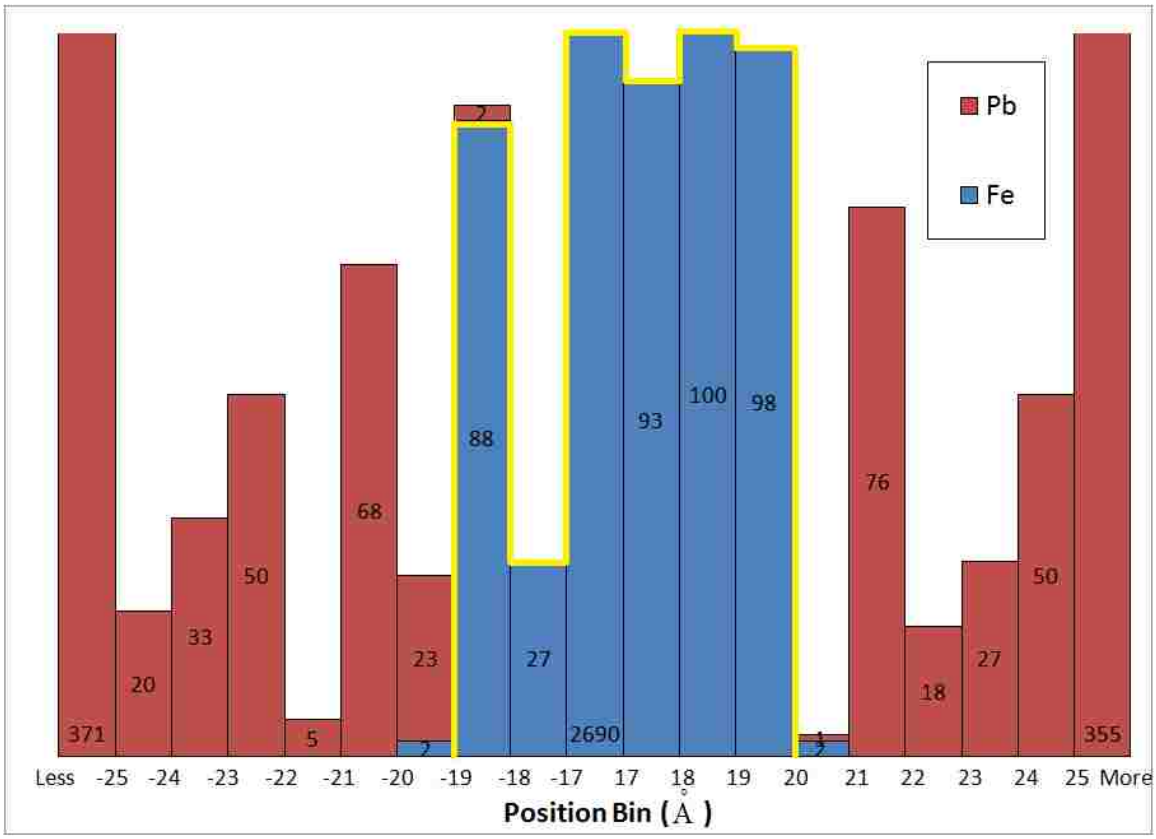

Figure 4.39 Histogram of atom positions along the z direction in the case of single crystal of iron in liquid lead without oxygen

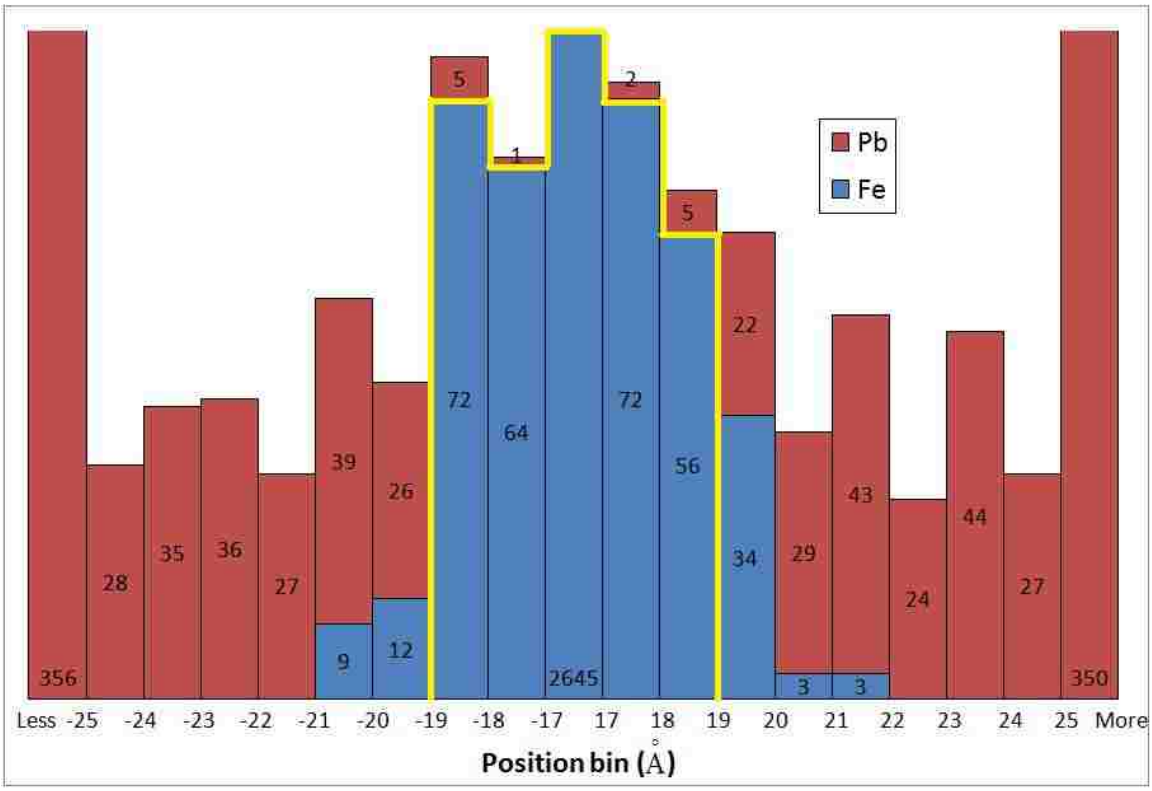

Figure 4.40 Histogram of atom positions along the z direction for the case of iron crystals in liquid lead without oxygen

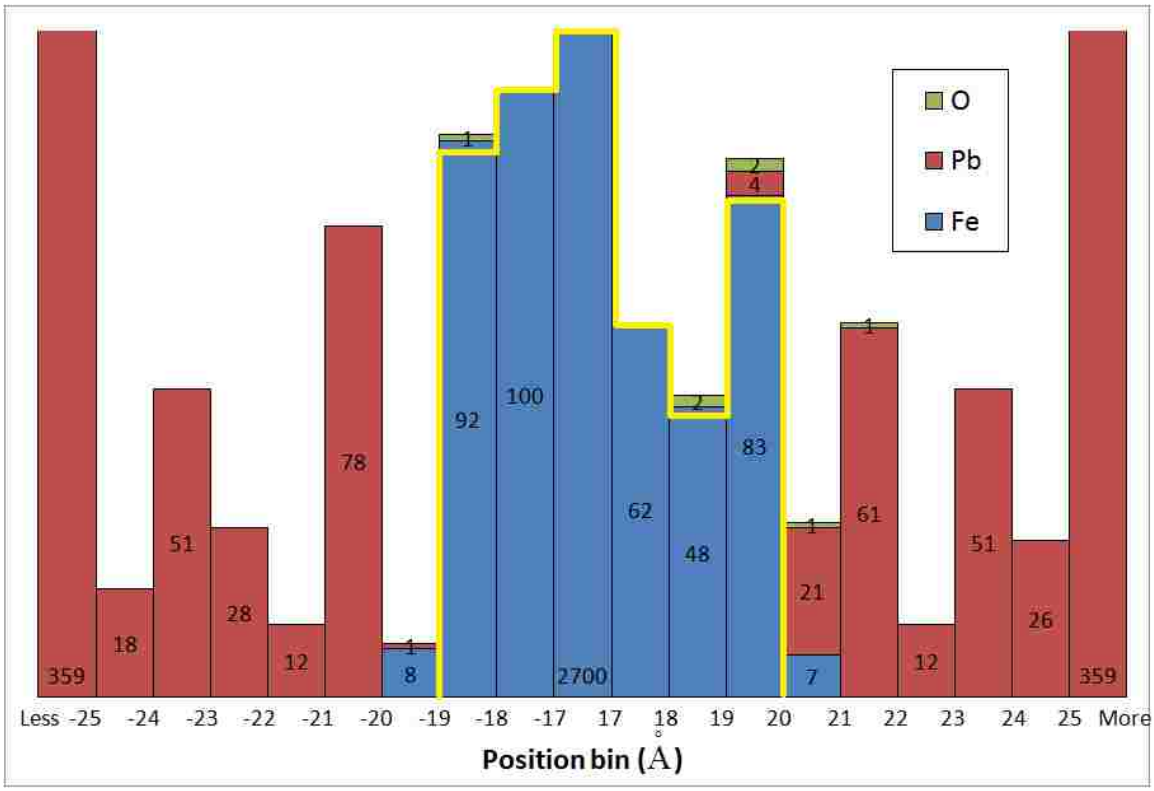

Figure 4.41 Histogram of atom positions along the z direction for the case of single crystal of iron in liquid lead saturated with oxygen

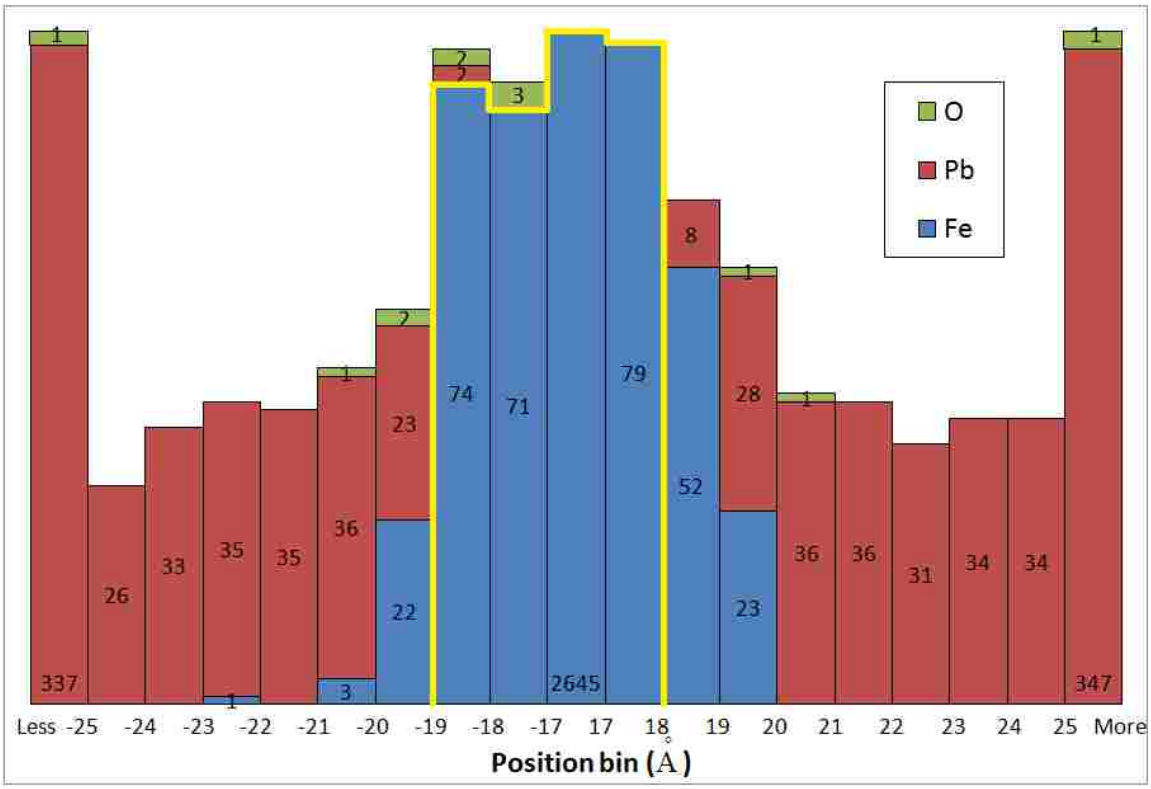

Figure 4.42 Histogram of atom positions along the z direction for the case of iron crystals in liquid lead saturated with oxygen

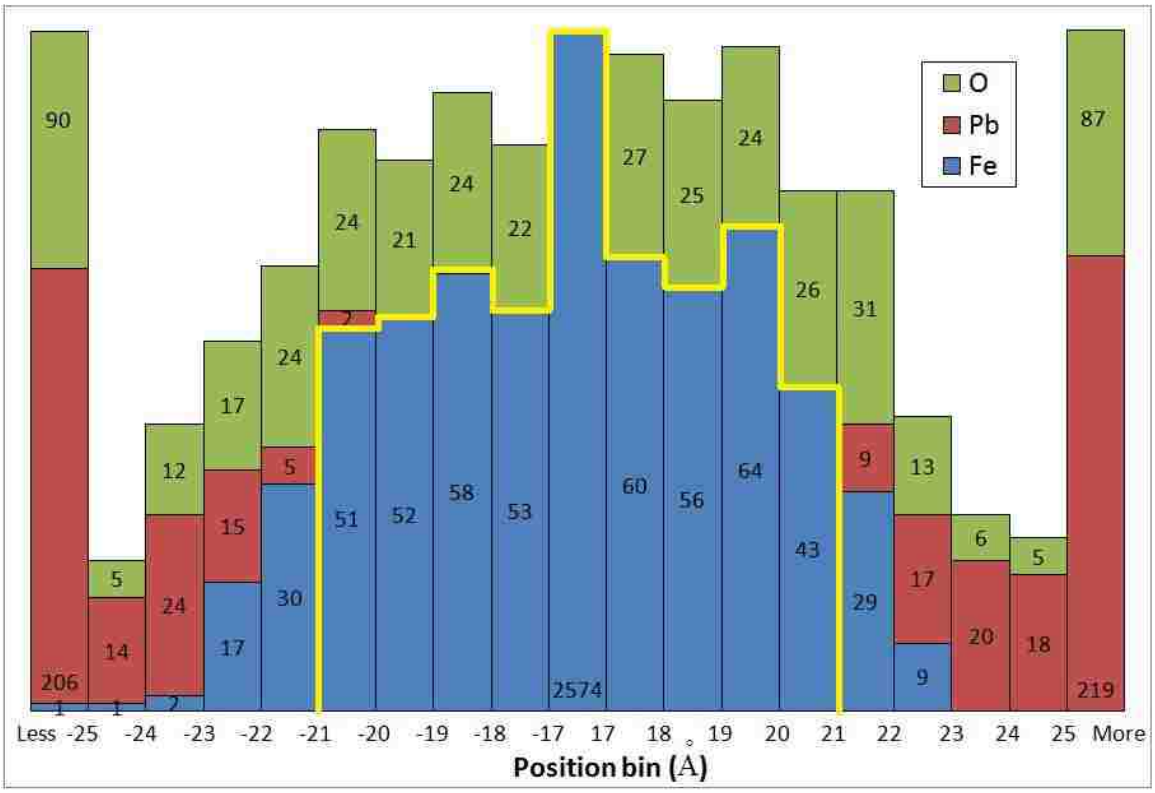

Figure 4.43 Histogram of atom positions along the z direction for the case of iron single crystal in liquid lead with the Pb:O atomic ratio at 1:1

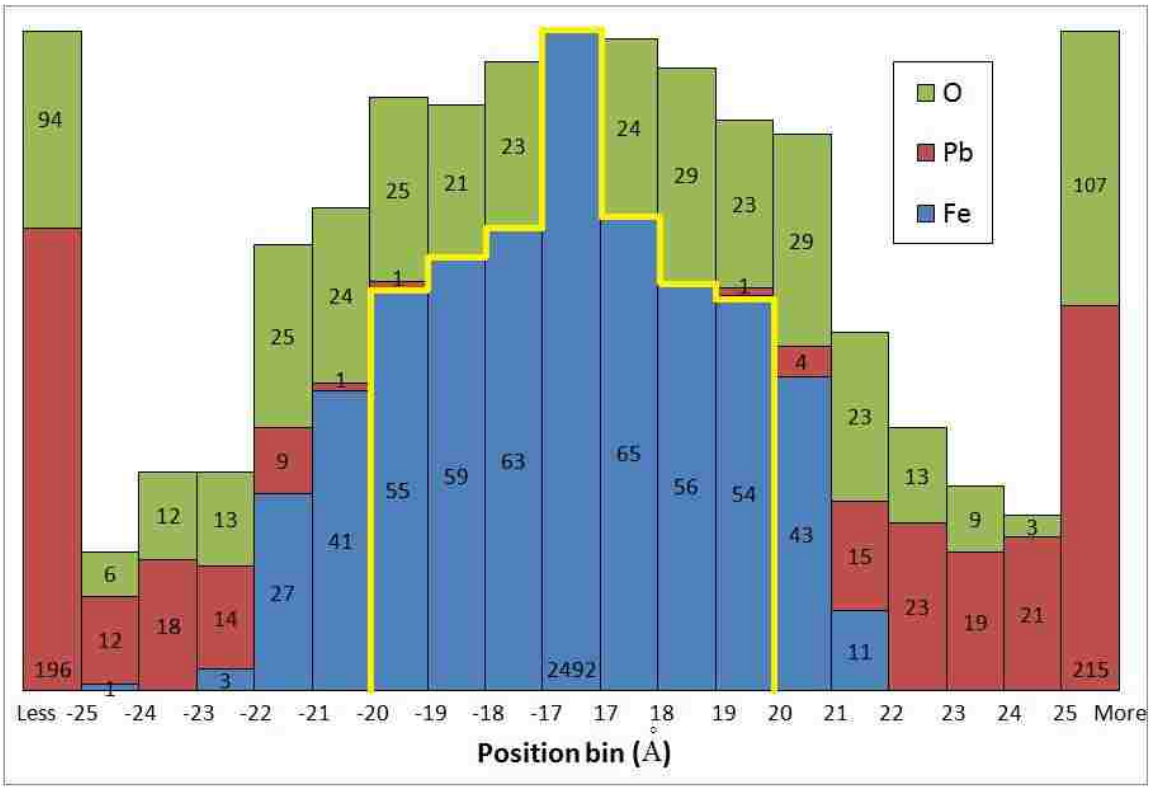

Figure 4.44 Histogram of atom positions along the z direction for the case of iron crystals in liquid lead with the Pb:O atomic ratio at 1:1

Table 4.9 The number of Pb atoms on the Fe surfaces at the end of each simulation

	Number of Lead Atoms on Iron Slab Surface	
	No Grain Boundary	With Grain Boundary
No Oxygen	24	48
Oxygen at Solubility Limit	22	31
Pb:O at 1:1 atomic ratio	14	5

From the same histograms, in terms of preventing the penetration of lead atoms, the cases with grain boundaries usually perform worse than the cases without grain

boundaries. More traces of lead atoms enter deeper under the slab surfaces. However, when there is enough oxygen in the systems, oxygen enters much deeper than lead atoms. It is evident that fewer lead atoms reach the inner slab cores when the slabs are oxidized as seen from the histograms. This clearly indicates that oxygen acts as an inhibitor.

Dissolution of iron atoms into liquid lead can be observed from the cross cut planes as shown in the last section. The histograms, however, provide the better views of the distributions of iron atom locations along the z direction. The histograms show how many iron atoms wander too far from their respective slab surfaces. That is, a distribution with long tails should suggest higher dissolution of iron atoms in liquid lead. Again the cases with grain boundaries generally perform worse than the cases of single crystals.

Finally, the radial distribution functions allow a comparison between the results from this modeling work and the results from the works by Takahashi et al. [20] and Maulana et al. [21]. Tables 4.10 and 4.11 list the closest distances between the pairs of Fe-Pb and Fe-Fe, respectively. The closest distance among iron atoms remains $2.5\,\mathring{A}$ in all cases. The closest distance between iron atoms in bulk iron crystals is $2.4825\ \mathring{A}$. So this indicates that the iron slabs still relatively retain their crystal structures. The closest distance between iron and lead atoms is $2.8\,\mathring{A}$ in almost all cases, except for the cases with oxygen at its solubility limit. When oxygen is present at its solubility limit of 1.3×10^{-3} wt. %, the closest distance between iron and lead atoms decreases to $2.7\,\mathring{A}$. At the oxygen solubility limit, oxygen is in its determining state of either staying as a solute

in lead or forming ionic bonds with lead. This may cause the deviation in the separation distances between lead and iron atoms.

Takahashi et al. reported the closest distances between the iron surface and the lead atom to be 1.79 $\mathring{A}$ and 1.48 $\mathring{A}$, depending on the original locations of a lead atom at the beginning of the simulation [20]. In addition, Takahashi et al. observed that liquid lead disturbs the crystal structure of iron near the contact surfaces. This behavior is also observed from the simulation results in this dissertation as iron atoms at the surface conglomerate into a denser network. Maulana et al. reported the closest distance between iron and lead atoms to be 2.7 $\mathring{A}$ for the system containing only iron and lead atoms [21]. The closest distances between Fe-Pb atoms from this dissertation are similar to what Maulana et al. reported.

Table 4.10 The closest distance between an Fe-Pb pair in each simulation case

	Closest Distance between Fe-Pb atoms ($\mathring{A}$)	
	No Grain Boundary	With Grain Boundary
No Oxygen	2.8	2.8
Oxygen at Solubility Limit	2.7	2.7
Pb:O at 1:1 atomic ratio	2.8	2.8

Table 4.11 The closest distance between an Fe-Fe pair in each simulation case

	Closest Distance between Fe-Fe atoms (Å)	
	No Grain Boundary	With Grain Boundary
No Oxygen	2.5	2.5
Oxygen at Solubility Limit	2.5	2.5
Pb:O at 1:1 atomic ratio	2.5	2.5

4.7 Conclusion

The simulation results show that the clusters of iron atoms become denser when put in liquid lead. There are two explanations for this behavior. First, iron atoms are compressed by lead atoms. Second, it is a self-defense mechanism of iron in order to deter the penetration of lead atoms by readjusting their configurations. As a result of readjustments, defects are introduced throughout the slabs, especially on the surfaces. When contacting surfaces turn rough, surface adsorption become favorable for lead atoms.

However, when oxygen is introduced into the systems, oxygen slows down the interaction rates between iron and lead. Oxygen can pin down lead atoms due to electrostatic forces. The results are analogous to adding carbon to iron as it prevents the glide of dislocations and sliding/slipping of iron atoms in the lattice. In addition, when oxygen forms magnetite oxide layers, iron in the oxide layers become positive ions. When lead atoms come near oxygen residing in the oxide layers, those lead atoms likely to become positive ions in order to form ionic bonding with oxygen. When this happens,

it is highly likely that positive iron ions and positive lead ions will repel each other due to electrostatic forces. This, in turn, helps against lead penetrations into iron slabs.

Finally, the simulation results confirm the following known experiment results:

1. Single crystal iron seems to be the best choice against liquid lead.
2. Oxygen acts as inhibitors by immobilizing lead atoms.
3. If iron crystals have been pre-oxidized before put into stagnant liquid lead, oxide layers protect lead atoms from diffusing into the core or bulk iron.

CHAPTER 5

CONCLUSIONS AND RECOMMENDATIONS

5.1 Conclusions

The aim of this work is to model oxidations by using molecular dynamics with a specific interest on iron in liquid lead with controlled oxygen. The first challenge in this work is to find a charge distribution that minimizes the total energy at each time step during a simulation. This challenge is overcome by using a mathematical optimization method called the Generalized Reduced Gradient (GRG) method. The GRG method guarantees charge neutrality at each time step during the course of a simulation. All simulations start with neutral atoms, and hence the net charge is zero. During a simulation, oxidations transform neutral atoms into ions, and the net charge in the system must be zero at all time during that simulation. The charge neutrality condition obeys the conservation of charge because charges cannot be created or destroyed. In addition, the GRG method ensures that each ion carries a charge that stays within its upper and lower limits. For example, an oxygen ion cannot carry a $-3e$ charge as the lowest charge it can carry is $-2e$, where e is the electron charge. The simulation results of the model with the GRG method agree with previously published data. This benchmarking confirms the validity of the GRG application in molecular dynamics modeling. This study has been published in Computational Materials Science (volume 46, issue 4, October 2009, pages 887-892).

The second challenge comes when modeling iron oxidation to form magnetite. Magnetite contains two different oxidation states of iron ions: one type carries the maximum charge of $+2e$ and the other type carries the maximum charge of $+3e$. The

problem is how to decide which type each iron ion belongs to. This is not a trivial problem because each iron ion normally carries a fractional charge, say $+0.25e$, not fully $+2e$ or $+3e$. The type determination of iron ions has to be based solely on the charge each iron ion carries. The simplest solution is to use the population ratio Fe^{2+}:Fe^{3+} that is always constant at 1:2, according to the chemical formula of magnetite Fe_3O_4 = (FeO)(Fe_2O_3). Iron ions with charges exceeding $+2e$ will be the Fe^{3+} type, while the rest will be randomly assigned to maintain the 1:2 population ratio. When implemented, the model yields satisfactory results when compared to the actual experiment results.

The last chapter combines the applications from Chapters 2 and 3, and demonstrates the robustness of this modeling work through the final simulation results. The systems containing iron in liquid lead with various oxygen concentrations have been simulated. The simulation results have come out as expected. The simulated systems show penetrations of lead atoms, dissolutions of solid iron in liquid lead, and the role of oxygen as an inhibitor. As the systems have behaved as hoped for, it is evident that this modeling work confirms the fundamental knowledge regarding corrosion attack of liquid lead on iron.

5.2 Recommendations for Future Work

The suggestion for future work can be divided into three parts. The first part concerns Moldy, the backbone computer code used in this dissertation for molecular dynamics simulations. The second part concerns the computer code for the GRG method. The final recommendations are about the basic assumptions and future systems to be modeled. Regarding Moldy, the following improvements should be done:

(1) Implement dynamic features into Moldy so that it can handle both static and dynamic simulations. This way, systems with flowing liquid lead can be simulated.

(2) Revise bookkeeping of Moldy such that it will

    a. Label ions separately from neutral atoms even though they are of the same element.

    b. Keep track of new morphing molecules, oxygen molecules to oxygen atoms.

    c. Be more flexible when new particles are introduced during ongoing simulations.

(3) Optimize the coding of Moldy so that it runs faster.

The current GRG code has been written from scratch. So there is a lot of room for improvements. The code has not been optimized for computational speed. Since the GRG function is repeatedly called during a simulation, an optimized GRG code will make a run time much shorter. If a more efficient algorithm exists, the GRG code should be replaced with that new algorithm.

Finally, there are opportunities to improve on assumptions and future systems to be simulated. The first assumption to be improved is on the iron oxidation in a form of magnetite. This dissertation assumes the simplest type classification of iron ions. A better assumption should give a more accurate results based on the magnetite structure. Furthermore, this dissertation only assumes that protective oxide layers consist of only magnetite. Not only magnetite exists, but other types of oxides exist as well. This is also true for oxidations of lead. It has been assumed that only one type of PbO forms.

However, if there is a change in simulation temperature, the other type of PbO can form as well. Therefore, future modifications to this modeling work should be more flexible regarding these oxide formations.

At its current stage, this modeling work is flexible enough for studies on various static (no flow) systems regarding oxidations. Only liquid lead is studied in this dissertation. Future studies can include bismuth, forming LBE, in simulations, or a different family of coolant materials entirely (such as sodium). Contaminations in systems or special grain boundary strengthening elements can also be studied. Structural alloys composed of iron, nickel, and chromium can also be modeled in place of pure iron. Predictive studies are also possible if the time spans are lengthened, say 100 ps or 1,000 ps. In the future if experimental data are available, benchmarking the simulation and experimental results can offer validations and further improvements of initial modeling assumptions.

APPENDIX

NOMENCLATURE

Symbol	Name	Unit
A	a fitting parameter for pair potential	eV
A_k	a constant in a wave equation	$\mathring{A}$
A_0	a constant in the oxide growth equation	$nm/Pa^{0.6}$–s
a	lattice parameter	$\mathring{A}$
a_0	the constant in the Rose equation	–
$\vec{a}$	acceleration vector	m/s
B	a fitting parameter for pair potential	eV
$\tilde{B}$	bulk modulus	GPa
$\vec{b}$	the jerk, the 3rd derivative of the position with respect to time	m/s^3
C_{IJ}	elastic constant	GPa
C_O	concentration of oxygen	wt. %
c	lattice parameter	$\mathring{A}$
D	diffusivity	cm^2/s
E	energy	eV or J
E_0	activation energy	eV or J
E_c	cohesive energy	eV or J
E^{es}	electrostatic energy	eV or J
E_k	kinetic energy	eV or J
F	embedding energy function	eV or J
F_0	fitting parameter for embedding energy function	eV or J
$\vec{F}$	force vector	N
f	electron density of an atom	–
f_e	equilibrium electron density of an atom	–
f_N	normalized distribution function	–
G^0	Gibbs free energy	eV or J
$\mathbf{G_R}$	reduced gradient	–
g	inequality constraint	–
h	equality constraint	–
IA	electron affinity energy	eV
IE	the first ionization energy	eV
J	self-Coulomb repulsion or chemical hardness	eV
J_{ij}	a matrix element in a row i and a column j	–
k	wave number	–
k_B	Boltzmann constant	eV/K

Symbol	Name	Unit
k_C	Coulomb constant	eV-$\mathring{A}/e^2$
m	mass of a particle	kg
N	the number of particles in a system	–
N_F	the number of degrees of freedom	–
n	the number of the nearest neighbors	–
$O(\ldots)$	big O notation	–
P	pressure	N/m^2
Q	fictitious mass parameter	$1/s^2$
q	charge	e
q^L	minimum charge limit	e
q^U	maximum charge limit	e
R	gas constant	J/mol-K
r	distance between two atoms	$\mathring{A}$
$\vec{r}$	position vector	$\mathring{A}$
r_e	the first nearest neighbor distance of a crystal at equilibrium	$\mathring{A}$
r_i	distance from the i^{th} neighbor to the site of interest	$\mathring{A}$
r_{ij}	distance between ions i and j	$\mathring{A}$
$\mathbf{S}$	search direction	–
T	temperature	K
T_0	heat bath temperature	K
t	time	s
Δt	time step	s
$\vec{v}$	velocity vector	m/s
$\vec{v}^{(p)}$	predicted velocity	m/s
$\vec{v}^{(c)}$	corrected velocity	m/s
w	energy penalty	eV
$\mathbf{Y}$	a set of basic variables	–
y	basic variable	–
$\mathbf{Z}$	a set of non-basic variables	–
z	non-basic variable	–
U	potential energy	eV or J
V	volume	$\mathring{A}^3$
Z	effective core charge	e
α	a fitting parameter for pair potential	–
α_M	Madelung constant	–
β	a fitting parameter for pair potential	–
γ_0	increase in activation free energy with thickness of oxide film	–

Symbol	Name	Unit
δ	Delta function	–
ζ	friction coefficient	s^{-1}
λ	Lagrange multiplier	–
μ	chemical potential	eV
ξ	coordinate of an atom in a crystal	$\mathring{A}$
π	Lagrange multiplier	–
ρ	electron density function	–
ρ_e	electron density at equilibrium	–
ρ_{Pb}	density of lead	g/cm^3
ρ_q	charge distribution function	–
φ	pair potential	eV
χ	electronegativity	eV
Ω_0	atomic volume at equilibrium	$\mathring{A}^3$
ω	phonon frequency	s^{-1}

BIBLIOGRAPHY

[1] Handbook on Lead–bismuth Eutectic Alloy and Lead Properties, Materials Compatibility, Thermal-hydraulics and Technologies, 2007 Edition, Nuclear Energy Agency, OECD 2007, NEA No. 6195.

[2] Baker, H. (Ed.), 1992, *ASM Handbook Volume 3: Alloy Phase Diagrams*, ASM International, Materials Park, OH, p. 103.

[3] U.S. Geological Survey, Mineral Commodity Summaries, January 2009

[4] Lyutyi, E. M., 1989, "Problems of High-Temperature Liquid-Metal Corrosion of Refractory Metals and Alloys," Materials Science, **24**(5), pp. 441-445.

[5] Manly, W. D., 1956, "Fundamentals of Liquid-metal Corrosion," Corrosion, **12**, pp. 46–52.

[6] Remy, F. N. and Bouchacourt, M., 1992, "Flow-assisted Corrosion: A Method to Avoid Damage," Nuclear Engineering and Design, **133**(1), pp. 23-30.

[7] Balbaud-Celerier, F. and Barbier, F., 2001, "Investigation of Models to Predict the Corrosion of Steels in Flowing Liquid Lead Alloys," Journal of Nuclear Materials, **289**(3), pp. 227-242.

[8] Heitz, E., 1991, "Chemo-mechanical Effects of Flow on Corrosion," Corrosion, **47**(2), pp. 135-145.

[9] Luk'yanova, I. N., Nevzorov, B. A., and Starkov, O. V., 1972, "Mechanical Properties of 1Kh16N15MZB and 1Kh18N10T Austenitic Steels Carburized in Liquid Sodium," Atomic Energy, **33**(4), pp. 974-975.

[10] Nikitin, V. I., 1966, "The Nature of the Corrosive Action of Oxygen-Bearing Liquid Sodium upon Steel," Materials Science, **1**(3), pp. 247-251.

[11] Guerin, S., Pastol, J.-L., Leroux, C., and Gorse, D., 2003, "Synergy Effect of LBE and Hydrogenated Helium on Resistance to LME of T91 Steel Grade," Journal of Nuclear Materials, **318**, pp. 339-347.

[12] Epstein, L. F., 1957, "Static and Dynamic Corrosion and Mass Transfer in Liquid Metal Systems," Chemical Engineering Progress Symposium Series, **53**(20), pp. 67-81.

[13] Sannier, J. and Santarini, G., 1982, "Etude de la corrosion de deux aciers ferritiques par le plomb liquide circulant dans un thermosiphon; recherche d'un modele," Journal of Nuclear Materials, **107**(2-3), pp. 196-217.

[14] Balbaud-Célérier, F. and Barbier, F., 2001, "Investigation of Models to Predict the Corrosion of Steels in Flowing Liquid Lead Alloys," Journal of Nuclear Materials, **289**(3), pp. 227-242.

[15] Zhang, J. and Li, N., 2003, "Parametric Study of a Corrosion Model Applied to Lead–Bismuth Flow Systems," Journal of Nuclear Materials, **321**(2-3), pp. 184-191.

[16] Zhang, J. and Li, N., 2004, "Corrosion/Precipitation in Non-isothermal and Multi-modular LBE Loop Systems," Journal of Nuclear Materials, **326**(2-3), pp. 201–210.

[17] Tan, T., Chen, Y., and Chen, H., 2008, "Theoretical Modeling and Numerical Simulation of the Corrosion and Precipitation in Non-isothermal Liquid Lead Alloy Pipe/Loop Systems," Heat and Mass Transfer, **44**(3), pp. 355–366.

[18] Chen, Y., Tan, T., and Chen, H., 2008, “Oxidation Companied by Scale Removal: Initial and Asymptotical Kinetics,” Journal of Nuclear Science and Technology, **45**(7), pp. 662–667.
[19] Tan, T. and Chen, Y., 2009, “Scale Removal Cellular Automaton Oxidation Models of Metals in Lead Bismuth Eutectic,” Journal of Electroanalytical Chemistry, **626**(1-2), pp. 89-97.
[20] Takahashi, M., Qi, Y., Nitta, H., Nishikawa, N., and Ohno, T., 2004, “First-Principles Molecular Dynamics Simulation on Interatomic Interaction of Fe Crystal with Pb and Bi Atoms,” Science and Technology of Advanced Materials, **5**(5-6), pp. 673-676.
[21] Maulana, A., Su’ud, Z., Hermawan K.D., and Khairurrijal, 2008, “Simulation Study of Steels Corrosion Phenomenon in Liquid Lead-Bismuth Cooled Reactors Using Molecular Dynamics Methods,” Progress in Nuclear Energy, **50**(2-6), pp. 616-620.
[22] Refson, K., 2000, “Moldy: A Portable Molecular Dynamics Simulation Program for Serial and Parallel Computers,” Computer Physics Communications, **126**(3), pp. 309-328.
[23] Humphrey, W., Dalke, A. and Schulten, K., 1996, "VMD - Visual Molecular Dynamics", Journal of Molecular Graphics, **14**(1), pp. 33-38.
[24] Zhang, J., Li, N., Chen, Y., and Rusanov, A. E., 2005, “Corrosion Behaviors of US Steels in Flowing Lead–Bismuth Eutectic (LBE),” Journal of Nuclear Materials, **336**(1), pp. 1-10.
[25] Zhang, J., Li, N., and Chen, Y., 2006, “Oxygen Control Technique in Molten Lead and Lead-Bismuth Eutectic Systems,” Nuclear Science and Engineering, **154**(2), pp. 223-232.
[26] Chen, Y., Chen, H., and Zhang, J., 2007, “Numerical Investigation on Enhancement of Oxygen Transfer by Forced Convection in Liquid Lead–Bismuth Eutectic System,” International Journal of Heat and Mass Transfer, **50**(11-12), pp. 2139-2147.
[27] Li, N., 2008, “Lead-Alloy Coolant Technology and Materials – Technology Readiness Level Evaluation,” Progress in Nuclear Energy, **50**(2-6), pp. 140-151.
[28] Finnis, M. W. and Sinclair, J. E., 1984, “A Simple Empirical N-body Potential for Transition Metals,” Philosophical Magazine A, **50**(1), pp.40-55.
[29] Daw, M. S. and Baskes, M. I., 1984, “Embedded-Atom Method: Derivation and Application to Impurities, Surfaces, and Other Defects in Metals,” Physical Review B, **29**(12), pp. 6443–6453.
[30] Daw, M. S., 1989, “Model of Metallic Cohesion: The Embedded Atom Method,” Physical Review B, **39**(11), pp. 7441-7451.
[31] Wadley, H. N. G., Zhou, X., Johnson R. A., and Neurock, M., 2001, “Mechanisms, Models and Methods of Vapor Deposition,” Progress in Materials Science, **46**(3-4), pp. 329-377.
[32] Johnson, R. A., 1988, “Analytic Nearest-Neighbor Model for FCC Metals,” Physical Review B, **37**(8), pp. 3924-3931.
[33] Banerjea, A., and Smith, J.R., 1988, “Origins of the Universal Binding-Energy Relation,” Physical Review B, **37**(12), pp. 6632–6645.

[34] Rappé, A. K. and Goddard, W. A., 1991, "Charge Equilibration for Molecular Dynamics Simulations," Journal of Physical Chemistry, **95**(8), pp. 3358-3363.
[35] Pearson, R. G., 1993, "Chemical Hardness – A Historical Introduction," Structure and Bonding, **80**, pp. 1-10.
[36] Streitz, F. H. and Mintmire, J. W., 1994, "Electrostatic Potential for Metal-oxide Surfaces and Interfaces," Physical Review B, **50**(16), pp.11996-12003.
[37] Zhou, X. W., Wadley, H. N. G., Filhol, J-S., and Neurock, M. N., 2004, "Modified Charge Transfer–Embedded Atom Method Potential for Metal/Metal Oxide Systems," Physical Review B, **69** (3), 035402.
[38] Venkataraman, P., 2002, *Applied Optimization with MATLAB Programming*, John Wiley & Sons, New York.
[39] Martinson, C. W. B., Flodstrom, S. A., Rundgren, J., and Westrin, P., 1979, "Oxygen Chemisorption on Aluminum Single Crystals: Site Determination by LEED Studies," Surface Science, **89**(1-3), pp. 102-113.
[40] Payling, R. and Ramsey, J. A., 1980, "Possible Ordered Structure in the Adsorption of Oxygen on Al(111)," Journal of Physics C: Solid State Physics, **13**(4), pp. 505-515.
[41] Yu, H. L., Munoz, M. C., and Soria, F., 1980, "On the Initial Stages of Oxidation of Al(111) by LEED Analysis," Surface Science, **94**(2-3), pp. L184-L190.
[42] Norman, D., Brennan, S., Jaeger, R., and Stohr, J., 1981, "Structural Models for the Interaction of Oxygen with Al(111) and Al Implied by Photoemission and Surface EXAFS," Surface Science, **105**(2-3), pp. L297-L306.
[43] Lamparter, P. and Kniep, R., 1997, "Structure of Amorphous Al_2O_3," Physica B, **234-236**, pp. 405-406.
[44] Campbell, T. J., Kalia, R. K., Nakano, A., and Vashishta, P., 1999, "Dynamics of Oxidation of Aluminum Nanoclusters using Variable Charge Molecular-Dynamics Simulations on Parallel Computers," Physical Review Letters, **82**(24), pp. 4866-4869.
[45] Hasnaoui, A., Politano, O., Salazar, J. M., Aral, G., Kalia, R. K., Nakano, A. and Vashishta, P., 2005, "Molecular Dynamics Simulations of the Nano-Scale Room-Temperature Oxidation of Aluminum Single Crystals," Surface Science, **579**(1), pp. 47-57.
[46] Alavi, S., Mintmire, J. W., and Thompson, D. L., 2005, "Molecular Dynamics Simulations of the Oxidation of Aluminum Nanoparticles," Journal of Physical Chemistry B, **109**(1), pp. 209-214.
[47] Wilding, M. C., Wilson, M., and McMillan, P. F., 2005, "X-ray and Neutron Diffraction Studies and MD Simulation of Atomic Configurations in Polyamorphic Y_2O_3-Al_2O_3 Systems," Philosophical Transactions of the Royal Society A, **363**(1827), pp. 589-607.
[48] Talbot, D. and Talbot, J., 1998, *Corrosion Science and Technology*, CRC Press, Boca Raton, FL, Chap. 7.
[49] Khanna, A. S., 2002, *Introduction to High Temperature Oxidation and Corrosion*, ASM International, Materials Park, OH, Chap. 6.
[50] Zhou, X. W., Wadley, H. N. G., Johnson, R. A., Larson, D. J., Tabat, N., Cerezo, A., Petford-Long, A. K., Smith, G. D. W., Clifton, P. H., Martens, R. L., and

Kelly, T. F., 2001, “Atomic Scale Structure of Sputtered Metal Multilayers,” Acta Materialia, **49**(19), pp. 4005-4015.
[51] Walmsley, S. H. and Pople, J. A., 1964, “Intermolecular Vibrations of Solid Carbon Dioxide,” Molecular Physics, **8**(4), pp. 345-356.
[52] Laufer, J. C. and Leroi, G. E., 1971, “Calculation of the Zero Wave Vector Lattice Frequencies of Alpha- and Beta- Oxygen,” Journal of Chemical Physics, **55**(1), pp. 993-1003.
[53] Hirshfelder, J. O., Curtiss, Ch. F., and Bird, R. B., 1954, *Molecular Theory of Gases and Liquids*, Wiley, NY.
[54] Wyckoff, R. W. G., 1963, *Crystal Structures I*, Interscience Publishers, New York, NY, pp. 85-237.
[55] Blake, R. L., Hessevick, R. E., Zoltai, T., and Finger, L. W., 1966, “Refinement of the Hematite Structure,” American Mineralogist, **51**(1-2), pp. 123-129.
[56] Fleet, M. E., 1981, “The Structure of Magnetite,” Acta Crystallographica B, **37**(4), pp. 917-920.
[57] Linstrom, P.J.; Mallard, W.G. (eds.), *NIST Chemistry WebBook, NIST Standard Reference Database Number 69*, National Institute of Standards and Technology, Gaithersburg MD, http://webbook.nist.gov
[58] Beest, B. W. H. van, Kramer, G. J., and Santen, R. A. van, 1990, “Force Fields for Silicas and Aluminophosphates Based on *Ab Initio* Calculations,” Physical Review Letters, **64**(16), pp. 1955-1958.
[59] Kittel, C., 2005, *Introduction to Solid State Physics*, John Wiley & Sons, Hoboken, NJ, Chap. 3.
[60] Rustad, J. R., Wasserman, E., and Felmy, A. R., 1999, “A Molecular Dynamics Investigation of Surface Reconstitution on Magnetite (001),” Surface Science, **432**(1-2), pp. L583-L588.
[61] Grosvenor, A. P., Kobe, B. A., and McIntyre, N. S., 2004, “Examination of the Oxidation of Iron by Oxygen Using X-ray Photoelectron Spectroscopy and QUASES™,” Surface Science, **565**(2-3), pp. 151-162.
[62] Eley, D. D. and Wilkinson, P. R., 1960, “Adsorption and Oxide Formation on Aluminium Films,” Proceedings of the Royal Society of London, Series A, Mathematical and Physical, **254**(1278), pp. 327-342.
[63] Grosvenor, A. P., Kobe, B. A., and McIntyre, N. S., 2005, “Activation Energies for the Oxidation of Iron by Oxygen Gas and Water Vapour,” Surface Science, **574**(2-3), pp. 371-321.
[64] Li, N., 2002, “Active Control of Oxygen in Molten Led-Bismuth Eutectic Systems to Prevent Steel Corrosion and Coolant Contamination,” Journal of Nuclear Materials, **300**(1), pp. 73-81.
[65] Zrodnikov, A. V., Efanov, A. D., Orlov, Yu. I., Martynov, P. N., Troyanov, V. M., and Rusanov, A. E., 2004, “Heavy Liquid Metal Coolant – Lead-Bismuth and Lead – Technology,” Atomic Energy, **97**(2), pp. 534-537.
[66] Yeliseyeva, O. and Tsisar, V., 2008, “Kinetic Features of Iron Oxidation in Liquid Lead Saturated with Oxygen Below and Above the Chaudron Point (570 ◦C),” Oxidation of Metals, **70**(3-4), pp. 213-227.

[67] Boher, P., Garnier, P., Gavarri, J.R., and Hewat, A.W., 1985, “Monoxyde quadratique PbOα(I): Description de la transition structurale ferroe´lastique,” **57**(3), pp. 343-350.
[68] Giefersa, H. and Porsch, F., 2007, “Shear Induced Phase Transition in PbO under High Pressure,” Physica B, **400**(1-2), pp. 53–58.
[69] Johnson, R. A., 1989, “Alloy Models with the Embedded-Atom Method,” Physical Review B, **39**(17), pp. 12554-12559.

VITA

Graduate College
University of Nevada, Las Vegas

Chaiyod Soontrapa

Address:
1401 Elizabeth Ave Apt 1
Las Vegas, NV 89119

Degrees:

Bachelor of Science, Physics, 2001
Carnegie Mellon University, Pittsburgh, PA

Bachelor of Science, Mathematics, 2001
Carnegie Mellon University, Pittsburgh, PA

Bachelor of Science, Economics, 2001
Carnegie Mellon University, Pittsburgh, PA

Master of Science, Nuclear Science and Engineering, 2005
Massachusetts Institute of Technology, Cambridge, MA

Master of Science, Materials Science and Engineering, 2005
Massachusetts Institute of Technology, Cambridge, MA

Publication:

Soontrapa, C. and Chen, Y., 2009, "Optimization Approach in Variable-Charge Potential for Metal/Metal Oxide Systems," Computational Materials Science, **46**(4), pp. 887-892

Dissertation Title: Oxidation Modeling by Means of Molecular Dynamics

Dissertation Examination Committee:

Chairperson, Yitung Chen, Ph. D.
Committee Member, Robert Boehm, Ph. D.
Committee Member, William Culbreth, Ph. D.
Committee Member, Anthony Hechanova, Ph. D.
Graduate Faculty Representative, John W. Farley, Ph. D.